Master Thesis

A Study of Thermal Radiation Shields for Cryogenic Gravitational Wave Detectors

低温重力波検出器の熱シールドの研究

Department of Physics, Graduate School of Science, The University of Tokyo

Yusuke Sakakibara

東京大学大学院理学系研究科物理学専攻　35-106033　榊原裕介

January 2012

Introduction

Although the existence of gravitational waves is derived from Einstein's theory of general relativity and has been proved indirectly by an observed change in the period of a binary pulsar[1], it hasn't been detected directly. If it is eventually detected directly, it will not only test the theory of general relativity, but also contribute to astronomy and atomic theory by acquiring information about the early universe, which cannot be obtained by electromagnetic wave observations, and the inner states of neutron stars.

In order to detect gravitational waves directly, gravitational wave detectors, such as LIGO[3], VIRGO[4], GEO[5], are working at locations around the world. In Japan, the Large-scale Cryogenic Gravitational wave Telescope (LCGT)[2] is proceeding. It is necessary to detect very small changes in the distance between test masses to detect gravitational waves. The gravitational wave detectors mentioned above are planned to detect them using interferometry. Thermal fluctuation of the interferometer mirrors and seismic vibration are sources of noise in detecting gravitational waves. In LCGT, the mirrors will be cooled down to cryogenic temperature (20 K) to reduce the thermal fluctuation and it will be constructed in an underground Kamioka laboratory to reduce the seismic noise. Although this thesis is a study of a radiation shield to realize LCGT, this study can be applied to other advanced interferometric gravitational wave detectors, such as ET[6], in the future.

It is necessary to estimate all of the heat loads on the cryocoolers in order to design the LCGT cryostat appropriately. The cooling power is limited because only four small cryocoolers for each cryostat will be used to prevent vibration of the cryocoolers from causing noise, and not to cause any danger of using cooling gas underground.

Especially, in order to estimate thermal radiation, it is necessary to know emissivity of materials at low temperature for the radiation shields. Measurements are presented here of the reflectivity of samples that are candidates for the radiation shields of LCGT using a CO_2 laser with wavelength $\lambda = 10.59$ μm, where black body radiation of 300 K has the largest intensity.

As an application of the result of the reflectivity measurements, the incident heat through duct shields was calculated using a ray-trace model. Only cryostats that contain the mirrors will be cooled down while the beam ducts and the vibration isolation system are to be kept at room temperature in LCGT, because it is difficult to cool all of the huge 3 km interferometer. Although the mirror should be surrounded by a radiation shield, a hole in the shield is necessary for the laser beam. Thus, it is necessary to reduce thermal radiation from the hole of the cryostat. For this purpose, aluminum pipes and baffles, called duct shields, will be used. Thermal radiation (funneling) through the duct shield was calculated using a ray-trace model. In order to verify this calculation, thermal radiation through a small aluminum pipe with baffles was measured.

Contents

1 Graviational waves **9**
1.1 Derivation of GWs . . . 9
1.2 Quadrupole radiation . . . 11
1.2.1 Oscillating masses . . . 11
1.2.2 Masses in a circular orbit (model of a binary pulsar) . . . 12
1.2.3 A Rotating rigid body (model of a neutron star) . . . 13
1.3 An indirect proof of the existence of GWs . . . 14

2 Detection of gravitational waves **17**
2.1 Principle of detecting GWs . . . 17
2.1.1 Phase shift in a Michelson interferometer due to GWs . . . 17
2.1.2 Response function and arm length . . . 19
2.2 Fabry-Perot interferometer as a gravitational wave detector . . . 20
2.2.1 Fabry-Perot interferometer . . . 20
2.2.2 Response of the Fabry-Perot interferometer to GWs . . . 21
2.3 Noise in an interferometer . . . 23
2.3.1 Shot noise of light . . . 23
2.3.2 Thermal noise . . . 24
2.3.3 Seismic noise . . . 27
2.3.4 Radiation pressure noise and the quantum limit . . . 27
2.3.5 Example of noise spectrum . . . 29
2.4 CLIO, CLIK and LCGT . . . 30

3 Thermal radiation **31**
3.1 Thermal radiation . . . 31
3.2 Black body radiation . . . 32
3.2.1 Definition of a black body . . . 32
3.2.2 Planck's law . . . 32
3.2.3 Wien's displacement law . . . 33

3.2.4 Stefan-Boltzmann law 33
3.3 Emissivity 33
3.4 Kirchhoff's law 34
3.5 Heat transfer by radiation 35
3.5.1 View factor 35
3.5.2 Heat transfer by radiation in a gray-body system 36
3.5.3 Some examples 38

4 Reflectivity Measurements (Metals) 41
4.1 Theory about the dependence of the reflectivity of metal on the temperature . . 41
4.2 Measured samples 44
4.3 Preliminary measurements 44
4.3.1 Laser turned on and off 47
4.3.2 Laser continuously turned on 47
4.4 Method of measurements 49
4.4.1 Measurements at room temperature 49
4.4.2 Measurements at cryogenic temperature 51
4.5 Results of measurements 54
4.5.1 Measurements at room temperature 54
4.5.2 Measurements at cryogenic temperature 55
4.6 Error analysis 58
4.6.1 Measurements at room temperature 58
4.6.2 Measurements at cryogenic temperature 59
4.7 Discussion 60

5 Reflectivity Measurements (Metal with high emissivity coatings) 63
5.1 Measured samples 63
5.2 Preliminary measurements 63
5.2.1 Laser turned on and off 63
5.2.2 Laser continuously turned on 65
5.3 Method of measurements 66
5.3.1 Measurements at room temperature 66
5.3.2 Measurements at cryogenic temperature 66
5.4 Results of measurements 67
5.4.1 Measurements at room temperature 67
5.4.2 Measurements at cryogenic temperature 70
5.5 Error analysis 70
5.5.1 Measurements at room temperature 70
5.5.2 Measurements at cryogenic temperature 73

5.6 Discussion 74

6 Thermal radiation (funneling) through a shield pipe for LCGT 75
6.1 Calculation 76
6.1.1 Method 76
6.1.2 Result 79
6.2 Experiment 81
6.2.1 Method 81
6.2.2 Result 83
6.2.3 Discussion 89

7 Conclusion 91

A Sample program 93
A.1 Flowchart to calculate the incident heat through the duct shield 93
A.2 A sample program to calculate the incident heat through the duct shield 95

Chapter 1

Graviational waves

This chapter describes a derivation of gravitational waves (GWs) from Einstein's theory of general relativity, examples of calculations of GWs' waveforms and how the existence of GWs has been proved indirectly.[7]

1.1 Derivation of GWs

In 4-dimensional space-time

$$ds^2 = g_{\mu\nu} dx^\mu dx^\nu, \tag{1.1}$$

a metric

$$g_{\mu\nu} = \eta_{\mu\nu} + h_{\mu\nu}, \mid h_{\mu\nu} \mid \ll 1 \tag{1.2}$$

can be considered. Here, $\eta_{\mu\nu}$ represents flat space-time

$$\eta_{\mu\nu} = \begin{pmatrix} -1 & 0 & 0 & 0 \\ 0 & 1 & 0 & 0 \\ 0 & 0 & 1 & 0 \\ 0 & 0 & 0 & 1 \end{pmatrix}. \tag{1.3}$$

Then, the Einstein equations

$$R_{\mu\nu} - \frac{1}{2} g_{\mu\nu} R = \frac{8\pi G}{c^4} T_{\mu\nu} \tag{1.4}$$

are expanded to linear order in $h_{\mu\nu}$. First, the Riemann tensor is calculated to linear order in $h_{\mu\nu}$ as follows:

$$R_{\mu\nu\rho\sigma} = \frac{1}{2}(\partial_\nu \partial_\rho h_{\mu\sigma} + \partial_\mu \partial_\sigma h_{\nu\rho} - \partial_\mu \partial_\rho h_{\nu\sigma} - \partial_\nu \partial_\sigma h_{\mu\rho}). \tag{1.5}$$

Using the trace of $h_{\mu\nu}$

$$h = \eta^{\mu\nu} h_{\mu\nu}, \tag{1.6}$$

$$\bar{h}_{\mu\nu} = h_{\mu\nu} - \frac{1}{2}\eta_{\mu\nu}h \tag{1.7}$$

is defined. Using this h, eq.(1.4) is rewritten as

$$\Box\bar{h}_{\mu\nu} + \eta_{\mu\nu}\partial^\rho\partial^\sigma\bar{h}_{\rho\sigma} - \partial^\rho\partial_\nu\bar{h}_{\mu\rho} - \partial^\rho\partial_\mu\bar{h}_{\nu\rho} = -\frac{16\pi G}{c^4}T_{\mu\nu}. \tag{1.8}$$

Here, one can choose the Lorentz gauge

$$\partial^\nu\bar{h}_{\mu\nu} = 0, \tag{1.9}$$

and obtain

$$\Box\bar{h}_{\mu\nu} = -\frac{16\pi G}{c^4}T_{\mu\nu}. \tag{1.10}$$

Here, independent degrees of freedom in the symmetric tensor $h_{\mu\nu}$ have been reduced from 10 to 6. Outside the wave source, $T_{\mu\nu} = 0$, one obtains

$$\Box\bar{h}_{\mu\nu} = 0. \tag{1.11}$$

In addition, one can choose the coordinate that satisfies the condition

$$\bar{h} = 0, h^{0i} = 0. \tag{1.12}$$

It can decrease the independent degrees of freedom in $h_{\mu\nu}$ from 6 to 2. In the end, one obtains

$$h^{0\mu} = 0, h^i_i = 0, \partial^j h_{ij} = 0 \tag{1.13}$$

(the transverse-traceless gauge or TT gauge). Eq.(1.11) has plane-wave solutions $h^{TT}_{ij}(x) = e_{ij}(\mathbf{k})e^{ikx}$. Assuming $\hat{\mathbf{n}} = \mathbf{k}/\mid\mathbf{k}\mid$ is toward the z direction, one can obtain

$$h^{TT}_{ab}(t,z) = \begin{pmatrix} h_+ & h_\times \\ h_\times & -h_+ \end{pmatrix}_{ab} \cos\left[\omega\left(t - \frac{z}{c}\right)\right]. \tag{1.14}$$

In this case, an interval is

$$\begin{aligned} ds^2 &= -c^2dt^2 + (\delta_{ij} + h^{TT}_{ij})dx^idx^j && (1.15)\\ &= -c^2dt^2 + dz^2 + \left\{1 + h_+\cos\left[\omega\left(t - \frac{z}{c}\right)\right]\right\}dx^2 + \left\{1 - h_+\cos\left[\omega\left(t - \frac{z}{c}\right)\right]\right\}dy^2 \\ &\quad +2h_\times\cos\left[\omega\left(t - \frac{z}{c}\right)\right]dxdy. && (1.16) \end{aligned}$$

The proper distance between two points $(t, x_1, 0, 0)$ and $(t, x_2, 0, 0)$, whose coordinate distance is $x_2 - x_1 = L$, is

$$s = (x_2 - x_1)[1 + h_+\cos(\omega t)]^{1/2} \simeq L\left[1 + \frac{1}{2}h_+\cos(\omega t)\right]. \tag{1.17}$$

GWs can be detected by measuring how long light takes to pass between the two points since the proper distance divided by c is equal to the time light takes to pass between them.

1.2 Quadrupole radiation

A solution of eq.(1.10) is given by

$$\bar{h}_{\mu\nu}(t,\mathbf{x}) = \frac{4G}{c^4}\int d^3x' \frac{1}{\mid \mathbf{x}-\mathbf{x}' \mid} T_{\mu\nu}\left(t - \frac{\mid \mathbf{x}-\mathbf{x}' \mid}{c}, \mathbf{x}'\right). \tag{1.18}$$

Here, assuming that $r \gg d$ and $v \ll c$ (nonrelativistic), where d is the typical length scale of the wave source and r is the distance from the wave source $\mathbf{x}'$ to the observation point $\mathbf{x}$, one can obtain the terms of the lowest order (the quadrupole radiation)

$$[h_{ij}^{TT}(t,\mathbf{x})]_{\rm quad} = \frac{1}{r}\frac{2G}{c^4}\Lambda_{ij,kl}(\hat{\mathbf{n}})\ddot{M}_{kl}(t-r/c) = \frac{1}{r}\frac{2G}{c^4}\Lambda_{ij,kl}(\hat{\mathbf{n}})\ddot{Q}_{kl}(t-r/c). \tag{1.19}$$

Here, $\Lambda_{ij,kl}(\hat{\mathbf{n}})$, called lambda tensor, includes information about the direction of radiation of GWs. M^{ij} is the second mass moment and Q^{ij} is the quadrupole moment; their definitions are as follows:

$$M^{ij} = \int d^3x \rho(t,\mathbf{x}) x^i x^j, \tag{1.20}$$

$$Q^{ij} = M^{ij} - \frac{1}{3}\delta^{ij}M_{kk} = \int d^3x \rho(t,\mathbf{x})\left(x^i x^j - \frac{1}{3}r^2\delta^{ij}\right), \tag{1.21}$$

where $\rho(t,\mathbf{x})$ is the mass density. Using the energy-momentum tensor, one can obtain energy per unit time radiated by the quadrupole radiation:

$$P_{\rm quad} = \frac{G}{2c^5}\langle \dddot{Q}_{ij}\dddot{Q}_{ij}\rangle = \frac{G}{2c^5}\langle \dddot{M}_{ij}\dddot{M}_{ij} - \frac{1}{3}(\dddot{M}_{kk})^2\rangle, \tag{1.22}$$

where $\langle\cdots\rangle$ represents an average over several periods of the mass motion. Next, examples of the quadrupole radiation are given.

1.2.1 Oscillating masses

One can consider two masses connected with a spring and assume that the relative coordinate is

$$z_0(t) = a\cos\omega_s t. \tag{1.23}$$

The mass density, using the reduced mass μ, is

$$\rho(t,\mathbf{x}) = \mu\delta(x)\delta(y)\delta(z - z_0(t)) \tag{1.24}$$

and then

$$\begin{aligned} M^{ij} &= \int d^3x\rho(t,\mathbf{x})x^ix^j \\ &= \mu z_0^2(t)\delta^{i3}\delta^{j3} \\ &= \mu a^2\frac{1+\cos 2\omega_s t}{2}\delta^{i3}\delta^{j3}. \end{aligned} \tag{1.25}$$

From eq.(1.19), one can obtain

$$h_+(t) = \frac{2G\mu a^2\omega_s^2}{rc^4}\sin^2\iota\cos(2\omega_s t), \tag{1.26}$$

$$h_\times(t) = 0, \tag{1.27}$$

where ι is the angle between the z axis and the direction of the observer. h_+ vanishes when the observer is in the direction of the z axis. The angular frequency of GWs is just two-times larger than that of the oscillation of the masses. From eq.(1.22),

$$P_{\text{quad}} = \frac{16}{15}\frac{G\mu^2}{c^5}a^4\omega_s^6. \tag{1.28}$$

1.2.2 Masses in a circular orbit (model of a binary pulsar)

One can consider two masses m_1, m_2 moving along a circular orbit and assume that the relative coordinate is

$$x_0(t) = R\cos\left(\omega_s t + \frac{\pi}{2}\right), \tag{1.29}$$

$$y_0(t) = R\sin\left(\omega_s t + \frac{\pi}{2}\right), \tag{1.30}$$

$$z_0(t) = 0. \tag{1.31}$$

Using

$$M^{ij} = \mu x_0^i(t)x_0^j(t), \tag{1.32}$$

where $\mu = m_1m_2/(m_1+m_2)$ is the reduced mass, eq.(1.19) becomes

$$h_+(t) = \frac{1}{r}\frac{4G\mu\omega_s^2R^2}{c^4}\left(\frac{1+\cos^2\iota}{2}\right)\cos(2\omega_s t), \tag{1.33}$$

$$h_\times(t) = \frac{1}{r}\frac{4G\mu\omega_s^2R^2}{c^4}\cos\iota\sin(2\omega_s t). \tag{1.34}$$

Here, ι is the angle between the normal to the orbit and the direction of the observer. When $\iota = \pi/2$, namely, the observer is on the orbital plane, $h_\times$ vanishes and GWs are linearly polarized. On the other hand, when $\iota = 0$, namely, the observer is in the direction of the normal of the orbital plane, GWs are circularly polarized since h_+ and $h_\times$ have the same amplitude and change as $\cos(2\omega_s t)$ and $\sin(2\omega_s t)$, respectively. The typical value is

$$h_0 = \frac{1}{r}\frac{4G\mu\omega_s^2 R^2}{c^4} = \frac{4}{r}\left(\frac{GM_c}{c^2}\right)^{5/3}\left(\frac{\pi f_{\rm gw}}{c}\right)^{2/3} \tag{1.35}$$

$$\simeq 2.56\times 10^{-23}\left(\frac{100\ {\rm Mpc}}{r}\right)\left(\frac{M_c}{M_\odot}\right)^{5/3}\left(\frac{f_{\rm gw}}{100\ {\rm Hz}}\right)^{2/3}. \tag{1.36}$$

Here, the chirp mass $M_c = (m_1 m_2)^{3/5}/(m_1+m_2)^{1/5}$, the frequency of GWs $f_{\rm gw}$ satisfying $2\pi f_{\rm gw} = 2\omega_s$, and Kepler's law

$$\omega_s^2 = \frac{G(m_1+m_2)}{R^3} \tag{1.37}$$

are used. $f_{\rm gw}$ reaches 100 Hz during the last several seconds to coalescence in the case that $M_c = M_\odot$. Moreover, eq.(1.22) becomes

$$P_{\rm quad} = \frac{32}{5}\frac{G\mu^2}{c^5}R^4\omega_s^6. \tag{1.38}$$

1.2.3 A Rotating rigid body (model of a neutron star)

One can consider the coordinate where the inertia tensor of a rigid body is diagonalized. Now, a rigid body whose principal moments of inertia are I_1, I_2, I_3 around the x, y, z axes respectively is rotating around the z axis with an angular velocity ω_s and a frequency $f_{\rm rot}$. Using

$$M_{ij} = -I_{ij} + c_{ij}, \tag{1.39}$$

where I_{ij} is the inertia tensor and c_{ij} is a constant tensor, eq.(1.19) becomes

$$\begin{aligned} h_+(t) &= h_0\frac{1+\cos^2\iota}{2}\cos(2\omega_s t), \\ h_\times(t) &= h_0\cos\iota\sin(2\omega_s t), \end{aligned} \tag{1.40}$$

where,

$$h_0 = \frac{4\pi^2 G}{c^4}\frac{I_3 f_{\rm gw}^2}{r}\epsilon. \tag{1.41}$$

Now, $f_{\rm gw} = 2f_{\rm rot}$ is the frequency of GWs, which is equal to twice the rotational frequency of the rigid body $f_{\rm rot}$. Also,

$$\epsilon \equiv \frac{I_1 - I_2}{I_3} \tag{1.42}$$

is the ellipticity. The typical value is

$$h_0 \simeq 1.06 \times 10^{-27} \left(\frac{\epsilon}{10^{-6}}\right) \left(\frac{I_3}{10^{38}\ \mathrm{kg\ m^2}}\right) \left(\frac{10\ \mathrm{kpc}}{r}\right) \left(\frac{f_{\mathrm{gw}}}{100\ \mathrm{Hz}}\right)^2 . \tag{1.43}$$

Here, $I_3 \sim M_\odot a_{\mathrm{ns}}^2$, where $M_\odot$ is the solar mass and $a_{\mathrm{ns}} = 10$ km is a typical radius of neutron stars. The more rapidly a neutron star rotates, the stronger are the GWs that it radiates because $h_0 \propto f_{\mathrm{gw}}^2$. In addition, eq.(1.22) becomes

$$P = \frac{32G}{5c^5} \epsilon^2 I_3^2 \omega_s^6 . \tag{1.44}$$

1.3 An indirect proof of the existence of GWs

Eq.(1.22), derived from the theory of general relativity, is consistent with the observed result concerning the change in the period of the Hulse Taylor binary pulsar PSR B1913+16 caused by its radiation of GWs.[1] The orbital phase $\phi_b(T)$ at time T, using the orbital frequency ν_b, is

$$\frac{1}{2\pi}\phi_b(T) = \nu_b T + \frac{1}{2}\dot{\nu}_b T^2 + \cdots . \tag{1.45}$$

When it passes the periastron for the nth time, $\phi_b(T_n) = 2\pi n$, that is,

$$\nu_b T_n + \frac{1}{2}\dot{\nu}_b T_n^2 = n \tag{1.46}$$

and thus

$$T_n - \frac{n}{\nu_b} = -\frac{\dot{\nu}_b}{2\nu_b} T_n^2 . \tag{1.47}$$

Or, using the orbital period $P_b = 1/\nu_b$,

$$T_n - P_b n = \frac{\dot{P}_b}{2P_b} T_n^2 . \tag{1.48}$$

The theoretical values and experimental values are plotted in Figure 1.1. The experimental value of $\dot{P}_b$ is consistent with the theoretical value at the (0.13± 0.21) % level.[1]

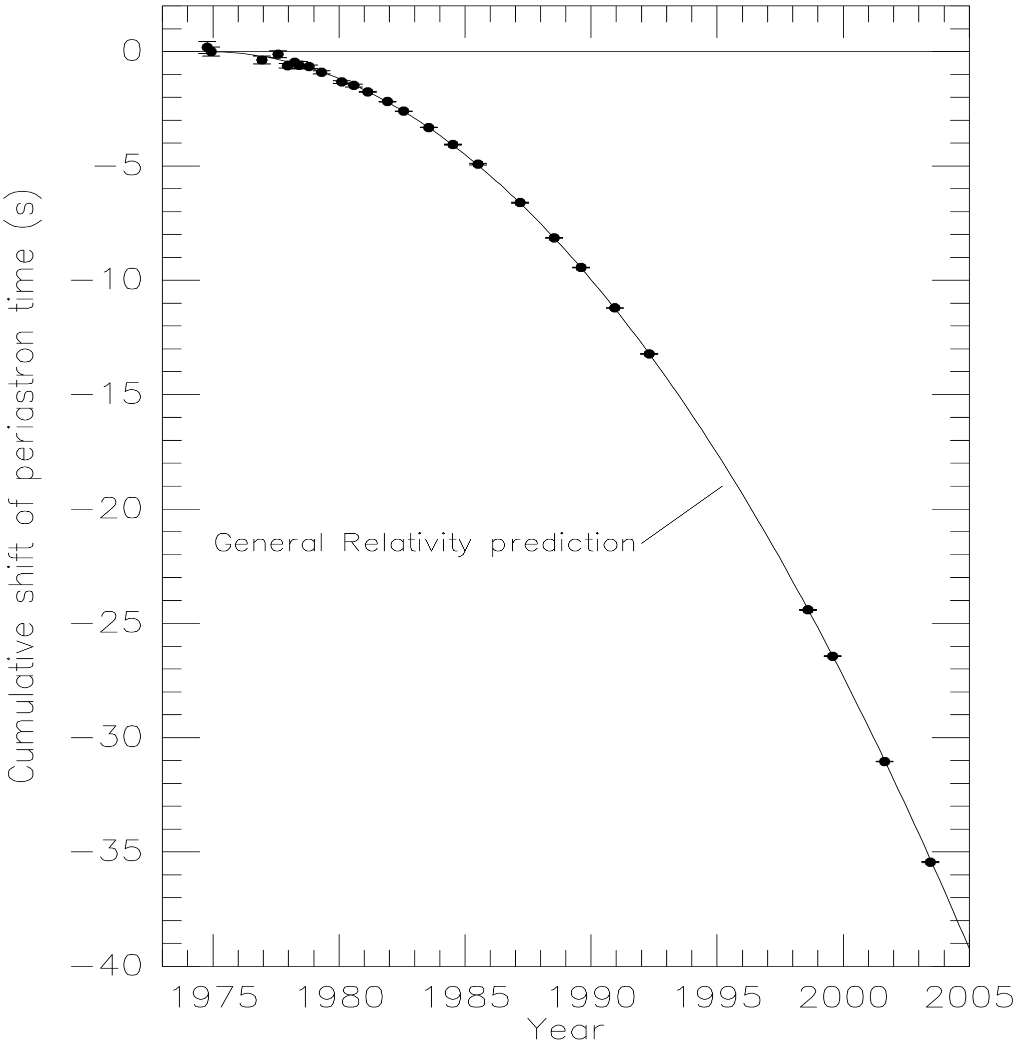

Figure 1.1: Change in the period of the Hulse Taylor binary pulsar PSR B1913+16. "Orbital decay of PSR B1913+16. The data points indicate the observed change in the epoch of periastron with date while the parabola illustrates the theoretically expected change in epoch for a system emitting gravitational radiation, according to general relativity."[1]

Chapter 2

Detection of gravitational waves

This chapter describes the principle of one way to detect gravitational waves (GWs) directly, that is, a laser interferometer.[8],[9]

2.1 Principle of detecting GWs

2.1.1 Phase shift in a Michelson interferometer due to GWs

In the Michelson interferometer shown in Figure 2.1, the current that flows through the photo detector changes as

$$I_P = \frac{I_{\max} + I_{\min}}{2} + \frac{(I_{\max} - I_{\min}) \cos(\phi_1 - \phi_2)}{2}. \tag{2.1}$$

Here,

$$K = \frac{I_{\max} - I_{\min}}{I_{\max} + I_{\min}} \tag{2.2}$$

is called visibility, which shows the clarity of interference fringes.

Next, let's think about the phase shift produced by GWs. Using the 4-dimentional infinitesimal length

$$ds^2 = -c^2 dt^2 + (1 + h)dx^2 + (1 - h)dy^2 + dz^2, \tag{2.3}$$

the velocity of light that makes a round trip along the x axis is

$$\frac{dx}{dt} = \pm \frac{c}{\sqrt{1 + h(t)}}. \tag{2.4}$$

Then, when the light comes in the beam splitter at time τ_1, makes a round trip on the distance

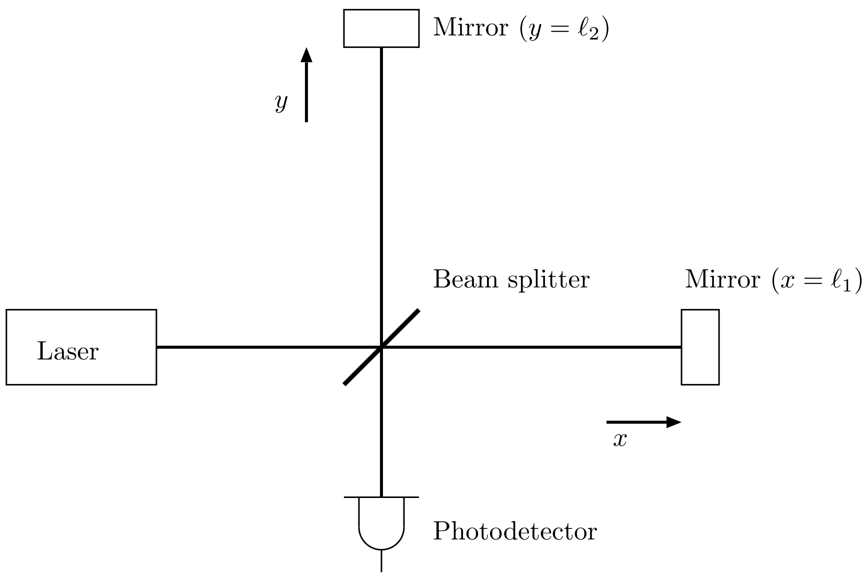

Figure 2.1: Michelson interferometer. The origin is on the beam splitter and x, y axes are set to the direction represented by the arrows. The light from the laser is split by a beam splitter. Then, the light travels to the mirrors, returns to the beam splitter and interferes. The interference is detected by a photodetector.

ℓ_1 and comes back to the beam splitter at time t, integrating eq.(2.4) from τ_1 to t produces

$$\frac{2\ell_1}{c} = \int_{\tau_1}^{t} \frac{dt'}{\sqrt{1+h(t')}} \approx \int_{\tau_1}^{t} \left[1 - \frac{1}{2}h(t')\right] dt' = t - \tau_1 - \frac{1}{2}\int_{\tau_1}^{t} h(t')dt'. \tag{2.5}$$

The lower limit of the integral in the third term of the right-hand side is approximately $\tau_1 = t - 2\ell_1/c$, considering this equation to a linear order in h; and then, the phase of the light is

$$\phi_1(t) = \Omega\tau_1 = \Omega\left[t - \frac{2\ell_1}{c} - \frac{1}{2}\int_{t-2\ell_1/c}^{t} h(t')dt'\right]. \tag{2.6}$$

Because the effect of GWs has a opposite sign on the y axis, the phase shift is

$$\Delta\phi = \phi_1 - \phi_2 = -\frac{2\Omega(\ell_1 - \ell_2)}{c} - \Delta\phi_{\rm GR}(t), \tag{2.7}$$

$$\Delta\phi_{\rm GR}(t) = \Omega\int_{t-2\ell/c}^{t} h(t')dt' \quad (\ell_2 \approx \ell_1 = \ell). \tag{2.8}$$

2.1.2 Response function and arm length

When h changes slowly, eq.(2.8) becomes

$$\Delta\phi_{\mathrm{GR}}(t) \approx \frac{4\pi}{\lambda} h(t)\ell, \tag{2.9}$$

which shows that the longer is the arm length, the higher does the sensitivity become. Actually, the response function of $h(t)$ to $\Delta\phi_{\mathrm{GR}}(t)$ is

$$H_{\mathrm{M}}(\omega) = \frac{2\Omega}{\omega} \sin(\ell\omega/c) e^{-i\ell\omega/c}. \tag{2.10}$$

For a certain frequency to be observed ($\omega = \omega_0$), the modulus of this function takes the maximum value at $\ell\omega_0/c = \pi/2$. Namely, if the arm length is longer than this value, the interferometer is no more sensitive. The modulus of eq.(2.10) is given in Figure 2.2, which shows that the longer arm length limits the band width.

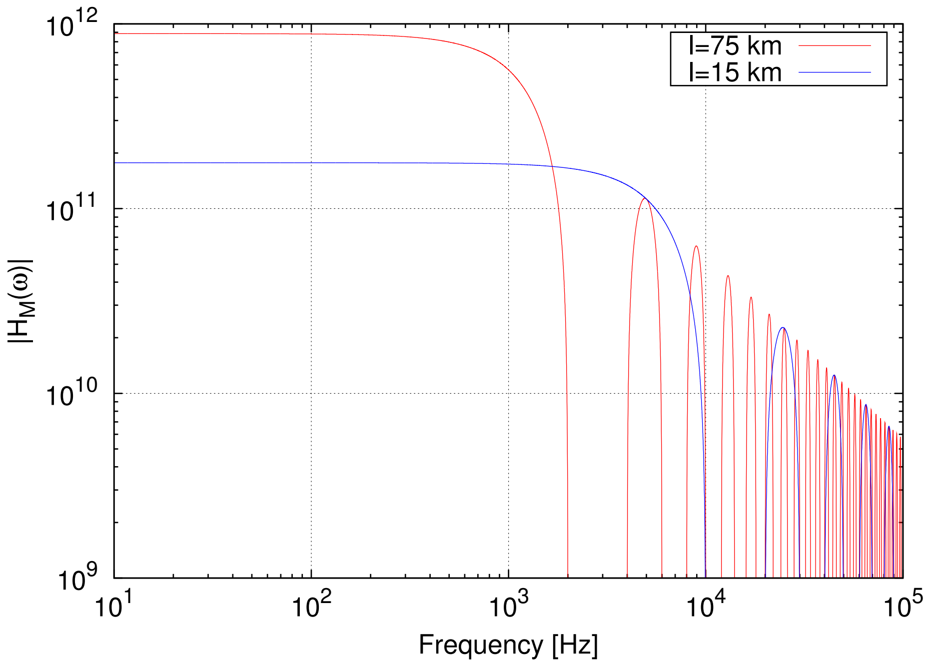

Figure 2.2: Response function of a Michelson interferometer. Here, the wavelength of the laser is $\lambda = 1064$ nm.

2.2 Fabry-Perot interferometer as a gravitational wave detector

2.2.1 Fabry-Perot interferometer

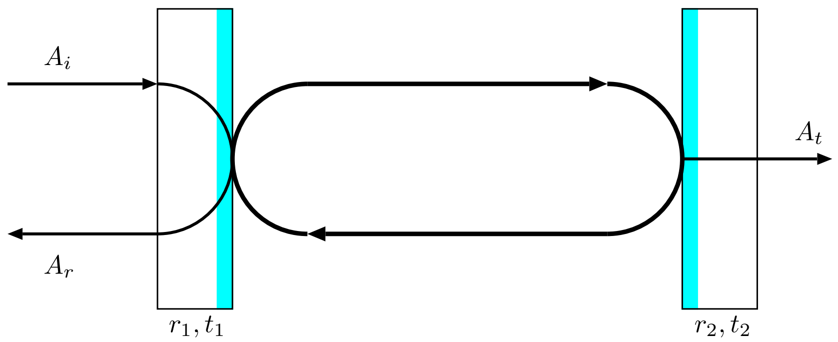

Figure 2.3: Fabry-Perot cavity

In a Fabry-Perot cavity, where two mirrors are set facing each other, as shown in Figure 2.3, the light goes back and forth many times. Only light with a certain wavelength resonates and has a large transmission intensity. r and t are the reflectivity and transmissivity of the mirrors, respectively. A formularization of the Fabry-Perot cavity is now described.

In Figure 2.3, when an incident light wave $A_i(t) = e^{i\Omega t}$ comes to the cavity, the reflection is

$$A_r(t) = r_1 e^{i\Omega t} - \frac{t_1^2}{r_1} \sum_{n=1}^{\infty} (r_1 r_2)^n \exp(i\Omega\tau_n) \quad \left(\tau_n = t - \frac{2\ell}{c} n\right); \tag{2.11}$$

namely,

$$A_r(t) = e^{i\Omega t}[r_1 - a(\Omega)], \tag{2.12}$$

$$a(\Omega) = \frac{t_1^2 r_2 \exp(-2i\Omega\ell/c)}{1 - r_1 r_2 \exp(-2i\Omega\ell/c)}. \tag{2.13}$$

Similarly, the transmission is

$$A_t(t) = e^{i\Omega(t-\ell/c)} \frac{t_1 t_2}{1 - r_1 r_2 e^{-2i\Omega\ell/c}}. \tag{2.14}$$

The intensity is

$$|A_t(t)|^2 \propto \frac{1}{1 + F\sin^2(\Omega\ell/c)}, \tag{2.15}$$

where

$$F = \frac{4r_1 r_2}{(1 - r_1 r_2)^2}. \tag{2.16}$$

When $\Omega\ell/c = n\pi$ (n is an integer), the intensity of the transmission takes the maximum value. The interval between the nth and the $(n+1)$th frequency

$$\nu_{n+1} - \nu_n = \frac{c}{2\ell} = \nu_{\mathrm{FSR}} \tag{2.17}$$

is called free spectral range (FSR) of the Fabry-Perot interferometer. On the other hand, the full width at half maximum (FWHM) of the resonance $\Delta\nu$ is

$$\frac{1}{1 + F\sin^2\left(\frac{2\pi\Delta\nu}{2}\frac{\ell}{c}\right)} = \frac{1}{2}. \tag{2.18}$$

When $\Delta\nu$ is sufficiently small,

$$\Delta\nu = \frac{c}{\pi\ell\sqrt{F}} = \frac{2}{\pi\sqrt{F}}\nu_{\mathrm{FSR}}. \tag{2.19}$$

Then, defining finesse as

$$\mathcal{F} = \frac{\pi\sqrt{F}}{2} = \frac{\pi\sqrt{r_1 r_2}}{1 - r_1 r_2}, \tag{2.20}$$

it becomes

$$\mathcal{F} = \frac{\nu_{\mathrm{FSR}}}{\Delta\nu}. \tag{2.21}$$

2.2.2 Response of the Fabry-Perot interferometer to GWs

The condition of τ_n

$$\int_{\tau_n}^{t} \frac{dt'}{\sqrt{1 + h(t')}} = \frac{2\ell}{c}n \tag{2.22}$$

yields

$$e^{i\Omega\tau_n} = e^{i\Omega(t - 2\ell n/c)}\left[1 - i\frac{\Omega}{2}\int h(\omega)e^{i\omega t}\frac{1 - e^{-2i\omega\ell n/c}}{i\omega}d\omega\right] \tag{2.23}$$

to the order of magnitude h. Using this equation, the reflection is

$$A_r(t) = e^{i\Omega t}\left[r_1 - a(\Omega) + \frac{i\Omega}{2}\int h(\omega)\frac{a(\Omega) - a(\Omega+\omega)}{i\omega}e^{i\omega t}d\omega\right]. \tag{2.24}$$

When the light is resonant in the cavity, namely $e^{-2i\Omega\ell/c} = 1$,

$$A_r(t) = e^{i\Omega t}(r_1 - \alpha_c + i\Delta_{\mathrm{GR}}(t)/2), \tag{2.25}$$

$$\Delta_{\mathrm{GR}}(t) = \int h(\omega)e^{i\omega t}H_{\mathrm{FP}}(\omega)d\omega, \tag{2.26}$$

$$H_{\rm FP}(\omega) = \frac{2\alpha_c\Omega}{\omega}\sin(\ell\omega/c)e^{-i\omega\ell/c}\frac{1}{1 - r_1r_2\exp(-2i\omega\ell/c)}, \tag{2.27}$$

$$\alpha_c = \frac{t_1^2 r_2}{1 - r_1r_2}. \tag{2.28}$$

Here, $i\Delta_{\rm GR}$ represents the side band produced by GWs. The modulus of eq.(2.27) is

$$|H_{\rm FP}(\omega)| = \frac{2\alpha_c\Omega}{\omega(1 - r_1r_2)}\frac{|\sin(\omega\ell/c)|}{\sqrt{1 + F\sin^2(\omega\ell/c)}}. \tag{2.29}$$

When $|H_{\rm FP}|$ is regarded as a function of ℓ, it has the maximum value at $\ell\omega/c = \pi/2$. When the finesse is high, it does not largely depend on ℓ. This function is plotted in Figure 2.4.

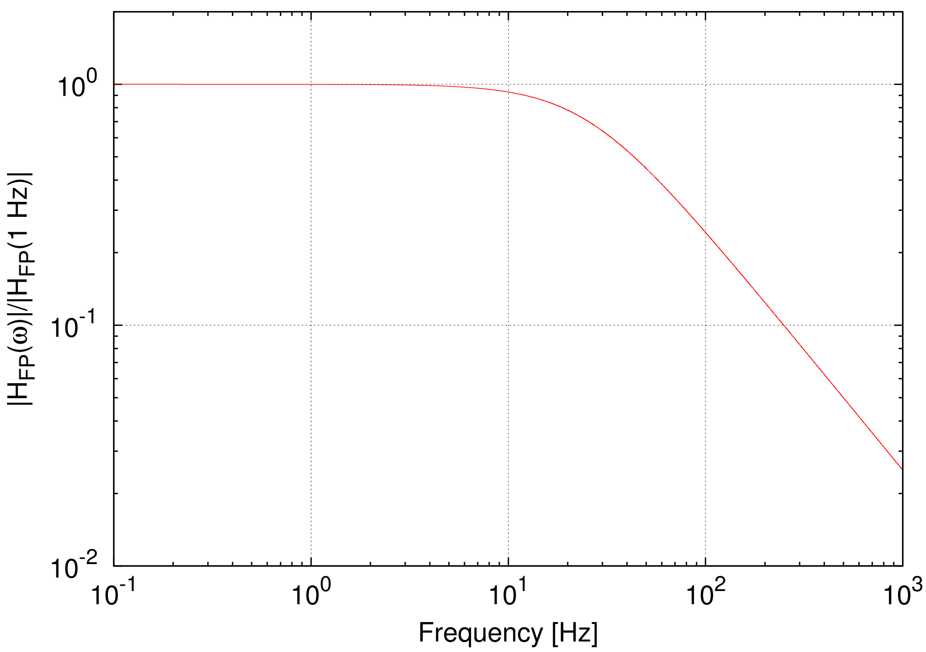

Figure 2.4: Response function of Fabry-Perot interferometer. Here, the finesse is 1000 and the arm length is 3 km.

2.3 Noise in an interferometer

2.3.1 Shot noise of light

The power spectrum of the shot noise of the photocurrent $I_{\rm P}$ is

$$\langle i_{\rm n}^2 \rangle = 2eI_{\rm P}. \tag{2.30}$$

In eq.(2.1), using $\Delta\phi = \phi_1 - \phi_2 = \Phi_0 + \delta\phi$ and $I_{\rm eff} = I_{\rm max} - I_{\rm min}$, the differential photocurrent is

$$\delta I_{\rm P} = -\frac{I_{\rm eff}}{2}\sin\Phi_0 \cdot \delta\phi. \tag{2.31}$$

If this is equal to the shot noise of the photocurrent, using an observable bandwidth Δf,

$$\frac{I_{\rm eff}}{2}\sin\Phi_0 \cdot \delta\phi_{\rm min} = \sqrt{2eI_{\rm dc}\Delta f}, \tag{2.32}$$

$$I_{\rm dc} = \frac{I_{\rm max} + I_{\rm min} + I_{\rm eff}\cos\Phi_0}{2}. \tag{2.33}$$

In an ideal case of $I_{\rm min} = 0$,

$$\delta\phi_{\rm min} = \frac{\sqrt{eI_{\rm max}(1+\cos\Phi_0)\Delta f}}{\frac{I_{\rm max}}{2}\sin\Phi_0} = \sqrt{\frac{2e}{I_{\rm max}}\Delta f}\frac{1}{\sin\frac{\Phi_0}{2}}. \tag{2.34}$$

This has the minimum value at a dark fringe $\Phi_0 = \pi$. Since the signal also becomes zero at a dark fringe, it is necessary to modulate the length of the light path. Namely, a phase modulation $\Delta\phi \to \Delta\phi + m\sin\omega_{\rm m}t$ in eq.(2.1) yields

$$\begin{aligned} I(t) &= I_{\rm min} + \frac{I_{\rm eff}}{2}[1+\cos(\Delta\phi + m\sin\omega_{\rm m}t)] && (2.35)\\ &\approx I_{\rm min} + \frac{I_{\rm eff}}{2}[1 + J_0(m)\cos\Delta\phi - 2J_1(m)\sin\Delta\phi\sin\omega_{\rm m}t + 2J_2(m)\cos\Delta\phi\cos 2\omega_{\rm m}t]. && (2.36) \end{aligned}$$

Near the dark fringe, using $\Delta\phi = \pi + \delta\phi$,

$$I(t) \approx I_{\rm min} + \frac{I_{\rm eff}}{2}[1 - J_0(m) + 2J_1(m)\delta\phi\sin\omega_{\rm m}t - 2J_2(m)\cos 2\omega_{\rm m}t]. \tag{2.37}$$

A demodulation derived from the product of this equation and $\sqrt{2}\sin\omega_{\rm m}t$ gives

$$I_{\rm s} = \sqrt{2}\frac{I_{\rm eff}}{2}J_1(m)\delta\phi. \tag{2.38}$$

Noise coming from the component of the direct current is

$$I_{\mathrm{n}} = \sqrt{2e\left\{I_{\min} + \frac{I_{\mathrm{eff}}}{2}[1 - J_0(m)]\right\}\Delta f}. \tag{2.39}$$

If one assumes $I_{\mathrm{s}} = I_{\mathrm{n}}$ when $I_{\min} = 0$, a consistent result with eq.(2.34) is obtained:

$$\delta\phi = \frac{\sqrt{eI_{\max}[1 - J_0(m)]\Delta f}}{\sqrt{2}I_{\max}J_1(m)/2} \to \sqrt{\frac{2e}{I_{\max}}\Delta f} \quad (m \to 0). \tag{2.40}$$

Using

$$I_{\max} = e\frac{\eta P}{\hbar\Omega}, \tag{2.41}$$

where P is the power of the laser and η is the quantum efficiency of the photodetector,

$$\delta\phi_{\min} = \sqrt{\frac{2\hbar\Omega}{\eta P}\Delta f}. \tag{2.42}$$

Because the minimum value of the differential phase is inversely proportional to the square root of the output of the laser power, a high-power laser is required for an interferomete-type gravitational wave detector.

The equivalent GWs' amplitude is

$$h_{\mathrm{shot}} \propto \frac{\delta\phi_{\min}}{|H_{\mathrm{FP}}|}. \tag{2.43}$$

A more precise calculation yields

$$h_{\mathrm{shot}} = \frac{1}{\tau}\sqrt{\frac{\hbar}{2\Omega P}}\sqrt{1 + (\omega\tau)^2}, \tag{2.44}$$

where $\tau = 2\mathcal{F}\ell/(\pi c)$ is the storage time of the cavity.[10]

2.3.2 Thermal noise

A general theory of thermal noise

A harmonic oscillator in a heat bath with temperature T which obeys the equation of motion

$$m\frac{d^2x}{dt^2} + \gamma\frac{dx}{dt} + kx = 0 \tag{2.45}$$

causes the Brownian motion. This is described by adding a fluctuation force to eq.(2.45):

$$m\frac{d^2x}{dt^2} + \gamma\frac{dx}{dt} + kx = f_{\rm N}(t). \tag{2.46}$$

If $f_{\rm N}$ is white noise, the correlation function is, using the Einstein relation,

$$\langle f_{\rm N}(t) f_{\rm N}(t') \rangle = 2\gamma k_B T \delta(t - t'). \tag{2.47}$$

Using $\langle f_{\rm N}(\omega)^2 \rangle = 4\gamma k_B T$, the power spectrum (per unit frequency, one-sided) of the Brownian motion is

$$\langle x(\omega)^2 \rangle = \frac{4\gamma k_B T}{|-m\omega^2 + i\omega\gamma + k|^2}. \tag{2.48}$$

Taking the limit and using $\gamma = m\omega_0/Q$,

$$\langle x(\omega)^2 \rangle \sim \frac{4k_B T}{m\omega_0^3 Q} \quad (\omega \ll \omega_0) \tag{2.49}$$

$$\sim \frac{4\omega_0 k_B T}{m\omega^4 Q} \quad (\omega \gg \omega_0), \tag{2.50}$$

which is proportional to T/Q in both cases. Thus,

1. Decreasing the temperature
2. Increasing the mechanical quality factor Q of the oscillator

are required in order to reduce the thermal noise.

Thermal oscillation of a harmonic oscillator with general dissipation

If the spring constant is complex $k \to k[1 + i\phi(\omega)]$, the equation of motion is

$$m\left\{-\omega^2 + \omega_0^2[1 + i\phi(\omega)]\right\} x(\omega) = f(\omega). \tag{2.51}$$

If

$$\phi(\omega) = \gamma\omega/k, \tag{2.52}$$

the situation is the same as in the previous discussion and $Q = 1/\phi(\omega_0)$. Even in the general case, where the fluctuation force is no longer white noise,

$$\langle f_{\rm N}(\omega)^2 \rangle = \frac{4m\omega_0^2\phi(\omega)k_B T}{\omega} \tag{2.53}$$

and

$$\langle x(\omega)^2 \rangle = \frac{4k_B T}{\omega}\frac{\omega_0^2\phi(\omega)}{m|-\omega^2 + \omega_0^2[1 + i\phi(\omega)]|^2} \tag{2.54}$$

hold (fluctuation dissipation theorem.) Taking the limit,

$$\begin{aligned}
\langle x(\omega)^2 \rangle &\sim \frac{4k_B T}{\omega} \frac{\phi(\omega)}{m\omega_0^2} \quad (\omega \ll \omega_0) &(2.55)\\
&\sim \frac{4k_B T}{\omega} \frac{\omega_0^2 \phi(\omega)}{m\omega^4} \quad (\omega \gg \omega_0). &(2.56)
\end{aligned}$$

Thermal noise of a pendulum

Because the restoring force of a pendulum is mainly gravity without loss, the dissipation is much smaller than the intrinsic dissipation (e.g. inner loss of wire.) The restoring force of a pendulum made by a mass of M and a wire of length ℓ is

$$\begin{aligned}
F &= -(Mg/\ell + k_{\rm el}[1 + i\phi(\omega)])x &(2.57)\\
&= -(Mg/\ell + k_{\rm el})[1 + i\phi_{\rm p}(\omega)]x, &(2.58)
\end{aligned}$$

where

$$\phi_{\rm p} = \frac{k_{\rm el}}{Mg/\ell + k_{\rm el}} \phi \approx \frac{k_{\rm el}\ell}{Mg} \phi. \tag{2.59}$$

Here, $k_{\rm el}$ is the spring constant due to the elasticity of the wire

$$k_{\rm el} = \frac{\sqrt{TEI}}{2\ell^2}, \tag{2.60}$$

where $T = Mg$ is the tension of the wire, E is Young's modulus and I is the wire cross section's moment of inertia. Thus,

$$\phi_{\rm p} \approx \frac{\phi}{2\ell} \sqrt{\frac{EI}{Mg}}, \tag{2.61}$$

where I is proportional to the square of the cross section and the cross section is proportional to the tension (Mg). If ϕ is independent of the tension, $\phi_{\rm p}$ is proportional to $M^{1/2}$. Eq.(2.54) shows that thermal noise (a root mean square) is proportional to $M^{-1/4}$.

Assuming that the resonant frequency is $f_{\rm p} = 1$ Hz, eq.(2.56) becomes

$$\sqrt{\langle x(\omega)^2 \rangle} \sim 3.85 \times 10^{-22} \left(\frac{T}{20\ \text{K}}\right)^{1/2} \left(\frac{30\ \text{kg}}{M}\right)^{1/2} \left(\frac{f_{\rm p}}{1\ \text{Hz}}\right) \left(\frac{\phi}{10^{-8}}\right)^{1/2} \left(\frac{100\ \text{Hz}}{f}\right)^{5/2} \ \text{m}/\sqrt{\text{Hz}}. \tag{2.62}$$

The equivalent GWs' amplitude is

$$h_{\rm thermal} = \frac{2}{\ell} \sqrt{\langle x(\omega)^2 \rangle}. \tag{2.63}$$

2.3.3 Seismic noise

A typical spectrum of seismic noise is empirically given by

$$x_{\text{seismic}} = 10^{-7} \left(\frac{1 \text{ Hz}}{f} \right)^2 \text{ m}/\sqrt{\text{Hz}}. \tag{2.64}$$

There are some places where seismic noise is less. For instance, seismic noise in Kamioka is smaller by two orders of magnitude than eq.(2.64). The equivalent sensitivity is, assuming that the vibration isolation system can decrease seismic noise by Γ_{v},

$$h_{\text{seismic}} = \Gamma_{\text{v}} \left(\frac{2x_{\text{seismic}}}{\ell} \right). \tag{2.65}$$

If $\Gamma_{\text{v}} = 10^{-3}/f^{10}$ in Kamioka[10],

$$h_{\text{seismic}} = 6.67 \times 10^{-16} \left(\frac{3 \text{ km}}{\ell} \right) \left(\frac{1 \text{ Hz}}{f} \right)^{12} /\sqrt{\text{Hz}}. \tag{2.66}$$

2.3.4 Radiation pressure noise and the quantum limit

When the light is reflected by the mirror, the mirror receives the momentum change of the light. Consequently, when the number of photons fluctuates, the force to the mirror, and then the position of the mirror fluctuate, which is called radiation pressure noise.

The force to the mirror is equal to the momentum change per unit time

$$f_{\text{ba}} = 2\frac{\hbar\Omega}{c}\frac{P}{\hbar\Omega} = \frac{2P}{c}, \tag{2.67}$$

where P is the power of the incident light. Using the mass of the mirror M, the equation of motion is

$$M\frac{d^2x}{dt^2} = f_{\text{ba}}, \tag{2.68}$$

that is, in spectrum

$$\langle x_{\text{ba}}^2(\omega) \rangle = \frac{4\langle \delta P^2(\omega) \rangle}{(M\omega^2 c)^2}. \tag{2.69}$$

When the incident light is in a coherent state,

$$\langle \delta P^2(\omega) \rangle = 2\hbar\Omega P. \tag{2.70}$$

The equivalent GWs' amplitude is

$$h_{\text{rad}} = \frac{2}{\ell}\sqrt{\langle x(\omega)_{\text{ba}}^2 \rangle} = \frac{2}{\ell}\frac{\sqrt{8\hbar\Omega P}}{M\omega^2 c}. \tag{2.71}$$

Next, the quantum uncertainty principle is described. Operators of the position and the momentum of a free mass are

$$\begin{aligned} \hat{x}(t) &= \hat{x}(0) + \frac{\hat{p}(0)t}{m}, &(2.72)\\ \hat{p}(t) &= \hat{p}(0). &(2.73) \end{aligned}$$

At a certain time τ,

$$\langle \Delta\hat{x}(\tau)^2 \rangle = \langle \Delta\hat{x}(0)^2 \rangle + \langle \Delta\hat{p}(0)^2 \rangle \frac{\tau^2}{m^2} + \langle \Delta\hat{x}(0)\Delta\hat{p}(0) + \Delta\hat{p}(0)\Delta\hat{x}(0) \rangle \frac{\tau}{m}. \tag{2.74}$$

If the third term of eq.(2.74) is negligible, the uncertainty principle

$$\sqrt{\langle \Delta\hat{x}(0)^2 \rangle \langle \Delta\hat{p}(0)^2 \rangle} \geq \frac{\hbar}{2} \tag{2.75}$$

yields

$$\langle \Delta\hat{x}(\tau)^2 \rangle \geq \langle \Delta\hat{x}(0)^2 \rangle + \frac{1}{\langle \Delta\hat{x}(0)^2 \rangle} \left(\frac{\hbar\tau}{2m} \right)^2 \geq \frac{\hbar\tau}{m}. \tag{2.76}$$

The equal sign holds when

$$\sqrt{\langle \Delta\hat{x}(0)^2 \rangle} = \sqrt{\frac{\hbar\tau}{2m}} = \Delta X_{\mathrm{SQL}}, \tag{2.77}$$

where ΔX_{SQL} is called standard quantum limit.

Taking the shot noise and the radiation pressure noise, eq.(2.42) with $\eta = 1$, (2.69) and (2.70) give

$$\langle x(\omega)^2 \rangle = \left(\frac{\lambda}{4\pi} \right)^2 \frac{2\hbar\Omega}{P} + \left(\frac{1}{m\omega^2} \right)^2 \frac{8\hbar\Omega P}{c^2} \geq \frac{4\hbar}{m\omega^2} \tag{2.78}$$

in the case of a Michelson interferometer. The equal sign holds when

$$P_{\mathrm{opt}} = \frac{m\omega^2 \lambda c}{8\pi}. \tag{2.79}$$

Eq.(2.78) is consistent with eq.(2.76) except for a factor, assuming that the bandwidth is $1/\tau$ and $\omega\tau \sim 1$.

The equivalent GWs' amplitude is

$$h_{\mathrm{SQL}} = \frac{2}{\ell} \sqrt{\langle x(\omega)^2 \rangle} = \frac{4}{\ell\omega} \sqrt{\frac{\hbar}{m}}. \tag{2.80}$$

In the case of a Fabry-Perot interferometer, a more precise calculation yields[10]

$$h_{\rm rad} = \frac{2}{\ell}\frac{\sqrt{8\hbar\Omega P}}{M\omega^2 c}\frac{2\mathcal{F}}{\pi}\frac{1}{\sqrt{1+(\omega\tau)^2}}, \tag{2.81}$$

$$h_{\rm SQL} = \frac{1}{\ell\omega}\sqrt{\frac{8\hbar}{m}} \tag{2.82}$$

instead of eqs. (2.71) and (2.80).

2.3.5 Example of noise spectrum

As an example of noise spectrum, $h_{\rm shot}$, $h_{\rm rad}$, $h_{\rm thermal}$, $h_{\rm seismic}$ and $h_{\rm SQL}$ in the case of a Fabry-Perot interferometer, namely eqs.(2.44), (2.81), (2.63), (2.66) and (2.82), are plotted in Figure 2.5, where

$$\lambda = 1064 \text{ nm}, \quad \ell = 3 \text{ km}, \quad P = 200 \text{ W}, \quad M = 30 \text{ kg}, \quad \mathcal{F} = 1000. \tag{2.83}$$

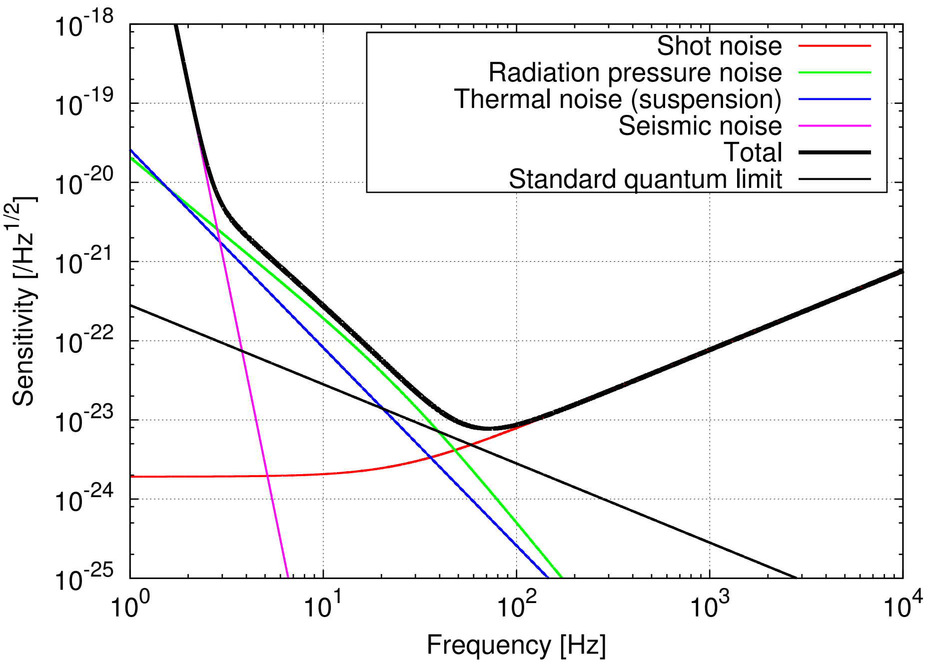

Figure 2.5: Example of noise spectrum

2.4 CLIO, CLIK and LCGT

The Large-scale Cryogenic Gravitational wave Telescope (LCGT) is an interferometric gravitational wave detector with an arm length of 3 km, which will be constructed in Kamioka mine. To reduce the thermal noise described above, the mirrors will be cooled down to cryogenic temperature (20 K) to detect GWs for the first time in the world.[2]

The Cryogenic Laser Interferometer Observatory (CLIO) is also an interferometric gravitational wave detector with cryogenic mirrors, located in Kamioka mine (an arm length is 100 m). CLIO is a prototype for preliminary research on LCGT.[11]

The Cryogenic Laser Interferometer in Kashiwa (CLIK) was a cryogenic interferometer with an arm length of 7 m located underground of the Institute for Cosmic Ray Research (ICRR), University of Tokyo. CLIK is a prototype to do research on cryocoolers since LCGT uses cryocoolers to cool the mirrors in such a way as not to cause any danger of using cooling gas underground.

Chapter 3

Thermal radiation

The mirror will be cooled down to cryogenic temperature (20 K) in LCGT to reduce the thermal noise described in the previous chapter. Interferometric gravitational wave detectors, including LCGT, use a high vacuum to prevent noise caused by fluctuation of refractive index along the light path. Thus, thermal radiation plays an important role in thermal transfer in the LCGT cryostat. In this chapter, the basic properties of thermal radiation are described.[12],[13]

3.1 Thermal radiation

Infinitesimal heat, dQ, which is radiated per unit time from an infinitesimal surface area of a body, dA, to an infinitesimal area in the (θ, ϕ) direction on a unit sphere, dA', is proportional to dA and $dA' \cos\theta$,

$$dQ = I(\theta, \phi) dA dA' \cos\theta. \tag{3.1}$$

Here, the intensity of radiation, $I(\theta, \phi)$, generally includes radiation with various wavelengths. Now, assuming that $I_\lambda(\lambda, \theta, \phi)d\lambda$ includes radiation within a wavelength range of $\lambda \sim \lambda + d\lambda$,

$$I(\theta, \phi) = \int_0^\infty I_\lambda(\lambda, \theta, \phi) d\lambda. \tag{3.2}$$

Using

$$dA' = \sin\theta d\theta d\phi, \tag{3.3}$$

eq.(3.1) becomes

$$dQ = I(\theta, \phi) dA \sin\theta \cos\theta d\theta d\phi. \tag{3.4}$$

Thus, the total heat radiated from dA is

$$Q = dA \int_0^\infty d\lambda \int_0^{2\pi} d\phi \int_0^{\frac{\pi}{2}} \sin\theta \cos\theta d\theta I_\lambda(\lambda, \theta, \phi). \tag{3.5}$$

Heat radiated per unit time and unit surface area, called emissive power, is

$$E = \frac{Q}{dA} = \int_0^\infty d\lambda \int_0^{2\pi} d\phi \int_0^{\frac{\pi}{2}} \sin\theta \cos\theta d\theta I_\lambda(\lambda, \theta, \phi). \tag{3.6}$$

Using monochromatic emissive power, defined as:

$$E_\lambda = \int_0^{2\pi} d\phi \int_0^{\frac{\pi}{2}} \sin\theta \cos\theta d\theta I_\lambda(\lambda, \theta, \phi), \tag{3.7}$$

one can obtain

$$E = \int_0^\infty E_\lambda d\lambda. \tag{3.8}$$

If I_λ is independent of the direction of radiation, (θ, ϕ), eq.(3.6) and eq.(3.7) become

$$E = \int_0^\infty I_\lambda d\lambda \int_0^{2\pi} d\phi \int_0^{\frac{\pi}{2}} \sin\theta \cos\theta d\theta \quad = \quad \pi I, \tag{3.9}$$

$$E_\lambda = I_\lambda \int_0^{2\pi} d\phi \int_0^{\frac{\pi}{2}} \sin\theta \cos\theta d\theta \quad = \quad \pi I_\lambda. \tag{3.10}$$

3.2 Black body radiation

3.2.1 Definition of a black body

A black body is defined as follows:

1. It absorbs all radiation of any wavelength coming from any direction.
2. It emits the largest intensity of thermal radiation at the same temperature and wavelength among any surface.
3. The intensity of its radiation is independent of the direction of the radiation.

3.2.2 Planck's law

The energy density of electromagnetic waves within a frequency range from ν to $\nu + d\nu$ is

$$D_\nu = \frac{8\pi h}{c^3} \frac{\nu^3}{e^{h\nu/kT} - 1} d\nu, \tag{3.11}$$

where h is Planck's constant, k is Boltzmann's constant, c is the speed of light and T is temperature. Using the wavelength λ,

$$D_\nu = \frac{8\pi hc}{\lambda^5 (e^{hc/k\lambda T} - 1)} d\lambda. \tag{3.12}$$

The black body intensity per unit solid angle and unit wavelength, $I_{\lambda,b}$, is

$$I_{\lambda,b} = \frac{c}{4\pi} D_\nu = \frac{2hc^2}{\lambda^5 (e^{hc/k\lambda T} - 1)}. \tag{3.13}$$

Eq.(3.10) gives the monochromatic emissive power of a black body,

$$E_{\lambda,b} = \pi I_{\lambda,b} = \frac{2\pi hc^2}{\lambda^5 (e^{hc/k\lambda T} - 1)}, \tag{3.14}$$

which is called Planck's law.

3.2.3 Wien's displacement law

The wavelength where the monochromatic emissive power of a black body has the maximum value at temperature T, $\lambda_{\max}(T)$, is a solution of

$$\frac{\partial E_{\lambda,b}}{\partial \lambda} = 0. \tag{3.15}$$

In eq.(3.14), using $x = hc/k\lambda T$, this condition becomes

$$x = 5(1 - e^{-x}) \to x = 4.965, \tag{3.16}$$

namely,

$$\lambda_{\max} T = 2898\ \mu\text{m K}. \tag{3.17}$$

This is called Wien's displacement law.

3.2.4 Stefan-Boltzmann law

Eq.(3.8) and eq.(3.14) give the Stefan-Boltzmann law,

$$E_b = \int_0^\infty E_{\lambda,b} d\lambda = \int_0^\infty \frac{2\pi hc^2}{\lambda^5 (e^{hc/k\lambda T} - 1)} d\lambda = \sigma T^4, \tag{3.18}$$

where σ is the Stefan-Boltzmann constant.

3.3 Emissivity

Because of the definition of a black body, the emissive power and the monochromatic emissive power of an actual body are smaller than those of a black body. Then, the ratio to a black body,

$$\epsilon_\lambda = \frac{E_\lambda}{E_{\lambda,b}}, \tag{3.19}$$

is called monochromatic emissivity and

$$\epsilon = \frac{E}{E_b} \tag{3.20}$$

is called total emissivity or simply emissivity. Namely, the heat of radiation per unit time from an actual body (surface area S), Q is

$$\frac{Q}{S} = \epsilon\sigma T^4. \tag{3.21}$$

In addition, a body that satisfies the following conditions is called a gray body:

- Its monochromatic emissivity ϵ_λ is a constant independent of the wavelength, $\epsilon_\lambda = \epsilon$.
- Its radiation intensity is independent of the direction of radiation.
- Its reflection of incident thermal radiation with any incident angle is isotropic.

The directional emissivity indicates the dependence on the zenith angle θ:

$$\epsilon_\theta = \frac{\int_0^\infty d\lambda \int_0^{2\pi} d\phi I_\lambda(\lambda,\theta,\phi)}{\int_0^\infty d\lambda \int_0^{2\pi} d\phi I_{\lambda,b}(\lambda)} = \frac{\int_0^\infty d\lambda \int_0^{2\pi} d\phi I_\lambda(\lambda,\theta,\phi)}{2\pi \int_0^\infty d\lambda I_{\lambda,b}(\lambda)}. \tag{3.22}$$

The directional emissivity of bodies with high electrical conductivity tends to increase as θ increases while that of bodies with low electrical conductivity tends to increase as θ decreases.

3.4 Kirchhoff's law

Assuming that the reflectivity and absorptivity of a body for all wavelengths is r and α, respectively,

$$r + \alpha = 1 \tag{3.23}$$

if there is no transmissivity. Next, this body (surface area S) is surrounded by a black body with temperature T, as shown in Figure 3.1. When the body and the black body are in thermal equilibrium, the temperature of the body is also T and radiates heat

$$\epsilon\sigma T^4 S. \tag{3.24}$$

On the other hand, α of the heat radiation from the black body is absorbed by the body and r returns to the black body. Thus, the body absorbs

$$\alpha\sigma T^4 S. \tag{3.25}$$

Due to thermal equilibrium, eq.(3.24) and eq.(3.25) are equal,

$$\epsilon = \alpha = 1 - r. \tag{3.26}$$

This discussion also holds for a certain wavelength λ, using reflectivity for wavelength λ, r_λ:

$$\epsilon_\lambda = 1 - r_\lambda. \tag{3.27}$$

This is called Kirchhoff's law.

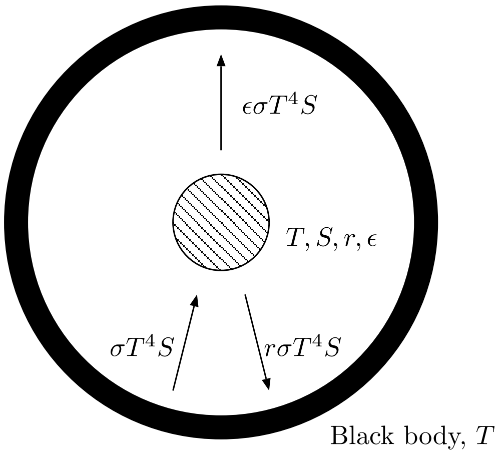

Figure 3.1: Derivation of Kirchhoff's law

3.5 Heat transfer by radiation

This section describes heat transfer by radiation among gray bodies.

3.5.1 View factor

One can consider gray bodies i, j whose surface areas are A_i, A_j, respectively, as shown in Figure 3.2. Using the emissive power of i, $E_i(=\pi I_i)$, heat radiated to all solid angle is $E_i A_i$. Using heat that comes to j of this value, Q_{ij}, the view factor is defined as

$$F_{ij} = \frac{Q_{ij}}{E_i A_i} = \frac{Q_{ij}}{\pi I_i A_i}. \tag{3.28}$$

Other names for this factor are radiation shape factor, angle factor, and configuration factor. From this definition, F_{ij} between surfaces whose radiation doesn't come into each other directly,

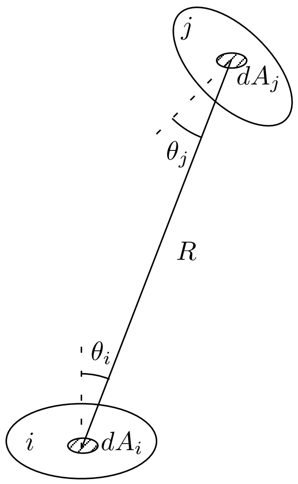

Figure 3.2: View factor

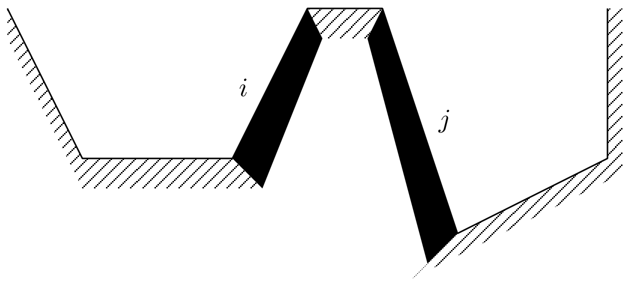

Figure 3.3: Surfaces whose radiation doesn't come into each other directly.

shown in Figure 3.3, is of course zero. In addition, $F_{ii} = 0$ for surfaces whose radiation doesn't come to itself, such as flat or convex planes, while $F_{ii} \neq 0$ for concave planes.

Next, one can consider infinitesimal areas dA_i, dA_j on i, j. The length of the line between dA_i and dA_j is R. Angles between this line and the normal to dA_i, dA_j are θ_i, θ_j. Heat from dA_i to dA_j is, replacing dA' (unit distance) in eq.(3.1) with $dA_j \cos\theta_j / R^2$,

$$dQ_{ij} = \frac{I_i \cos\theta_i \cos\theta_j}{R^2} dA_i dA_j. \tag{3.29}$$

Thus,

$$A_i F_{ij} = \frac{Q_{ij}}{E_i} = \int_{A_i} dA_i \int_{A_j} dA_j \frac{\cos\theta_i \cos\theta_j}{\pi R^2}. \tag{3.30}$$

This equation yields

$$A_i F_{ij} = A_j F_{ji}. \tag{3.31}$$

3.5.2 Heat transfer by radiation in a gray-body system

Figure 3.4 shows a closed-space system composed of gray bodies i $(i = 1, 2, \cdots, n)$ with surface area A_i, emissivity ϵ_i and temperature T_i. In this case, thermal radiation from a certain surface i comes to any surfaces directly:

$$F_{i1} + F_{i2} + \cdots + F_{ii} + \cdots + F_{in} = \sum_{j=1}^{n} F_{ij} = 1. \tag{3.32}$$

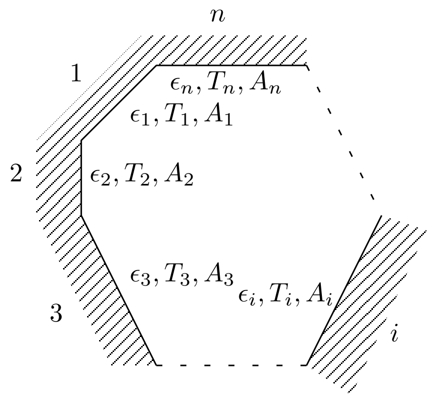

Figure 3.4: Closed space system composed of gray bodies.

It is very complicated to trace the infinite reflection among the n surfaces in order to calculate the heat transfer from surface i to surface j. Then, one can introduce radiosity G_i, which represents the total heat radiated from surface i per unit area (= radiation from itself + reflection of radiation). Due to the fact that the reflectivity is equal to $1 - \epsilon_i$ from eq.(3.26),

$$G_i = \epsilon_i \sigma T_i^4 + \frac{1-\epsilon_i}{A_i} \sum_{k=1}^{n} A_k G_k F_{ki} \tag{3.33}$$

$$= \epsilon_i \sigma T_i^4 + (1-\epsilon_i) \sum_{k=1}^{n} G_k F_{ik}, \tag{3.34}$$

where eq.(3.31) is used. On the other hand, the net heat radiated from surface i, Q_i, is

$$\frac{Q_i}{A_i} = G_i - \frac{1}{A_i} \sum_{k=1}^{n} A_k G_k F_{ki} \tag{3.35}$$

$$= G_i - \sum_{k=1}^{n} G_k F_{ik}. \tag{3.36}$$

These equations can extinguish the term $\sum G_k F_{ik}$:

$$Q_i = \frac{\sigma T_i^4 - G_i}{\frac{1-\epsilon_i}{\epsilon_i A_i}}. \tag{3.37}$$

The net heat radiated from surface i to surface j, Q_{ij}, is

$$Q_{ij} = G_i A_i F_{ij} - G_j A_j F_{ji} = A_i F_{ij} (G_i - G_j) \tag{3.38}$$

$$= \frac{G_i - G_j}{\frac{1}{A_i F_{ij}}}. \tag{3.39}$$

Here, σT_i^4, G_i can be regarded as being voltages; Q_i, Q_{ij} can be regarded as being electric current. Eq.(3.37) means that the current Q_i flows in the resistance between σT_i^4 and G_i:

$$R_i = \frac{1-\epsilon_i}{\epsilon_i A_i}. \tag{3.40}$$

Eq.(3.39) means that the current Q_{ij} flows in the resistance between G_i and G_j:

$$R_{ij} = \frac{1}{A_i F_{ij}}. \tag{3.41}$$

3.5.3 Some examples

Two parallel planes

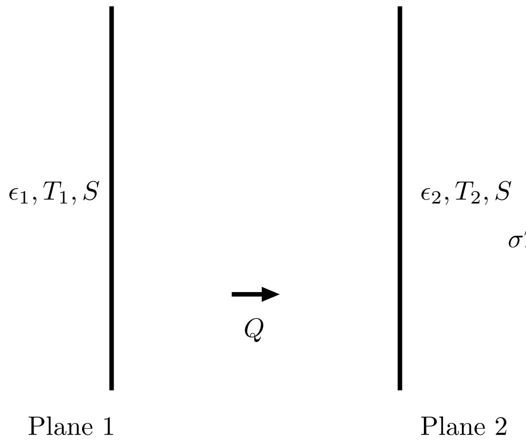

Figure 3.5: Two parallel planes

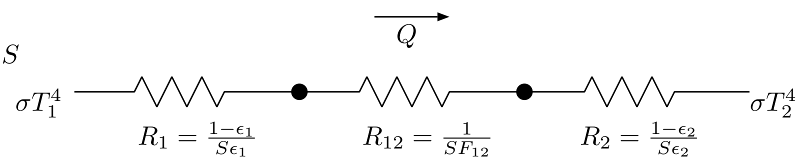

Figure 3.6: Equivalent circuit

The equivalent circuit of the two parallel planes 1,2 with sufficiently large surface areas, shown in Figure 3.5, is given in Figure 3.6. Using the fact that $F_{11} = F_{22} = 0$ and that eq.(3.32) gives $F_{12} = F_{21} = 1$, the heat transferred by radiation, Q, is

$$\begin{aligned} Q &= \frac{\sigma(T_1^4 - T_2^4)}{R_1 + R_{12} + R_2} && (3.42) \\ &= \frac{\sigma S(T_1^4 - T_2^4)}{\frac{1}{\epsilon_1} + \frac{1}{\epsilon_2} - 1} && (3.43) \\ &= \epsilon' \sigma S(T_1^4 - T_2^4), && (3.44) \end{aligned}$$

where

$$\epsilon' = \frac{1}{\frac{1}{\epsilon_1} + \frac{1}{\epsilon_2} - 1}. \tag{3.45}$$

Shields

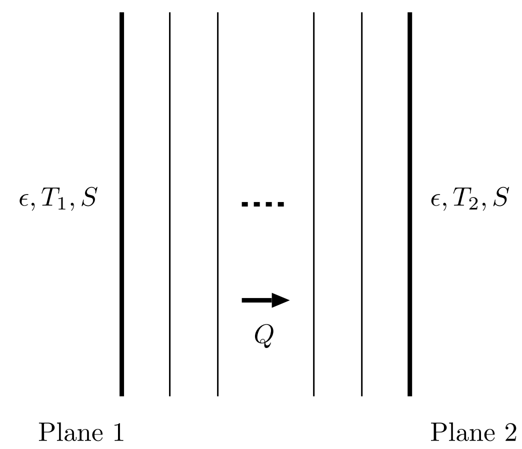

Figure 3.7: Shields

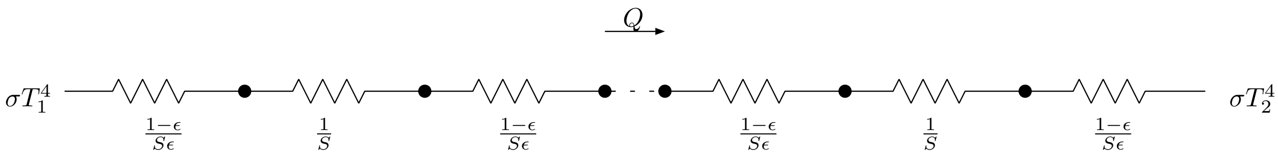

Figure 3.8: Equivalent circuit

In the case where n shields with emissivity ϵ and area S are introduced between plane 1 and plane 2 (here, assuming $\epsilon_1 = \epsilon_2 = \epsilon$),

$$Q = \frac{1}{n+1} \frac{\sigma S(T_1^4 - T_2^4)}{\frac{2}{\epsilon} - 1} = \frac{1}{n+1} \epsilon' \sigma S(T_1^4 - T_2^4). \tag{3.46}$$

The heat transfer is reduced by $1/(n+1)$.

Surrounded gray body

Figure 3.9 shows that convex gray body 1 with surface area A_1, emissivity ϵ_1 and temperature T_1 is surrounded by gray body 2 with surface area A_2, emissivity ϵ_2 and temperature T_2. In this case, $F_{11} = 0$, eq.(3.31) and eq.(3.32) give

$$F_{12} = 1, \quad F_{21} = \frac{A_1}{A_2}, \quad F_{22} = 1 - F_{21} = \frac{A_2 - A_1}{A_2}. \tag{3.47}$$

The equivalent circuit is shown in Figure 3.10. The radiated heat per unit time is

$$Q = \frac{\sigma(T_1^4 - T_2^4)}{R_1 + R_{12} + R_2} = \frac{\sigma A_1(T_1^4 - T_2^4)}{\frac{1}{\epsilon_1} + \frac{A_1}{A_2}\left(\frac{1}{\epsilon_2} - 1\right)}. \tag{3.48}$$

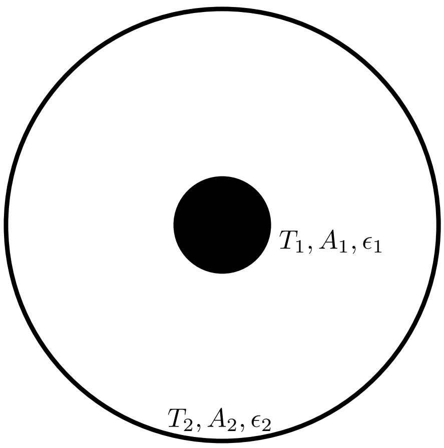

Figure 3.9: Surrounded gray body

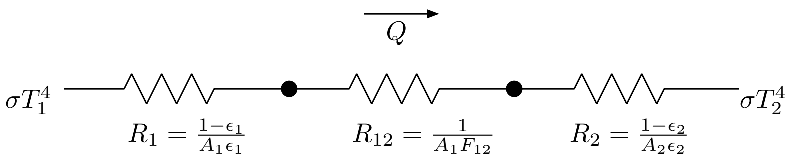

Figure 3.10: Equivalent circuit

Chapter 4

Reflectivity Measurements (Metals)

Thermal radiation plays an important role in heat transfer in the LCGT cryostat. Thus, in order to calculate the radiation, it is necessary to know the emissivity of materials at low temperature for the radiation shields. In this chapter, measurements of metals are described. A part of these results is published in [14].

Although there is much published data on the emissivity at low-temperature metals (e.g. [15]-[20]), it is mostly data of metals with the highest fineness or the best surface treatment. On the other hand, the radiation shields in LCGT have a large surface area (approximately several m^2), and thus the fineness and surface treatment that can be used are limited. Because there is little data on the emissivity at low temperature of metals with practical fineness and a practical surface treatment, it was necessary to measure it. The reflectivity of samples that are candidates for the radiation shields in LCGT was measured using a CO_2 laser with wavelength $\lambda = 10.59$ μm, where black body radiation of 300 K has the largest intensity.

4.1 Theory about the dependence of the reflectivity of metal on the temperature

Before presenting the measurements, a theory is described about the dependence of the reflectivity of metals on the temperature.[22]

First, let's consider the relationship between the electrical conductivity of materials σ and the permittivity ε. Maxwell's equations in materials are given as follows:

$$\nabla \cdot \mathbf{D} = \rho, \tag{4.1}$$

$$\nabla \cdot \mathbf{B} = 0, \tag{4.2}$$

$$\nabla \times \mathbf{E} = -\frac{\partial \mathbf{B}}{\partial t}, \tag{4.3}$$

$$\nabla \times \mathbf{H} = \mathbf{j} + \frac{\partial \mathbf{D}}{\partial t}, \tag{4.4}$$

where $\mathbf{D}$ is the electric displacement, $\mathbf{B}$ the magnetic induction, $\mathbf{E}$ the electric field, $\mathbf{H}$ the magnetic vector, ρ the electric charge density and $\mathbf{j}$ the electric current density.

In the case of uniform and isotropic materials, $\mathbf{j} = \sigma \mathbf{E}$, $\mathbf{D} = \varepsilon \mathbf{E}$ and $\mathbf{B} = \mu \mathbf{H}$, eq.(4.4) becomes

$$\nabla \times \mathbf{B} = \mu \left(\sigma \mathbf{E} + \varepsilon \frac{\partial \mathbf{E}}{\partial t} \right). \tag{4.5}$$

In metals, $\rho = 0$, eq.(4.1) is

$$\nabla \cdot \mathbf{E} = 0. \tag{4.6}$$

Eqs.(4.3), (4.5) and (4.6) yield

$$\nabla^2 \mathbf{E} = \mu \varepsilon \frac{\partial^2 \mathbf{E}}{\partial t^2} + \mu \sigma \frac{\partial \mathbf{E}}{\partial t}. \tag{4.7}$$

The assumption that the electric field is $\mathbf{E} = \mathbf{E}_0 e^{-i\omega t}$ and that the materials are nonmagnetic, where $\mu = \mu_0$ (μ_0 is the magnetic permeability of vacuum), gives

$$\nabla^2 \mathbf{E} + \mu_0 \omega^2 \left(\varepsilon + i \frac{\sigma}{\omega} \right) \mathbf{E} = 0. \tag{4.8}$$

This equation, using $\varepsilon = \varepsilon_0$ (ε_0 is the permittivity of vacuum), $\sigma = 0$, yields an equation that holds in a vacuum:

$$\nabla^2 \mathbf{E} + \mu_0 \omega^2 \varepsilon_0 \mathbf{E} = 0, \tag{4.9}$$

that is,

$$\nabla^2 \mathbf{E} + \frac{\omega^2}{c^2} \mathbf{E} = 0. \tag{4.10}$$

From a comparison between eq.(4.8) and eq.(4.9), the relative permittivity $\hat{\varepsilon}$ is

$$\hat{\varepsilon} = \frac{\varepsilon}{\varepsilon_0} + i \frac{\sigma}{\omega \varepsilon_0}. \tag{4.11}$$

The model of P. Drude is now described as a theory of reflectivity. The equation of motion of a free electron (velocity $\mathbf{v}$, mass m, electric charge $-e$) in metals is, using the electric field $\mathbf{E}$ and the relaxation time τ,

$$m \dot{\mathbf{v}} = -e \mathbf{E} - m \frac{\mathbf{v}}{\tau}. \tag{4.12}$$

Assuming that the electric field is written as $\mathbf{E} = \mathbf{E}_0 e^{-i\omega t}$, its periodic solution is

$$\mathbf{v} = \frac{(-e)\tau}{m(1 - i\omega\tau)}\mathbf{E}. \tag{4.13}$$

The current density $\mathbf{j}$ is, using the number density of free electrons, N,

$$\mathbf{j} = (-e)N\mathbf{v} = \frac{Ne^2\tau}{m(1 - i\omega\tau)}\mathbf{E}. \tag{4.14}$$

It represents that

$$\sigma = \frac{Ne^2\tau}{m(1 - i\omega\tau)} \tag{4.15}$$

and that

$$\sigma_0 = \frac{Ne^2\tau}{m} \tag{4.16}$$

for a static electric field.

Substituting eq.(4.15) for eq.(4.11), and neglecting the contribution of the bound electrons, namely using $\varepsilon = \varepsilon_0$, one can obtain

$$\hat{\varepsilon} = n^2 = 1 - \frac{Ne^2\tau}{m\varepsilon_0}\frac{1}{\omega(\omega\tau + i)}, \tag{4.17}$$

where n is the complex refractive index. The reflectivity R_λ is given by

$$R_\lambda = \left|\frac{n-1}{n+1}\right|^2, \tag{4.18}$$

and absorptivity α_λ is

$$\alpha_\lambda = 1 - R_\lambda. \tag{4.19}$$

For example, calculations about copper and aluminum are shown in Figure 4.1. The value of σ_0 was first calculated from the dependence of the electrical resistivity of copper[21] or aluminum[23] on the temperature. Next, τ was calculated, using eq.(4.16), and eq.(4.19) is plotted.

Here, $\omega = 2\pi c/\lambda = 1.78 \times 10^{14}$ rad/s ($\lambda = 10.59$ μm). The parameters for copper are $N = \varrho N_A/A = 8.49 \times 10^{28}$ /m^3, where $\varrho = 8.96$ g/cm^3 is the mass density of copper[24], $A = 63.55$ is the atomic weight of copper, and N_A is the Avogadro number. The parameters for aluminum are $N = \varrho N_A/A = 6.02 \times 10^{28}$ /m^3, where $\varrho = 2.70$ g/cm^3 is the mass density of aluminum[24] and $A = 26.98$ is its atomic weight.

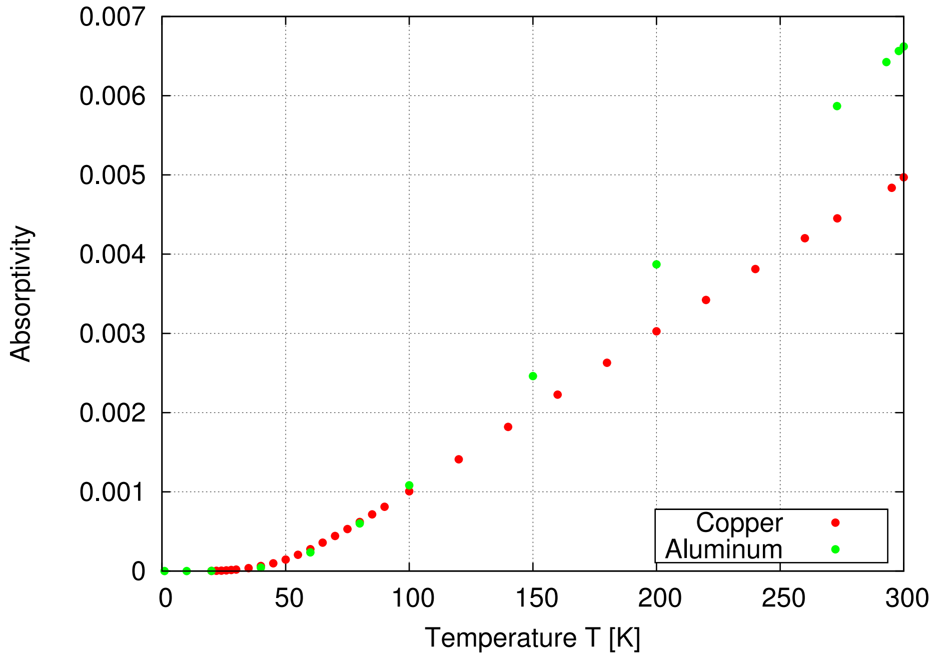

Figure 4.1: Dependence of the absorptivity at 10.59 μm on temperature predicted by Drude's model.

4.2 Measured samples

Four samples (Cu, 6NAl, AlECB, A1070) were measured. The Cu sample was oxygen-free copper class-1 (fineness more than 99.99%) with the surface polished by sandpaper (Figure 4.2, Figure 4.3). The 6NAl sample was aluminum of fineness 99.9999% with the surface precisely lathed using a diamond bit (Figure 4.4, Figure 4.5). The AlECB sample was aluminum 1100 with the surface prepared by an electrochemical buffing (ECB) treatment[25] after being polished to an average roughness of Ra = 0.8 μm using a milling machine (Figure 4.6, Figure 4.7). The A1070 sample was aluminum 1070 with a chemically polished (CP) surface (Figure 4.8, Figure 4.9). Every sample had a disk form; the 6NAl sample was 37 mm in diameter and 6 mm in thickness; the other samples were 30 mm in diameter and 5 mm in thickness.

4.3 Preliminary measurements

This section describes preliminary measurements to estimate the stability of the laser power and the precision of the power meter, which are necessary to evaluate the error of reflectivity measurements.

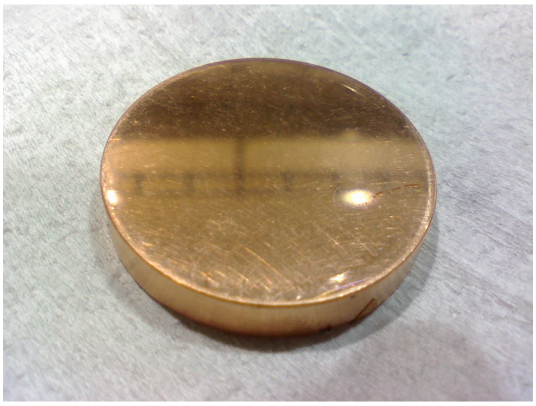

Figure 4.2: Overview: Cu sample

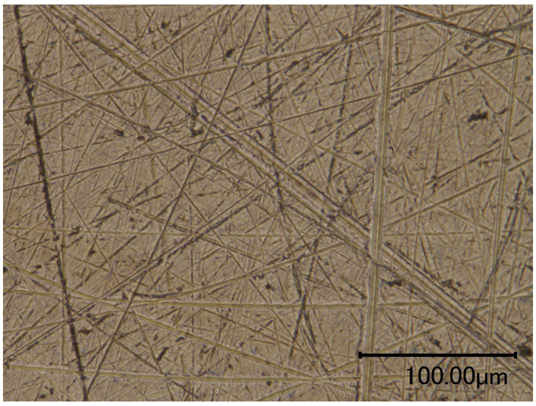

Figure 4.3: Micrograph of the surface: Cu sample

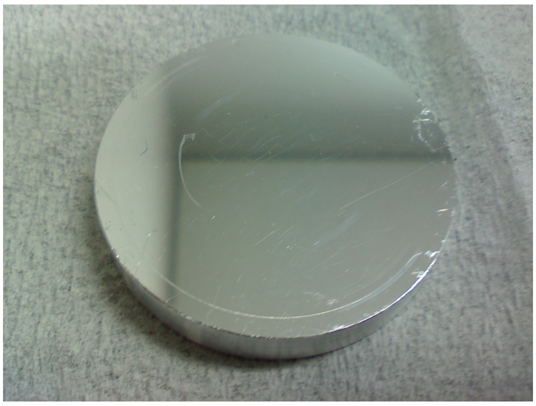

Figure 4.4: Overview: 6NAl sample

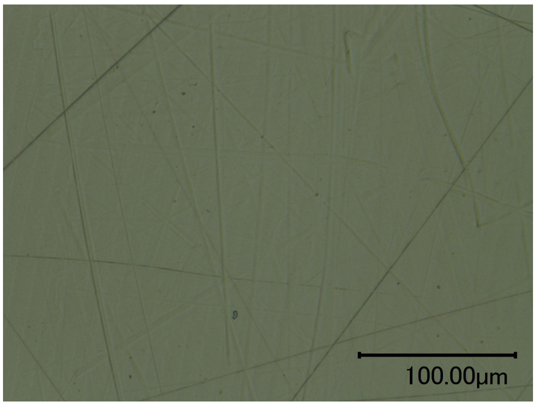

Figure 4.5: Micrograph of the surface: 6NAl sample

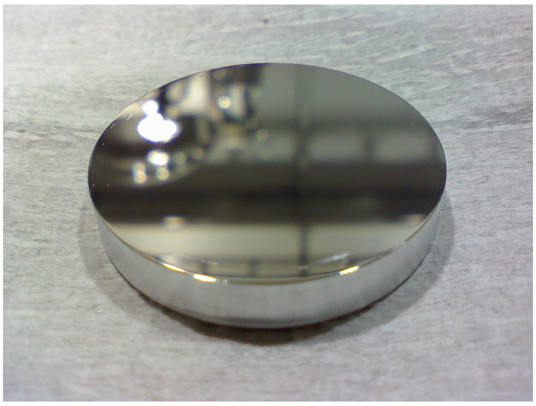

Figure 4.6: Overview: AlECB sample

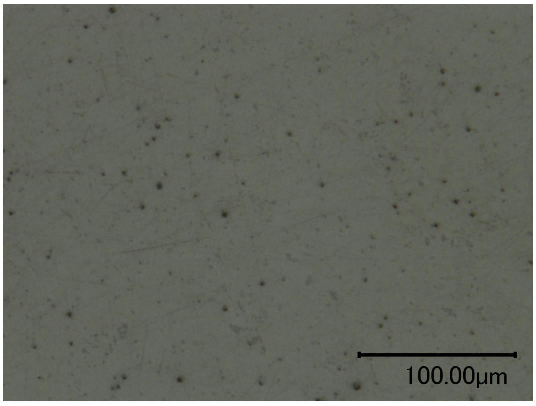

Figure 4.7: Micrograph of the surface: AlECB sample

Figure 4.8: Overview: A1070 sample

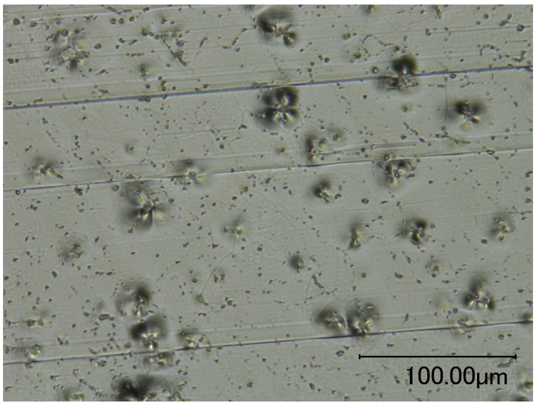

Figure 4.9: Micrograph of the surface: A1070 sample

Date and time	Measured value[W] ($\pm$ is its fluctuation)
2010/7/2	6.27$\pm$0.06
2010/7/5 18:30	6.24$\pm$0.03
2010/7/7 16:30	6.22$\pm$0.03

Table 4.1: Measured value of the power meter when laser light comes directly to the power meter.

4.3.1 Laser turned on and off

Since the laser was turned on and off repeatedly in measurements at room temperature, the stability of the laser power and the precision of the power meter were measured in that case.

Method

The fluctuation of the measured value of the power meter was examined when the laser light directly came to the power meter. The power meter used here, model AC5000, of SCIENTECH inc., measures the temperature change of the black surface that absorbs the laser light. Then, it converts it to the power of the laser and outputs a voltage signal proportional to the laser power. Here, the measured value and its fluctuation were recorded when the laser light came to the power meter for a several minutes and the increase of the measured value became saturated. This measurement was repeated at different dates.

Result

The measured value of the intensity of the laser is given in Table 4.1. From this result, the stability of the laser power and the precision of the power meter turned out to be at most 1 % (value on 2010/7/2).

4.3.2 Laser continuously turned on

Since the laser was turned on for a long time in measurements at cryogenic temperature, the stability of the laser power and the precision of the power meter were measured in that case. The output voltage of the power meter was sampled every 10 seconds.

Method

The fluctuation of the measured value of the power meter was examined when the laser light came directly to the power meter.

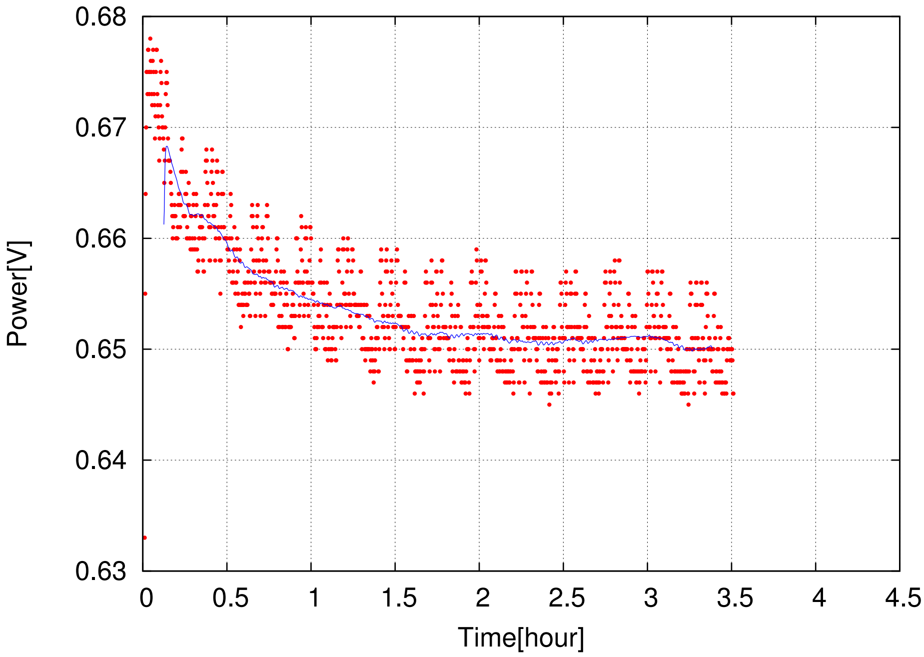

Figure 4.10: Measured change over time of the power meter when the laser beam comes directly to the power meter (2010/11/12 am)

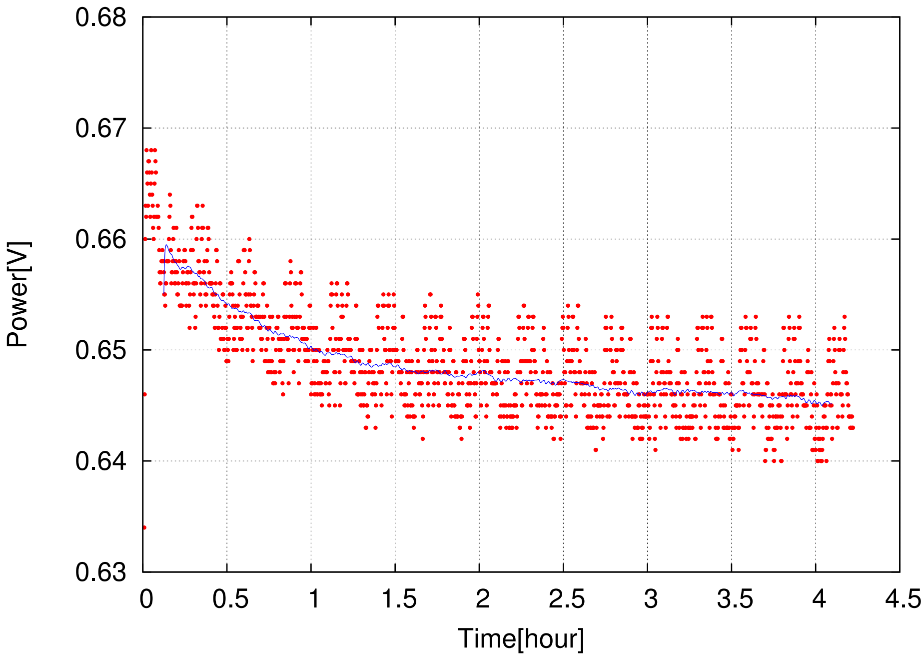

Figure 4.11: Measured change over time of the power meter when the laser beam comes directly to the power meter (2010/11/12 pm)

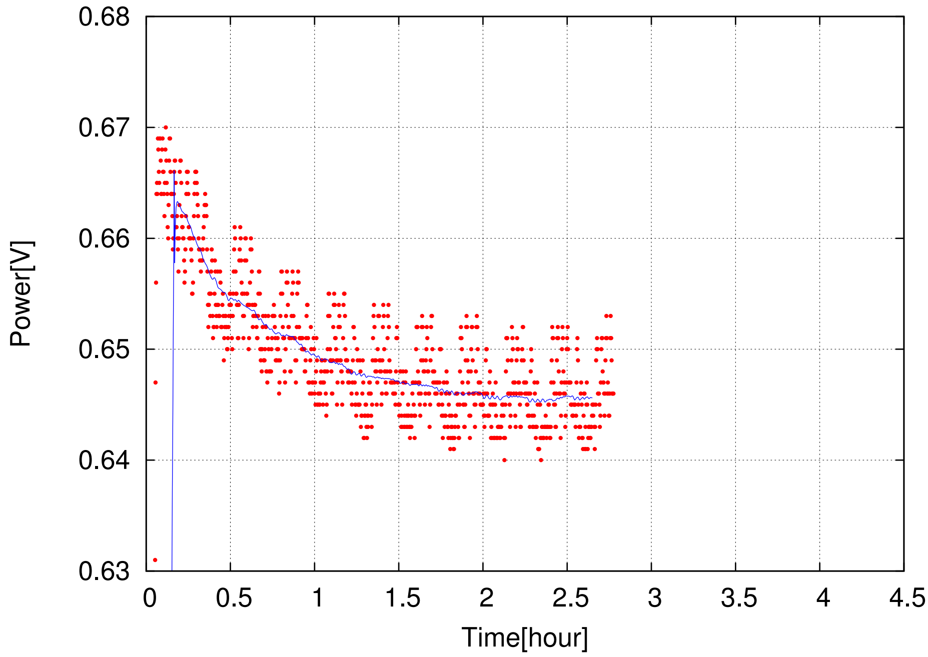

Figure 4.12: Measured change over time of the power meter when the laser beam comes directly to the power meter (2010/11/15 pm)

Result

The change in the measured value when the laser light came directly to the power meter is plotted in Figures 4.10-4.12. These results show that the measured value is 0.648± 0.007 V since two hours after the laser was turned on. Namely, the stability of the laser power including the precision of the power meter was approximately 1 %. For this reason, in reflectivity measurements at cryogenic temperature, the cooling and measurement were started more than two hours after the laser was turned on.

4.4 Method of measurements

4.4.1 Measurements at room temperature

The arrangement shown in Figure 4.13 was set up to measured the absorptivity of each sample at room temperature by making the samples reflect the CO_2 laser (wavelength $\lambda = 10.59$ μm).

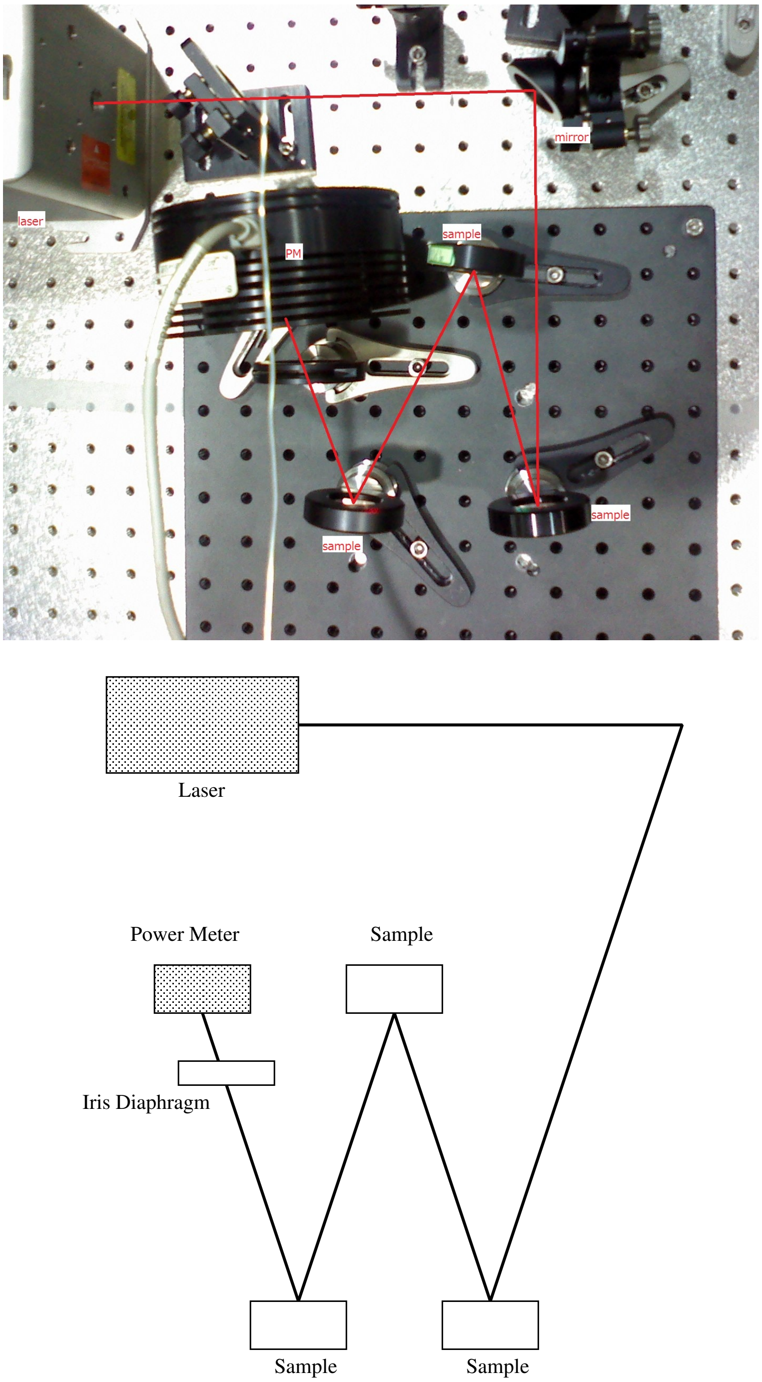

Figure 4.13: Experimental setup for measurements at room temperature for the case that the number of reflections is $\mathcal{N} = 3$

In other words, the reflectivity at room temperature, R_0, was obtained by

$$R_0 = \left(\frac{\mathcal{P}}{\mathcal{P}_0}\right)^{1/\mathcal{N}}, \tag{4.20}$$

where $\mathcal{P}$ is the power of the laser after $\mathcal{N}$ ($\mathcal{N} = 1 \sim 3$) reflections, measured by the power meter, and $\mathcal{P}_0$ is the power of the laser before a reflection measured by the same power meter. Then,

$$\alpha = 1 - R_0. \tag{4.21}$$

was obtained. The power after the reflections $\mathcal{P}$ was measured by the power meter as a function of the diameter of the aperture of the iris diaphragm to confirm that almost all of the power of the laser reflected or scattered by the samples was detected. Namely, one can confirm this when $\mathcal{P}$ becomes a constant as the diameter of the aperture becomes larger.

4.4.2 Measurements at cryogenic temperature

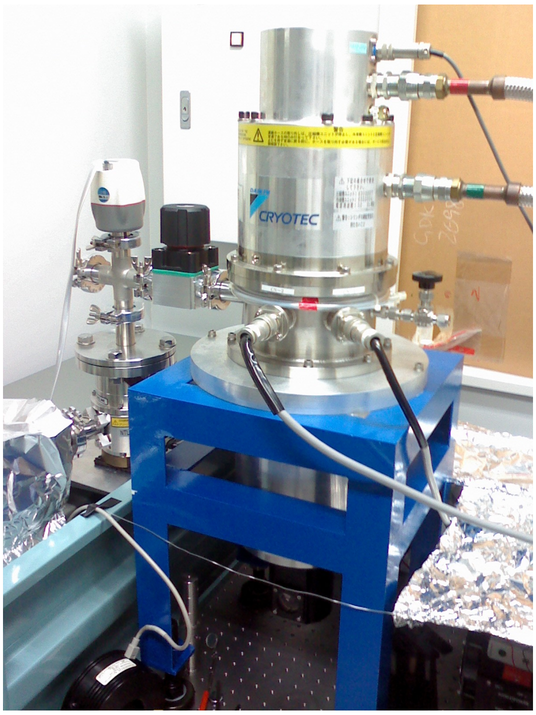

Figure 4.14: 4 K pulse tube cryocooler used in this experiment

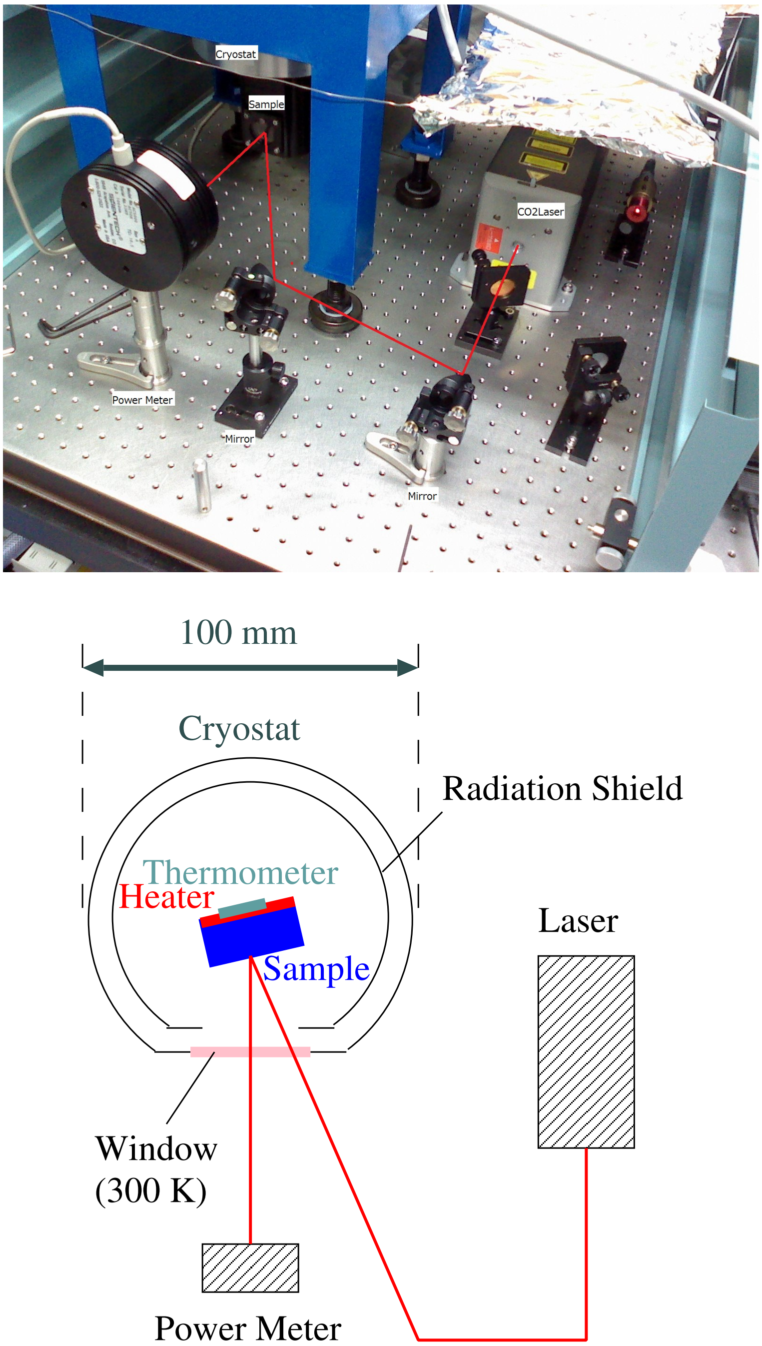

Figure 4.15: Experimental setup for measurements at cryogenic temperature. The cryostat was cooled by a 4 K pulse tube cryocooler with double stages, whose 1st stage is connected to the radiation shield and 2nd stage is connected to the sample.

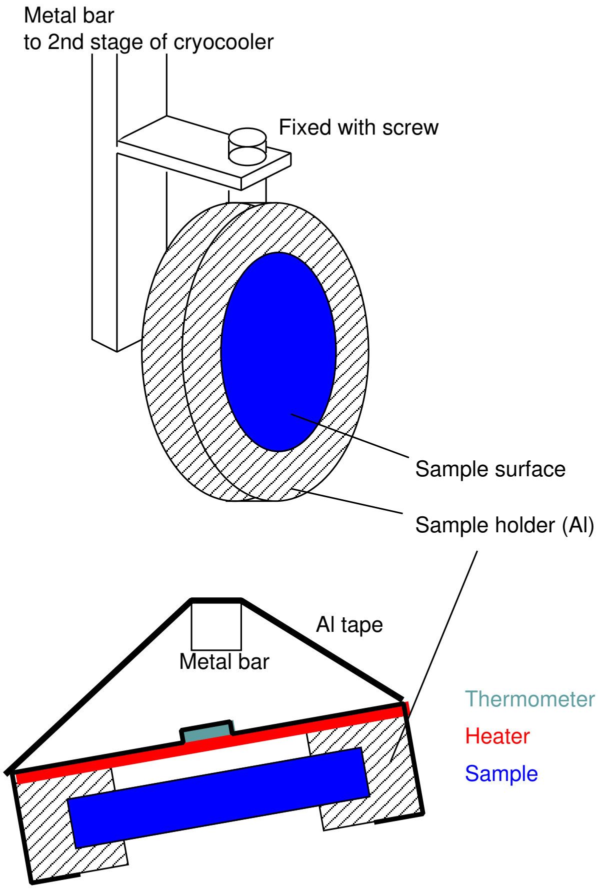

Figure 4.16: Schematic diagram of how to fix the Cu, AlECB samples)

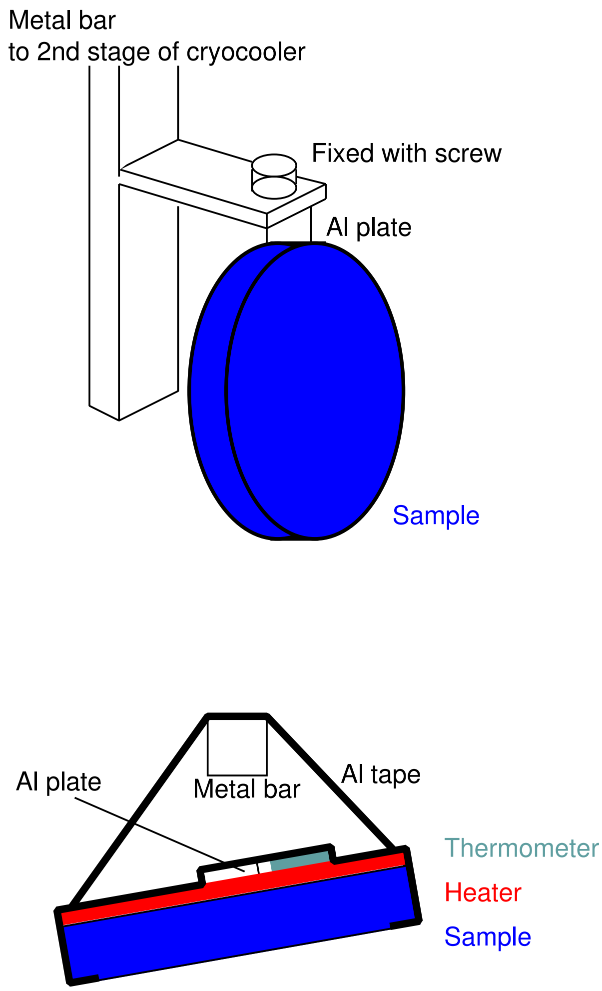

Figure 4.17: Schematic diagram of how to fix the 6NAl, A1070, DLC, AlTiN samples (DLC and AlTiN samples are described in chapter 5)

The optical system shown in Figure 4.15 was set up to measure the power of the CO_2 laser after reflection at the sample in the cryostat by the power meter; it was recorded together with the temperature of the sample. The cryostat was cooled by a 4 K pulse tube cryocooler with double stages (made by CRYOTEC, shown in Figure 4.14), whose 1st stage is connected to the radiation shield and 2nd stage is connected to the sample. Here, a silicon diode DT-670-SD, made by Lake Shore Cryotronics and attached on the back side of the sample, measured the temperature of the sample.To prevent residual gas from contaminating the surface of the sample and changing the reflectivity, the pressure was sufficiently reduced ($\sim 10^{-4}$ Pa.) Also, a heater was attached on the back side (the other side than the side that reflects the laser beam) of the sample, as shown in Figures 4.16,4.17, which always kept the temperature of the sample higher than that of the surrounding, even when cooling or heating the sample. Heating the sample was done by the heater while the cryocooler was on basically, and the cryocooler was stopped only when the heater power could not heat up the sample because stopping the cryocooler would increase the temperature around the sample rapidly, increase the pressure and cause the gas to contaminate the surface of the sample. Cooling and heating was repeated to confirm the reflectivity reproduced at the same temperature.

Next, the absolute value of the reflectivity in the cryogenic temperature was obtained using the result of the reflectivity measured at room temperature. Specifically, the reflectivity $R(T)$ was calculated on the basis of the value of the power meter at room temperature (300 K) $\mathcal{P}(T = 300 \text{ K})$ by

$$R(T) = R_0 \frac{\mathcal{P}(T)}{\mathcal{P}(T = 300 \text{ K})}, \tag{4.22}$$

where $\mathcal{P}(T)$ is the value of the power meter at temperature T and R_0 is the reflectivity at room temperature. Here, the average of the output of the power meter during approximately 10 minutes was used as $\mathcal{P}(T)$ to cancel the fluctuation of the laser power while the output voltage of the power meter was sampled every 10 seconds. Then, the absorptivity, α, was obtained as

$$\alpha = 1 - R. \tag{4.23}$$

4.5 Results of measurements

4.5.1 Measurements at room temperature

The power after the reflections, divided by the power of the laser before the reflection, $\mathcal{P}/\mathcal{P}_0$, as a function of the diameter of the aperture of the iris diaphragm is given in Figure 4.18. Then, using the constant that $\mathcal{P}/\mathcal{P}_0$ reaches to as the diameter of the aperture becomes larger, the result given in Table 4.2 was obtained.

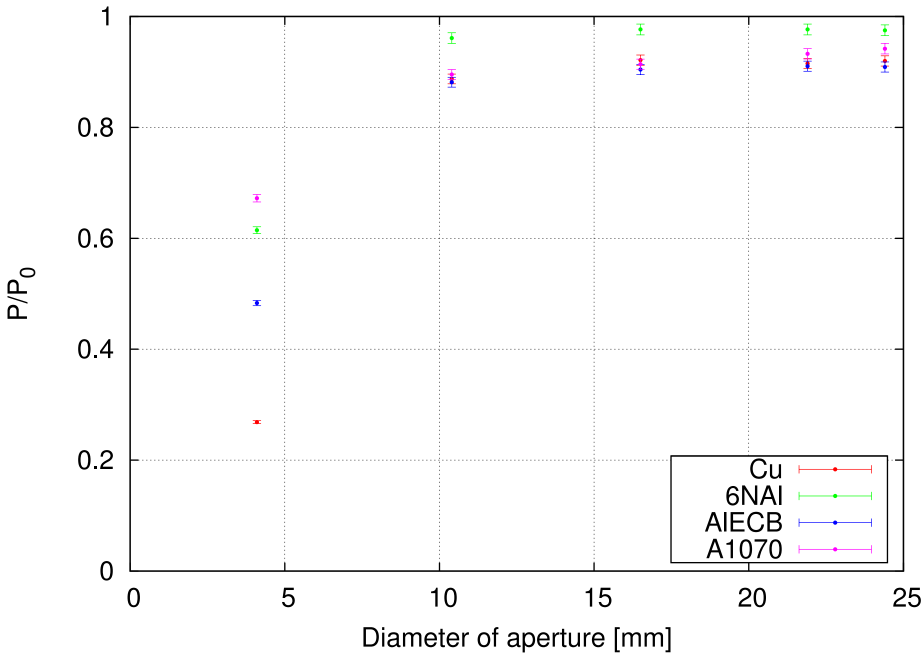

Figure 4.18: Power after the reflections divided by the power of the laser before the reflection, $\mathcal{P}/\mathcal{P}_0$, as a function of the diameter of the aperture of the iris diaphragm. The error bars show an error of 1% from the precision of the power meter and the fluctuation of the intensity of the laser.

Sample	$\mathcal{N}$	Absorptivity at 300 K
Cu	3	0.028±0.003
6NAl	1	0.024±0.010
AlECB	3	0.032±0.003
A1070	1	0.063±0.010

Table 4.2: Absorptivity at room temperature and the number of reflections, $\mathcal{N}$, of each sample

4.5.2 Measurements at cryogenic temperature

The relationship between the temperature and the absorptivity of each sample is shown in Figures 4.19-4.22. In these figures, plural plots at a certain temperature represent the results of repetitive measurements. The value of the temperature has errors of several K.

The change in temperature of the 6NAl sample as a representative during a measurement is shown in Figure 4.23; ON/OFF of the heater and the cryocooler at each time is given in Table 4.3.

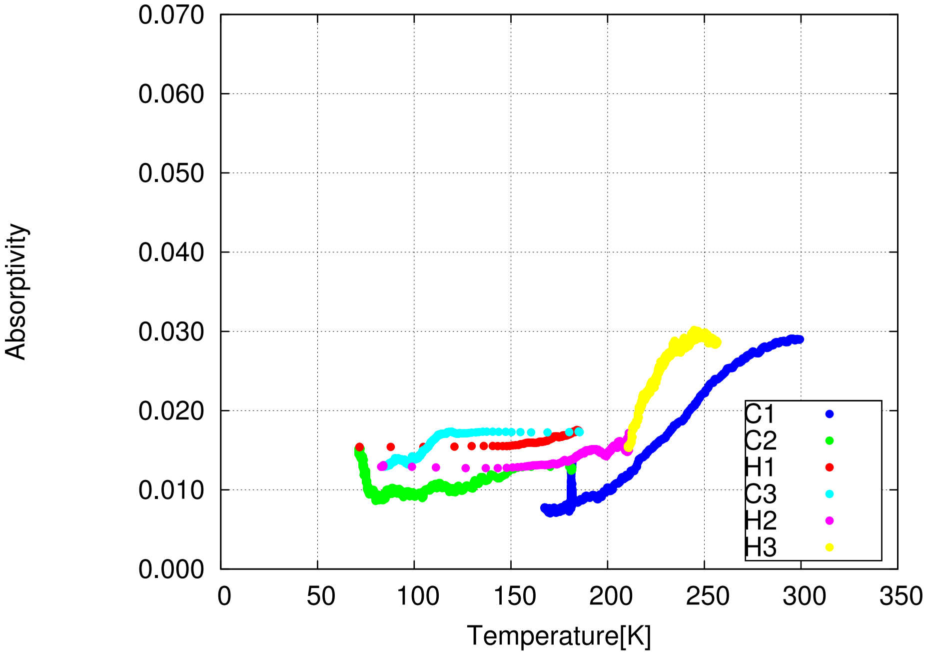

Figure 4.19: Relationship between temperature and absorptivity of the Cu sample. Plural plots at one temperature represent the results of repetitive measurements. The meanings of the legends are given in Table 4.3.

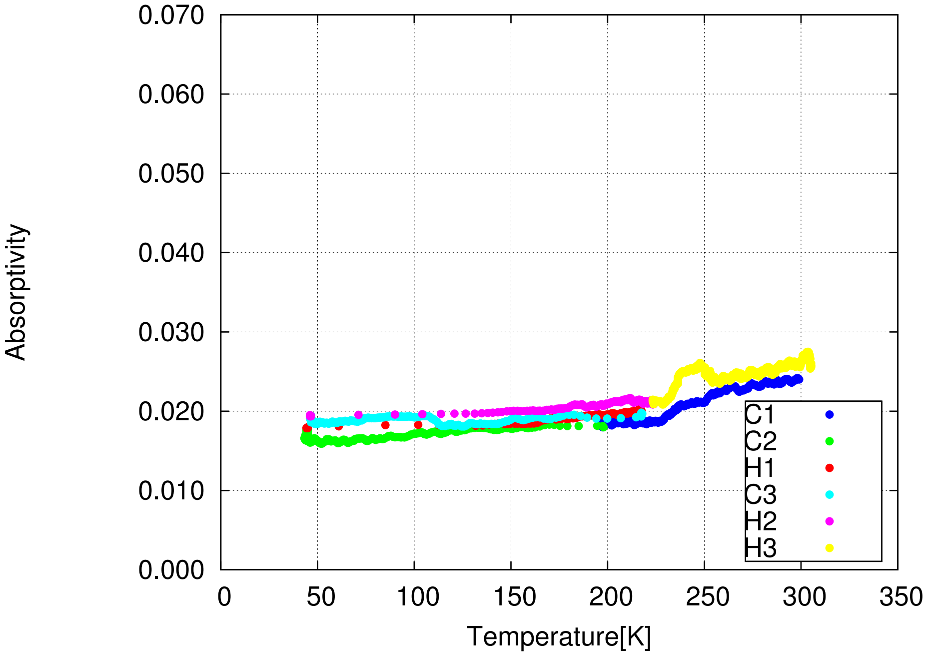

Figure 4.20: Relationship between temperature and absorptivity of the 6NAl sample.

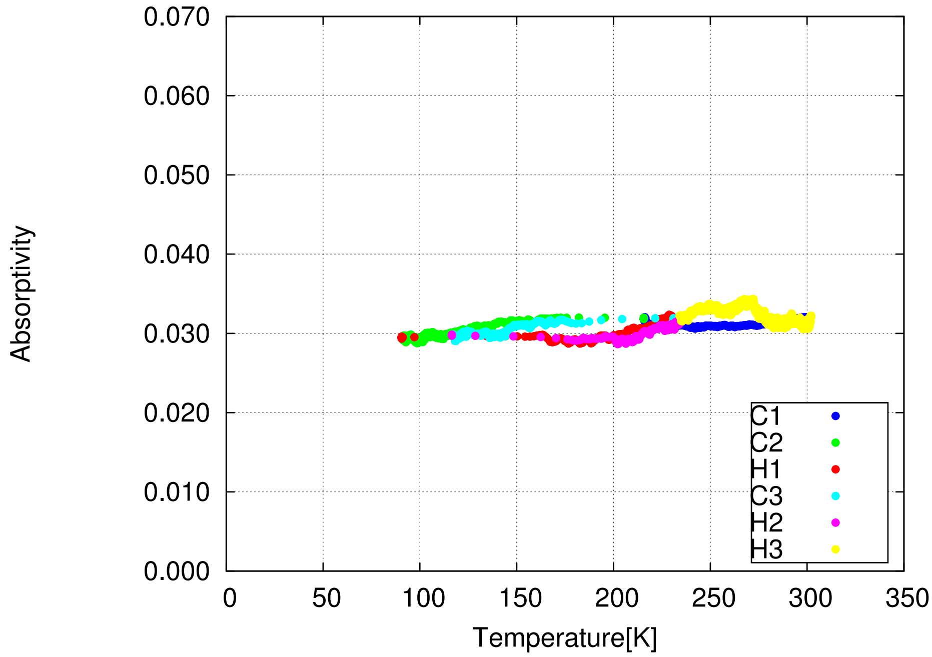

Figure 4.21: Relationship between temperature and absorptivity of the AlECB sample.

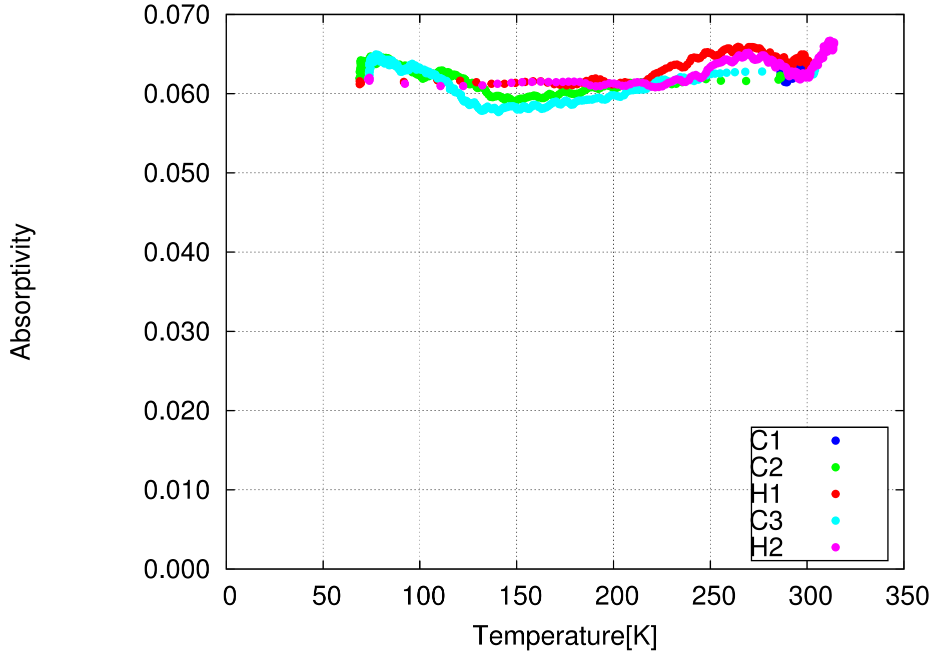

Figure 4.22: Relationship between temperature and absorptivity of the A1070 sample.

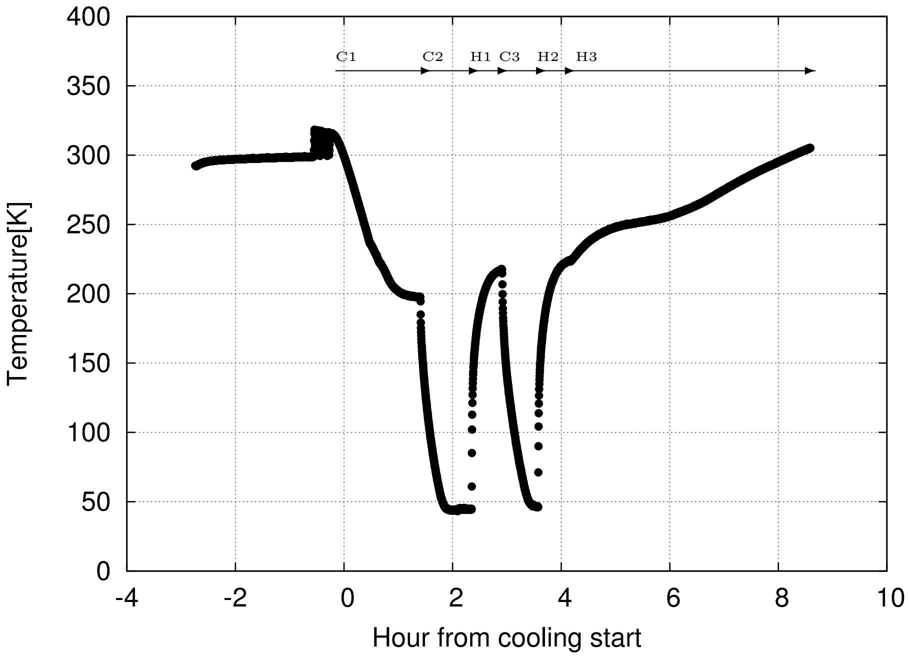

Figure 4.23: Temperature change with time

		Heater	Cryocooler
C1	Cooling	ON	ON
C2	Cooling	OFF	ON
H1	Heating	ON	ON
C3	Cooling	OFF	ON
H2	Heating	ON	ON
H3	Heating	ON	OFF

Table 4.3: Heater and cryocooler turned on and off

4.6 Error analysis

4.6.1 Measurements at room temperature

The results of the measurements at room temperature have errors that come mainly from:

1. the precision of the power meter,
2. the fluctuation of the intensity of the laser,

3. the scattering on the surfaces of the samples.

The precision of the power meter and the fluctuation of the intensity of the laser were 1 %, as described in subsection 4.3.1. On the other hand, the accuracy of the power meter was 3 %, which did not have any effect on the values of the reflectivity because $\mathcal{P}$ and $\mathcal{P}_0$ in Eq(4.20) were measured by the same power meter.

To prevent the laser from scattering on the surfaces of the samples as possible, the samples whose surfaces are regarded as mirrors, that is, whose surface roughness are sufficiently small were used. Moreover, Figure 4.18 confirms that more than 99 % of the power of the laser reflected or scattered by the sample is detected because the power becomes constant within 1 % at more than 20 mm in the diameter of the aperture.

To sum up these errors, the error in $\mathcal{P}/\mathcal{P}_0$ of each sample is approximately 1 %. Thus, the error in the absorptivity is approximately $1/\mathcal{N}$ %, which is given in Table 4.2.

4.6.2 Measurements at cryogenic temperature

The results of the measurements at cryogenic temperature have errors that come mainly from:

1. the precision of the power meter,

2. the fluctuation of the intensity of the laser.

Measuring the relative value, as shown in Eq.(4.22), makes it unnecessary to take into account the scattering on the surface of the sample because one can assume that the angular distribution of the scattering doesn't have any difference between room temperature and the cryogenic temperature. Also, it is unnecessary to take into consideration the absorption or the scattering of the laser by the window of the vacuum chamber BaF_2 because the deformation of the window can be neglected since both $\mathcal{P}(T = 300\ \mathrm{K})$ and $\mathcal{P}(T)$ in Eq.(4.22) were measured under a vacuum and one can assume that the window is always at room temperature.

Also, here, the precision of the power meter and the fluctuation of the intensity of the laser were 1 %, as described in subsection 4.3.2. The accuracy of the power meter doesn't have any effect on the values of the reflectivity.

As a result, the value of the reflectivity has systematic errors of about 1 %, which come from $\mathcal{P}(T = 300\ \mathrm{K})$ and R_0, and random errors of about 1%, which come from the precision of the power meter and the fluctuation of the intensity of the laser. Namely, the value of the absorptivity has systematic errors of about 0.01 (absolute error) and random errors of about 0.01 (absolute error). In total, the measured values of absorptivity have an uncertainty of about 0.02.

Even if these errors are large compared with other measurements (e.g. [15]-[20]), the safety margin for the heat load will be taken when cryostat is designed, and these errors are not problematic for the design of the cryostat.

4.7 Discussion

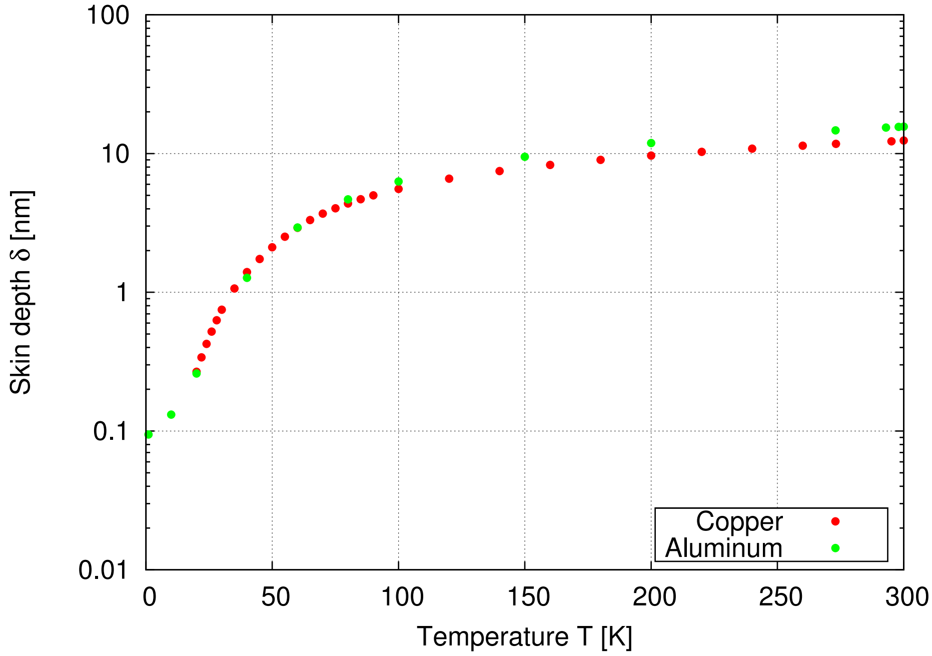

Figure 4.24: Dependence of the skin depth on temperature

Figure 4.1 shows that the absorptivity of copper and aluminum decreases as the temperature decreases. On the other hand, taking account of random errors of about 0.01 in the absorptivity, no tendency was clearly found for the reflectivity to increase, that is, for the absorptivity to decrease as the temperature decreases in the case of aluminum (Figures 4.20-4.22). However, it was found in the case of copper (Figure 4.19). Moreover, fluctuation of the absorptivity of copper at one temperature is larger than that of aluminum. I speculate that this fact has something to do with surface treatment or thickness of oxide on the surface of the sample. The estimation of the effect of this surface condition is a future work.

The typical thickness of the oxide naturally formed on aluminum and copper surface is the order of several nm.[26],[27] On the other hand, the typical length where the electromagnetic wave can intrude into metal (skin depth) is

$$\delta = \sqrt{\frac{2}{\sigma\omega\mu_0}}, \tag{4.24}$$

where $\omega = 2\pi c/\lambda = 1.78 \times 10^{14}$ rad/s ($\lambda = 10.59$ μm). The calculated values of the skin depth using the resistivity of copper[21] and aluminum[23] are plotted in Figure 4.24. The skin depth is comparable with the thickness of the oxide at 50 K and reaches to the value larger than the thickness of the oxide by one order of magnitude as the temperature rises. Although the effect of the oxide on the reflectivity is small at room temperature, this can be large at cryogenic temperature. Also, the thickness of the oxide can change over time. For the LCGT, the change over several years is important. The examination of the change of the thickness of the oxide on the surface of the metal and the relationship between the thickness of the oxide and the reflectivity is a future issue.

Comparing the measured value with Figure 4.1, one can see that the measured value is approximately several to 10 times larger. This means that the dissipation $1/\tau$ of real metal is larger than that from the contribution of the electrical resistivity (eq.(4.16)). Measurement of the surface electrical resistivity of the sample itself at cryogenic temperature and its comparison with the reflectivity will produce useful result. However, the surface electrical resistivity of the disk form metal is difficult to be measured because it is too small. Although the electrical resistivity of fine fiber metal can be measured more easily, it is generally different from the surface resistivity.

Comparing the measured value with previously published data (e.g. [15]-[20]), one finds that the measured values of copper and aluminum are generally larger by approximately 0.01-0.04 though [15] reported higher values than the measured ones. This comes from the practical fineness and the practical surface treatment used here because the impurity or imperfection on the surface can increase the emissivity of metals.

The absorptivity was reproduced at the same temperature within random errors of 0.01 in Figures 4.19-4.22.

Chapter 5

Reflectivity Measurements (Metal with high emissivity coatings)

In this chapter, measurements of metal with high emissivity coatings are described. The measurement methods were almost the same as those for metals except that some improvement was achieved because the high absorptivity led to the fact that the sample was more heated by the laser.

5.1 Measured samples

Two samples (DLC, AlTiN) were measured. The DLC sample was an aluminum A1070 sample with a chemically polished (CP) surface coated with Diamond Like Carbon (DLC) (1.0 μm in thickness; Figure 5.1, Figure 5.2). The AlTiN sample was an aluminum A1070 sample with a CP surface coated with AlTiN (1.0 μm in thickness; Figure 5.3, Figure 5.4). Each sample had a disk form: 30 mm in diameter and 5 mm in thickness.

5.2 Preliminary measurements

In this section, preliminary measurements to estimate the stability of the laser power and the precision of the power meter are describe, which are necessary to evaluate the error of reflectivity measurements.

5.2.1 Laser turned on and off

Since the laser was turned on and off repeatedly in measurements at room temperature, the stability of the laser power and the precision of the power meter were measured in that case.

Figure 5.1: Overview: DLC sample

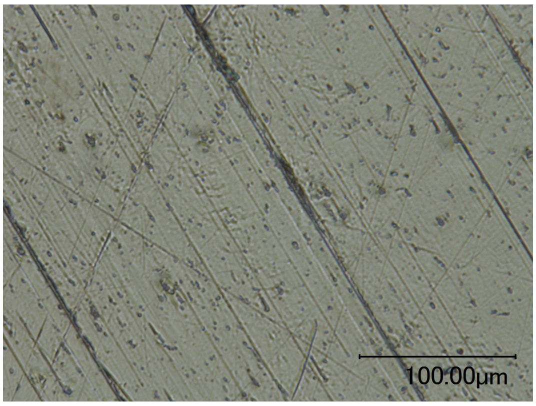

Figure 5.2: Micrograph of the surface: DLC sample

Figure 5.3: Overview: AlTiN sample

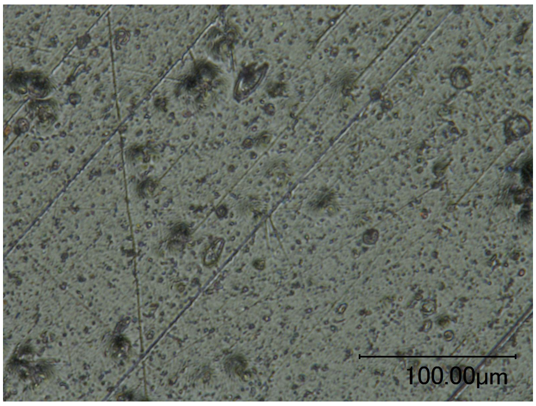

Figure 5.4: Micrograph of the surface: AlTiN sample

Method

Same as subsection 4.3.1 in the previous chapter. These measurements were repeated because another CO_2 laser was used.

Result

The measured value of the intensity of the laser is given in Table 5.1. From this result, the stability of the laser power and the precision of the power meter turned out to be at most 1 %. As an example, Figure 5.5 gives the typical change over time of the output voltage of the power meter.

Date and time	Measured value[V] (± is its fluctuation)
2011/6/17 11:00	2.63±0.03
2011/6/17 18:30	2.58±0.02
2011/6/22 11:00	2.63±0.03
2011/6/22 17:30	2.58±0.03

Table 5.1: Measured value of the power meter when the laser beam comes directly to the power meter. Figure 5.5 shows the typical change over time of the output voltage of the power meter.

5.2.2 Laser continuously turned on

High absorptivity leads to the fact that the laser light absorbed by the sample becomes a larger heat load on the cryocooler. Thus, the laser was turned on for 3 minutes and turned off for 7 minutes repeatedly in measurements at cryogenic temperature. The result was obtained from the average values from 1.5 to 3 minutes since the laser was turned on while the output voltage of the power meter was sampled every 10 seconds. Here, the stability of the laser power and the precision of the power meter were measured in that case.

Method

The fluctuation of the measured value of the power meter was examined when the laser beam came directly to the power meter.

Result

The change of the measured value when the laser beam came directly to the power meter is plotted in Figure 5.6. This result shows that the average of every measured value is 2.645 ±

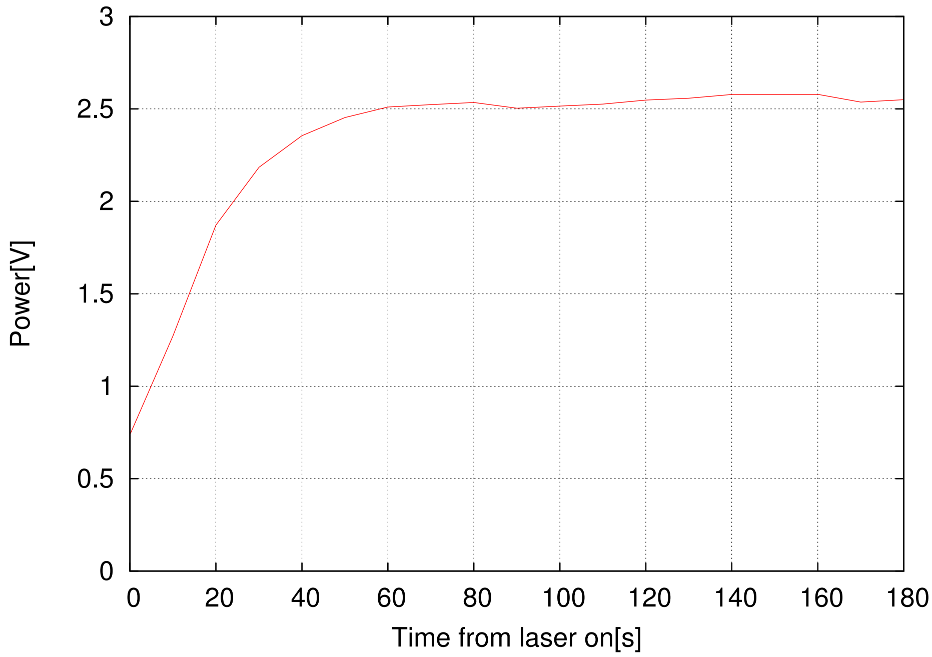

Figure 5.5: Typical change over time of the output voltage of the power meter

0.018; namely, the stability of the laser power, including the precision of the power meter, is approximately 0.7 %.

5.3 Method of measurements

5.3.1 Measurements at room temperature

Same as subsection 4.4.1 in the previous chapter. The experimental setup is shown in Figure 5.7.

5.3.2 Measurements at cryogenic temperature

The experimental setup is shown in Figure 5.7. Similar to subsection 4.4.2 in the previous chapter except for the following points.

The laser was turned on for 3 minutes and turned off for 7 minutes repeatedly. The result was obtained from the average values from 1.5 to 3 minutes since the laser was turned on while the output voltage of the power meter was sampled every 10 seconds. The average values of the thermometer in that time were used as the temperature of the sample. If the value of the

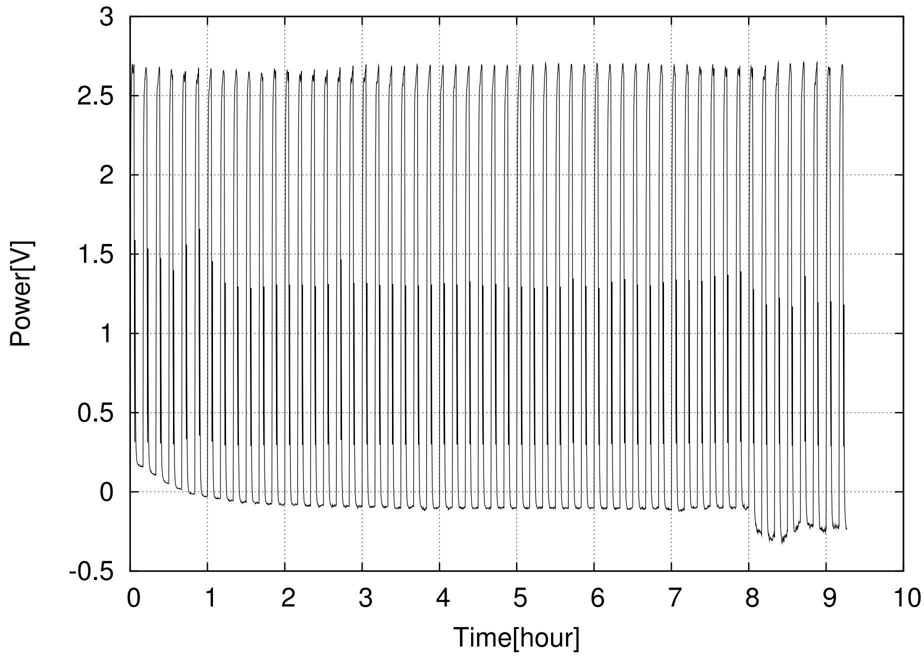

Figure 5.6: Change over time of the measured value when the laser beam comes directly to the power meter.

Sample	$\mathcal{N}$	Absorptivity at 300 K
DLC	1	0.41±0.01
AlTiN	1	0.27±0.01

Table 5.2: Absorptivity at room temperature and the number of reflections, $\mathcal{N}$, of each sample

thermometer changed by more than 6 K from the 1.5 to 3 minutes, the obtained result was discarded.

5.4 Results of measurements

5.4.1 Measurements at room temperature

The power after the reflections divided by the power of the laser before the reflection, $\mathcal{P}/\mathcal{P}_0$, as a function of the diameter of the aperture of the iris diaphragm is given in Figure 5.9. Then, using the constant which $\mathcal{P}/\mathcal{P}_0$ comes to as the diameter of the aperture becomes larger, the result given in Table 5.2 was obtained.

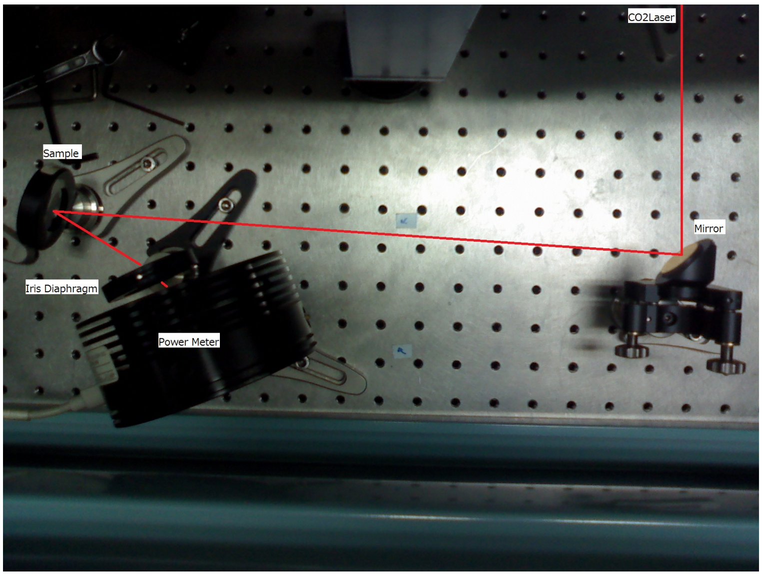

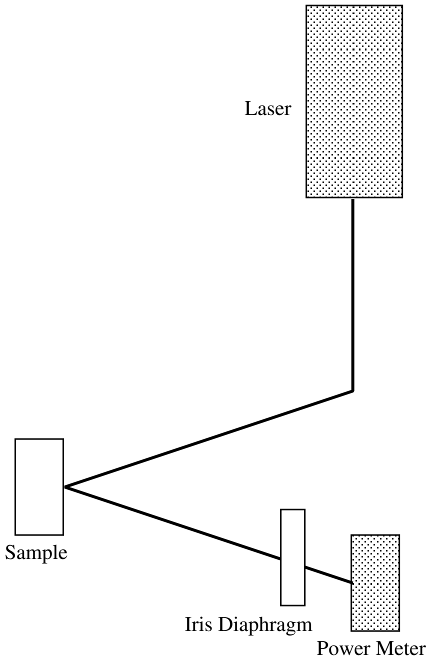

Figure 5.7: Experimental setup for measurements at room temperature for the case that the number of reflections is $\mathcal{N} = 1$

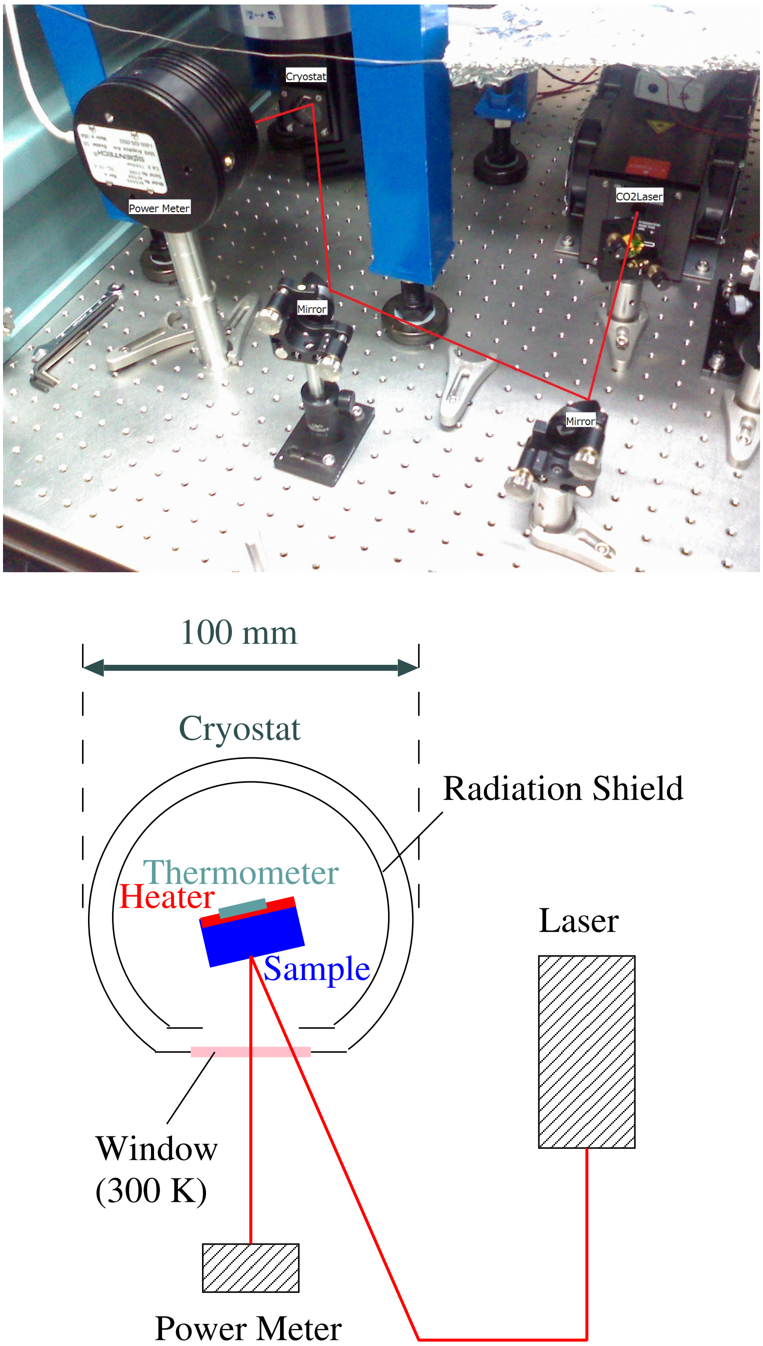

Figure 5.8: Experimental setup for measurements at cryogenic temperature. The cryostat was cooled by a 4 K pulse tube cryocooler with double stages, whose 1st stage is connected to the radiation shield and 2nd stage is connected to the sample.

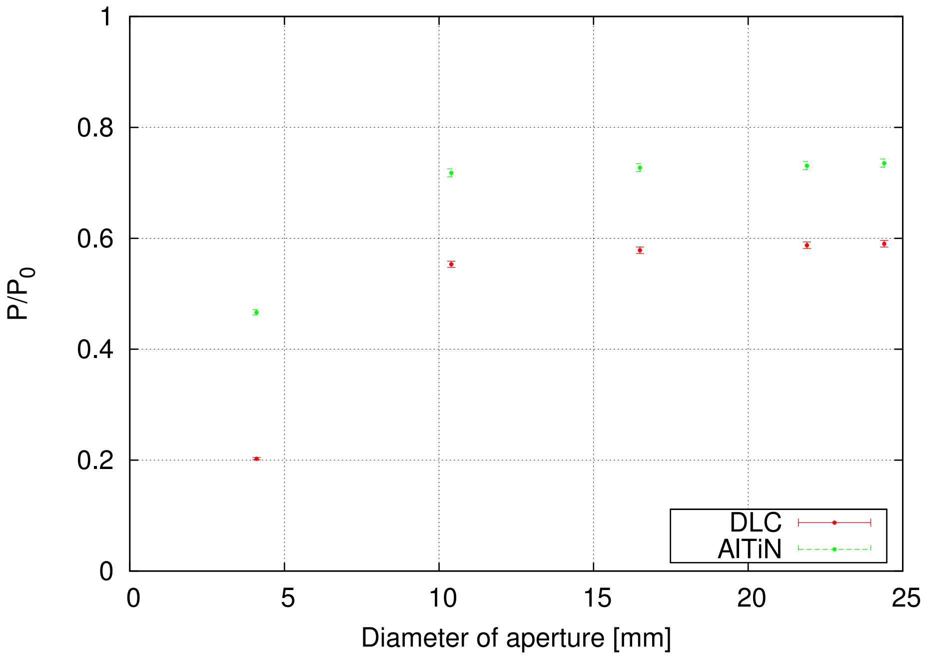

Figure 5.9: Power after reflections divided by the power of the laser before the reflection, $\mathcal{P}/\mathcal{P}_0$, as a function of the diameter of the aperture of the iris diaphragm. The error bars show an error of 1% from the precision of the power meter and the fluctuation of the intensity of the laser.

5.4.2 Measurements at cryogenic temperature

The relationship between the temperature and the absorptivity of each sample is shown in Figures 5.10-5.12. Figures 5.11 and 5.12 show the same result as Figure 5.10, plotted by different scales of the vertical axes. In these figures, plural plots at a certain temperature represent the results of repetitive measurements. The value of the temperature has errors of several K because the result where the value of the thermometer changed by more than 6 K was discarded, as described in subsection 5.3.2.

The change in temperature of the DLC sample as a representative during a measurement is shown in Figure 5.13.

5.5 Error analysis

5.5.1 Measurements at room temperature

The results of measurements at room temperature have errors that come mainly from:

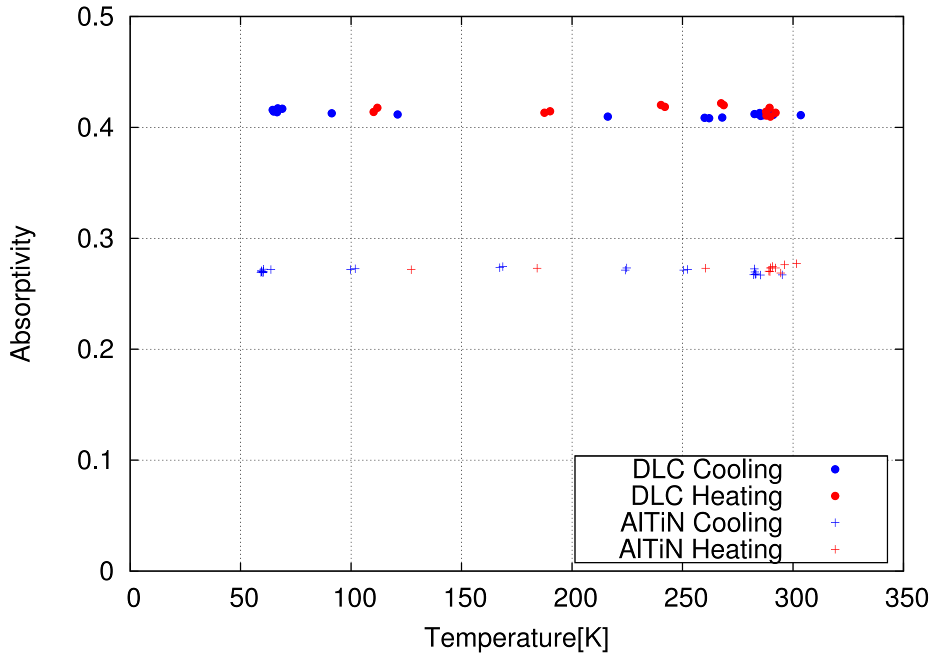

Figure 5.10: Relationship between temperature and absorptivity. Plural plots at one temperature represent the results of repetitive measurements. In the legends, “cooling” represents data taken while cooling the sample and “heating” represents that during heating.

1. the precision of the power meter,
2. the fluctuation of the intensity of the laser,
3. the scattering on the surfaces of the samples.

The precision of the power meter and the fluctuation of the intensity of the laser were 1 % as described in subsection 5.2.1. On the other hand, the accuracy of the power meter was 3 %, which did not have any effect on the values of the reflectivity because $\mathcal{P}$ and $\mathcal{P}_0$ in Eq(4.20) were measured by the same power meter.

To prevent the laser from scattering on the surfaces of the samples as possible, the samples whose surfaces are regarded as mirrors, that is, whose surface roughness are sufficiently small were used. Moreover, Figure 5.9 confirms that more than 99 % of the power of the laser reflected or scattered by the sample is detected because the power becomes constant within 1 % at more than 20 mm in the diameter of the aperture.

To sum up these errors, the error in $\mathcal{P}/\mathcal{P}_0$ of each sample is approximately 1 %. Thus, the error in the absorptivity is approximately 1 %, which is given in Table 5.2.

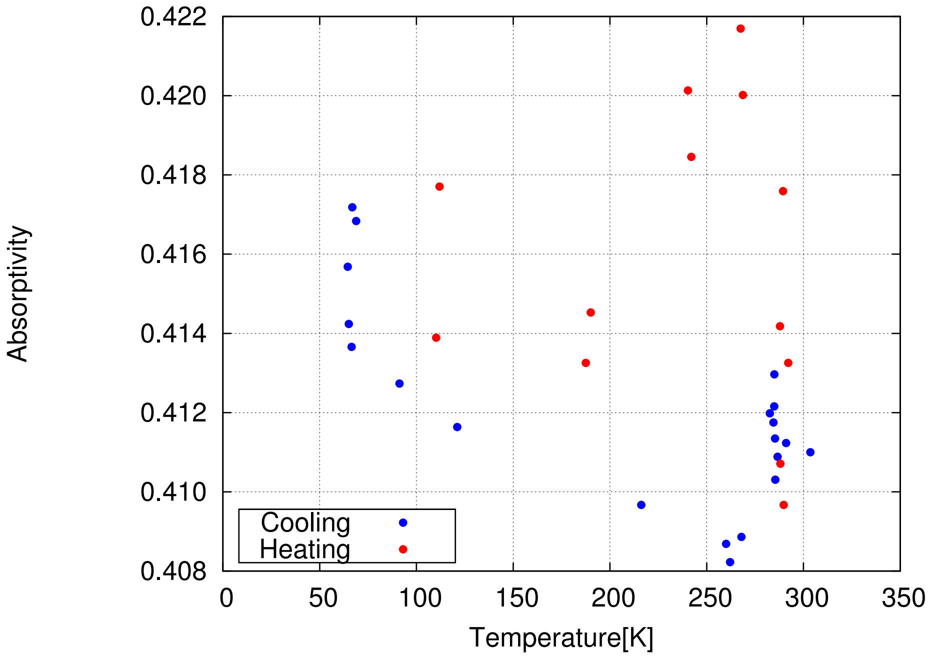

Figure 5.11: Relationship between temperature and absorptivity of the DLC sample; this is the same result as Figure 5.10 but plotted by a different scale of the vertical axis.

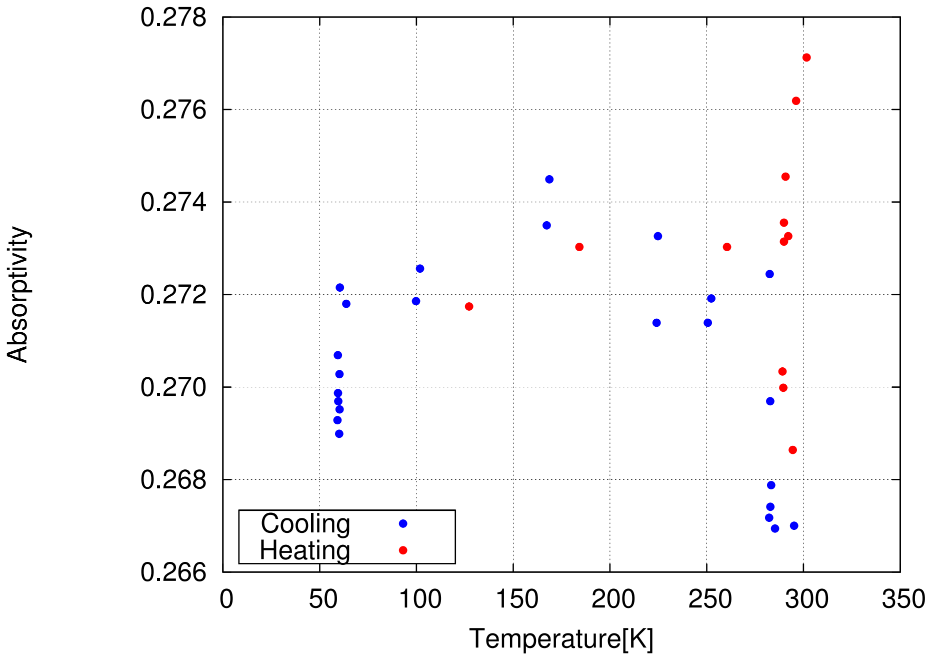

Figure 5.12: Relationship between temperature and absorptivity of the AlTiN sample; this is the same result as Figure 5.10 but plotted by a different scale of the vertical axis.

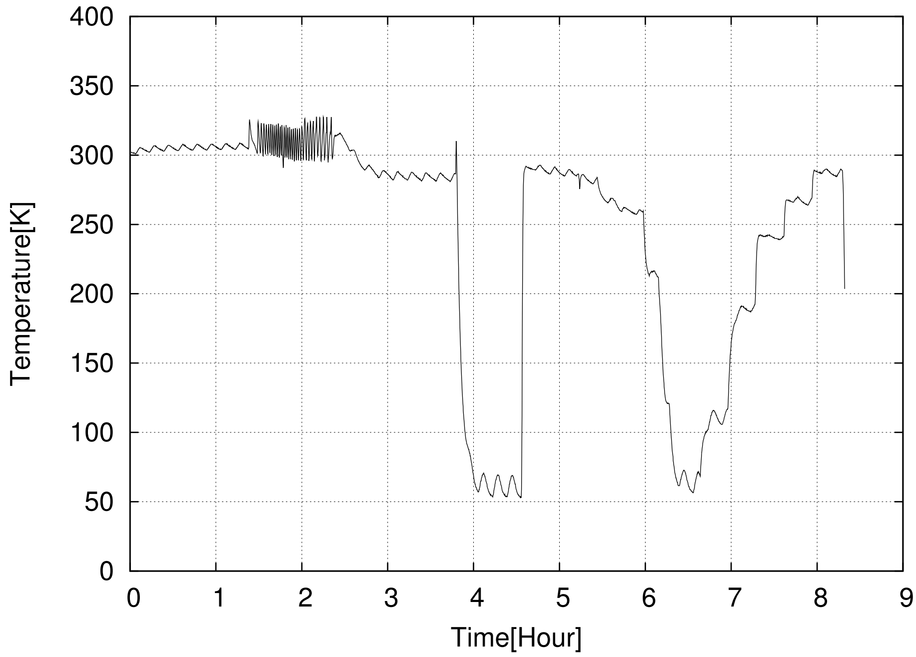

Figure 5.13: Temperature change with time. Waveforms represent that the laser was turned on and off repeatedly every 10 minutes.

5.5.2 Measurements at cryogenic temperature

The results of the measurements at cryogenic temperature have errors come mainly from

1. the precision of the power meter,

2. the fluctuation of the intensity of the laser.

Measuring the relative value, as shown in Eq.(4.22), makes it unnecessary to take into account the scattering on the surface of the sample because one can assume that the angular distribution of the scattering doesn't have any difference between room temperature and the cryogenic temperature. Also, it is unnecessary to take into consideration the absorption or the scattering of the laser by the window of the vacuum chamber BaF_2 because the deformation of the window can be neglected since both $\mathcal{P}(T = 300\text{ K})$ and $\mathcal{P}(T)$ in Eq.(4.22) were measured under a vacuum and one can assume that the window is always at room temperature.

The precision of the power meter and the fluctuation of the intensity of the laser were 0.7% as described in subsection 5.2.2. The accuracy of the power meter doesn't have any effect on the values of the reflectivity.

As a result, the value of the reflectivity has systematic errors of about 1%, which come from $\mathcal{P}(T = 300\ \mathrm{K})$ and R_0, and random errors of about 1%, which come from the precision of the power meter and the fluctuation of the intensity of the laser. Namely, the value of the absorptivity has systematic errors of about 0.01 (absolute error) and random errors of about 0.01 (absolute error). In total, the measured values of absorptivity have an uncertainty of about 0.02.

5.6 Discussion

Taking into account random errors of about 0.01 in the absorptivity, no dependence of the reflectivity was found on temperature in Figures 5.11 and 5.12.

The absorptivity was reproduced at the same temperature within random errors of 0.01 in Figures 5.11 and 5.12.

For the LCGT, the change of the property, including the reflectivity, of these coatings over several years is important, whose examination is future work.

Chapter 6

Thermal radiation (funneling) through a shield pipe for LCGT

This chapter describes one of the applications of the results of reflectivity measurements described in chapters 4 and 5, namely, a calculation about the incident heat through the radiation shields of the LCGT ducts.

To reduce the thermal noise described in subsection 2.3.2, the mirrors will be cooled down to cryogenic temperature (20 K) in the LCGT. Only cryostats that contain the mirrors will be cooled down while the beam ducts and vibration isolation system are to be kept at room temperature in LCGT, because it is difficult to cool all of the huge 3 km interferometer. (The LCGT cryostat is shown in Figure 6.1.) However, the cooling power is limited because only four small cryocoolers for each cryostat will be used to prevent vibration of the cryocoolers from causing noise, and not to cause any danger of using cooling gas underground. Thus, it is necessary to estimate all of the heat loads on the LCGT cryocoolers in order to design the cryostat appropriately.

Among them, the incident power of thermal radiation from an opening of the cryostat through which a laser beam passes was problematic. Although the mirror should be surrounded by a radiation shield, a hole in the shield is necessary for the laser beam. Thus, it is necessary to reduce thermal radiation from the hole of the cryostat. To do this, a radiation shield pipe (80 K) was installed so as to decrease the solid angle to the 300 K region in cooling tests of the Cryogenic Laser Interferometer Observatory (CLIO)[11], which is described in section 2.4. However, thermal radiation still comes into the cryostat due to being reflected by the surface of the duct shield[28]. (A similar phenomenon also occurs through the neck tube of a liquid-helium dewar[29].)

Although it was shown experimentally that introducing two baffles, whose shape is shown in Figure 6.2, in the duct shield could reduce the incident heat sufficiently[30], it was necessary to obtain how much the incident heat can be reduced when more than two baffles are set and which position of the baffles can make it smallest since it is better to have some safety margin in the heat load. In addition, the apertures of the baffles have to be wider in the LCGT current plan than considered in [30] because reflection of the main laser beam or light for monitoring the mirror will pass through the baffles as shown in Figure 6.3 and there is no estimation or measurement of the incident heat in this case. The incident heat in this case was thus calculated by using a ray-trace model. In order to examine the validity of this calculation, the thermal radiation through the small aluminum pipe with baffles was measured.

6.1 Calculation

6.1.1 Method

The incident power of thermal radiation through the duct shield, P_i, is, assuming that duct shield is axial symmetric, that the tracing ray is started from the middle of the duct shield opening of the room temperature side, and that thermal radiation from the opening is isotropic,

$$P_i = P_0 \int R_d^{N_d(\theta)} R_r^{N_r(\theta)} R_c^{N_c(\theta)} \frac{d\Omega}{2\pi}, \tag{6.1}$$

where P_0 is the total emitted power from the opening, Ω is the solid angle from the opening of the room-temperature side to the opening of the cryogenic temperature side, and R_d, R_r, R_c is the reflectivity of the surface of the duct, the room temperature sides of the baffles and the cryogenic temperature sides of the baffles respectively; $N_d(\theta)$, $N_r(\theta)$, $N_c(\theta)$ are the number of reflections of a ray with incident angle θ by, also here, the surfaces of the duct, the room temperature sides of the baffles and the cryogenic temperature sides of the baffles, respectively. The integral is calculated over a semisphere. In this integral, the rays returned to the room-temperature side by the baffles are excluded, and only those incident on the cryogenic temperature side are included. Conversely, the value that includes the former and excludes the latter is the reflected power by the baffles, P_r. In addition, the absorbed power by the duct shield, P_a, is $P_a = P_0 - P_i - P_r$. To calculate these values, the range of the incident angle, $0 < \theta < \pi/2$, was divided by $M = 10000$; also θ was changed by an infinitesimal angle, $\Delta\theta = (\pi/2)/M$, the ray was traced, and the number of reflections for angle θ was counted. This gives:

$$\begin{aligned} P_i &= P_0 \int_0^{\pi/2} R_d^{N_d(\theta)} R_r^{N_r(\theta)} R_c^{N_c(\theta)} \sin\theta d\theta & (6.2) \\ &\simeq P_0 \sum_{i=0}^{M-1} R_d^{N_d(i\Delta\theta)} R_r^{N_r(i\Delta\theta)} R_c^{N_c(i\Delta\theta)} \sin(i\Delta\theta)\Delta\theta, & (6.3) \end{aligned}$$

where the sum excludes rays returned to the room-temperature side, and includes only those incident on the cryogenic temperature side. On the other hand, the sum which includes only

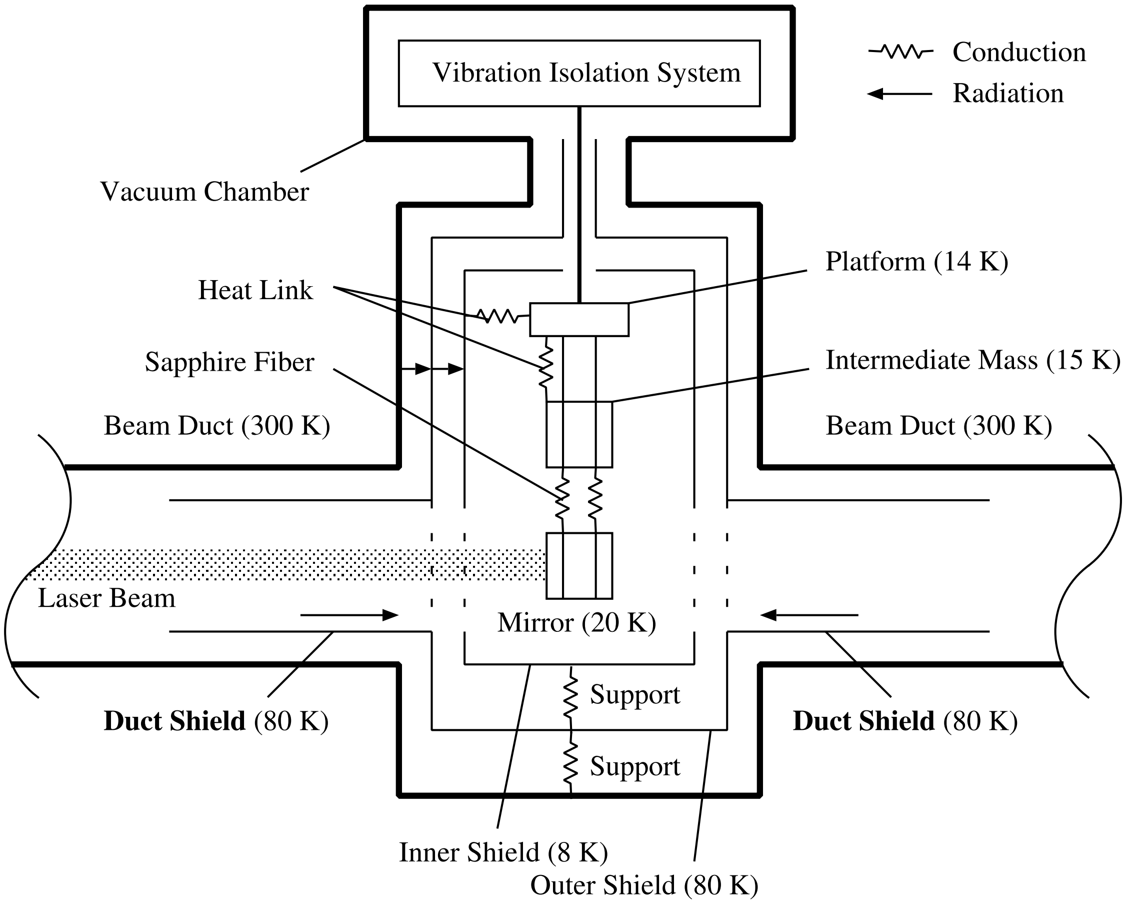

Figure 6.1: Schematic diagram of the cryotstat of LCGT. The inside of the vacuum chamber is kept at a high vacuum to prevent noise caused by fluctuation of the refractive index along the path of the laser. The outer shield is connected to the 1st stages of four cryocoolers, and the inner shield is connected to the 2nd stages of the four cryocoolers. Heat absorbed by the mirror is conducted to the intermediate mass by the sapphire fibers, to the platform and to the inner shield by aluminum heat links. Thermal radiation comes from the wall of the cryostat to the outer shield and from the outer shield to the inner shield, and through the duct shields to the inner shield.

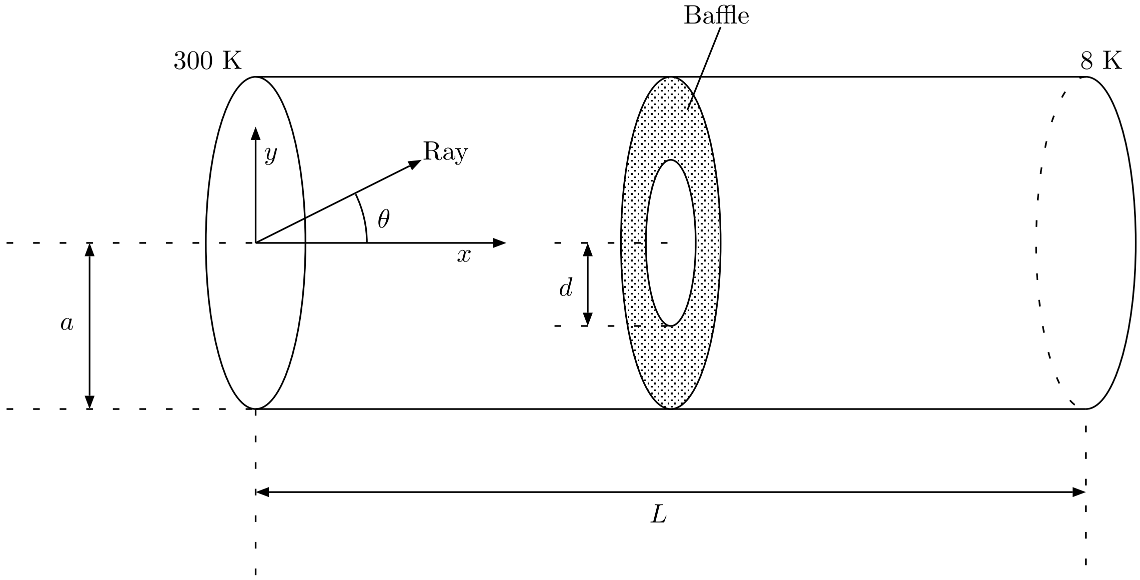

Figure 6.2: Baffle is introduced in the duct shield

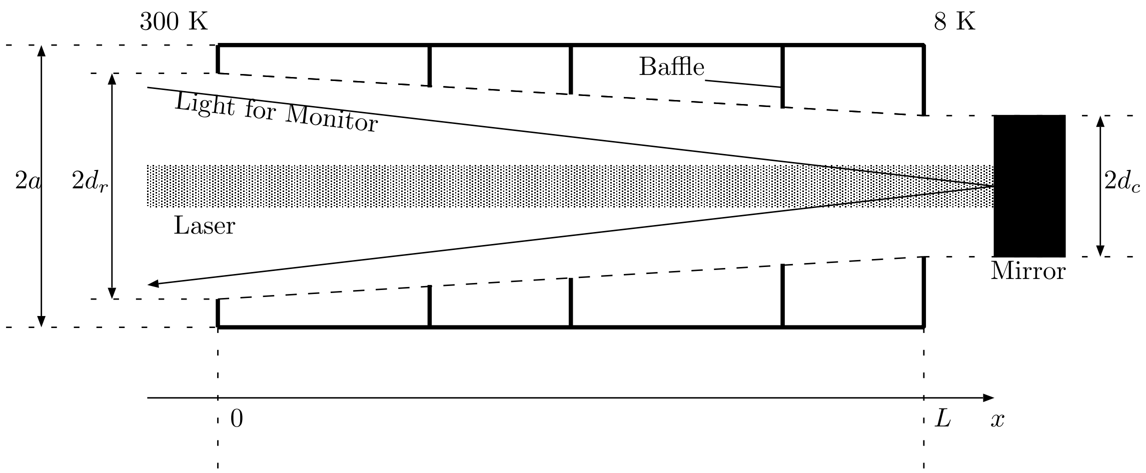

Figure 6.3: Duct shield of the LCGT cryostat. The apertures of the baffles depend on the position.

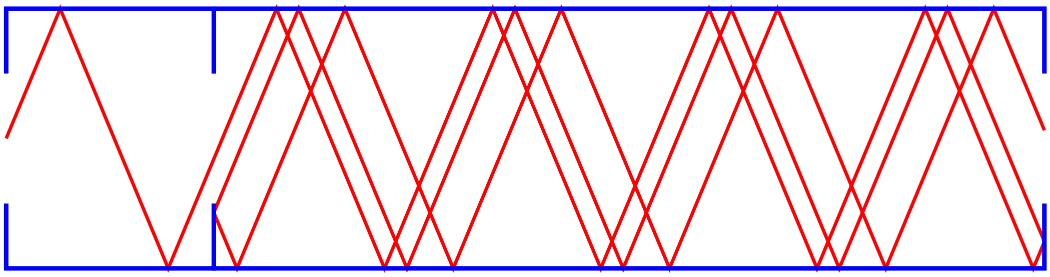

Figure 6.4: Example of the ray path in the case where three baffles are inserted

the rays returned to the room-temperature side is P_r. Figure 6.4 shows an example of the ray path calculated using this model.

The diameter of the duct shield is represented as $2a$, the length as L, and the diameter of the baffle aperture as $2d$, as shown in Figure 6.2.

6.1.2 Result

	P_i [W]	P_r [W]	P_a [W]
No baffle	$6.2^{+2.7}_{-1.6}$	0	23^{-3}_{+2}
Five baffles	$0.16^{+0.12}_{-0.06}$	$2.6^{+1.5}_{-0.8}$	20^{-2}_{+1}
Five baffles with DLC	$0.088^{+0.060}_{-0.033}(*)$	$1.5^{+0.9}_{-0.5}$	21^{-1}_{+1}
Five baffles with AlTiN	$0.11^{+0.08}_{-0.04}$	$1.9^{+1.1}_{-0.6}$	21^{-1}_{+1}

Table 6.1: P_i, P_r and P_a in the LCGT current plan. The errors in the superscript are for $R_d = R_r = R_c = 0.96$ and those in the subscript are for $R_d = R_r = R_c = 0.92$ in "No baffle" and "Five baffles." In "Five baffles with DLC", the errors in the superscript are for $R_d = R_c = 0.96,\ R_r = 0.61$ and those in the subscript are for $R_d = R_c = 0.92,\ R_r = 0.57$. In "Five baffles with AlTiN", the errors in the superscript are for $R_d = R_c = 0.96,\ R_r = 0.75$ and those in the subscript are for $R_d = R_c = 0.92,\ R_r = 0.71$. Five baffles are set at $x = 0, 10, 14, 16, 17$ m.

The current plan of the LCGT has the following parameters:

$$2a = 0.9 \text{ m}, \quad L = 17 \text{ m}, \quad R_d = R_r = R_c = 0.94 \pm 0.02. \tag{6.4}$$

The reflectivity is the measured value in chapter 4 for aluminum A1070, which will be used for the LCGT duct shields, at 80 K and a wavelength 10 μm, where the black-body radiation at 300 K has the largest intensity. In this case, the apertures of the baffles have to be wider because reflection of the main laser beam or light for monitoring the mirror will pass through the baffles, as shown in Figure 6.3. In the current plan, the apertures of the baffles depend on the position x as follows:

$$d(x) = d_r + \frac{x}{L}(d_c - d_r). \tag{6.5}$$

Namely, the aperture of the baffle at the room temperature side is $2d_r = 0.8$ m in diameter, that at the cryogenic temperature side is $2d_c = 0.25$ m, and those between them change linearly as shown in Figure 6.3.

With no baffle

P_i, P_r, and P_a were calculated with no baffle, as shown in Table 6.1 for not only $R_d = 0.94$ but also $R_d = 0.92, 0.96$ to show the dependence on the error of R_d. Here,

$$P_0 = \epsilon\sigma T^4 A = 29.2 \text{ W}, \tag{6.6}$$

was used, where $\epsilon = 0.1$ is the emissivity of the beam duct (SUS, room temperature) and $A = \pi a^2$ is the area of the duct shield opening.

With baffles

Two baffles were fixed at $x = 0$ and $x = L = 17$ m. Then, all 560 (the number of combinations of 3 taken from 16, ${}_{16}C_3$) cases in which three baffles are set at any place of $x = 1, 2, 3, \cdots, 16$ m were calculated using $R_d = R_r = R_c = 0.94$. The minimum value of P_i was obtained in the case where the baffles are set at

$$x = 0, 10, 14, 16, 17 \text{ m}. \tag{6.7}$$

The values of P_i, P_r, and P_a for $R = 0.94$ besides $R = 0.92, 0.96$ are listed in Table 6.1. Here,

$$P_0 = \epsilon\sigma T^4 A = 23.1 \text{ W}, \tag{6.8}$$

was used, where $\epsilon = 0.1$ is emissivity of the beam duct (SUS, room temperature) and $A = \pi d_r^2$ is the area of the aperture of the baffle.

In addition, the case where the room temperature sides of the baffles are coated with a high absorptivity coating such as Diamond Like Carbon (DLC) and AlTiN in order to absorb the thermal radiation and decrease the incident heat was calculated. The reflectivity

$$R_d = R_c = 0.94 \pm 0.02, R_r = 0.59 \pm 0.02 \tag{6.9}$$

for DLC and

$$R_d = R_c = 0.94 \pm 0.02, R_r = 0.73 \pm 0.02 \tag{6.10}$$

for AlTiN were used. These values are measured at 80 K and a wavelength of 10 μm, whose measurement is described in chapter 5. The result of the calculation is given in Table 6.1. Also, in this case the minimum value of P_i was obtained when the baffles are set at eq.(6.7).

6.2 Experiment

6.2.1 Method

Figure 6.5: Cryostat used for the experiment

Figure 6.6: Cryostat in a nitrogen dewar

In the cryostat shown in Figure 6.5, an aluminum A1070 pipe with a chemically polished (CP) surface (the outer diameter is 30 mm and the inner diameter is 24 mm) and a bolometer were introduced as shown in Figure 6.8. To make the bolometer, an aluminum plate (20 mm in diameter, 1 mm in thickness) with paper (emissivity $\sim$ 0.9) on its surface was fixed to three G10 bars (5 mm in diameter, 20 mm in length, with screws), as shown in Figure 6.7. Moreover, two aluminum heat links (0.5 mm in diameter, 20mm in length) were connected. The bottom of the bolometer contacted aluminum tape at the bottom of the pipe. Thermometers (DT-670-CU made by LakeShore, calibrated) were attached on the aluminum plate (SI2) and the

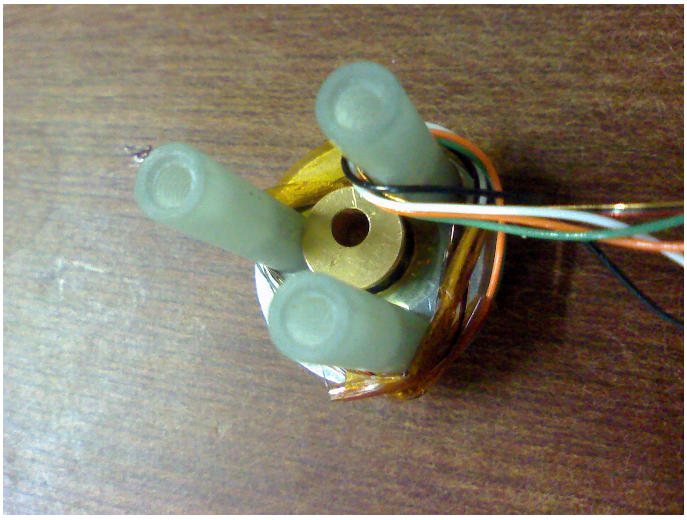

Figure 6.7: Bolometer

aluminum tape (SI4), a heater (H2) was attached to the aluminum plate. The difference in the temperature between these two thermometer ΔT indicates the incident heat. As a monitor, a thermometer SI3 was attached to the pipe.

When the experiment was started, the inside of the cryostat was kept in a vacuum ($\sim 10^{-3}$ Pa) to prevent water molecules from adhering to the pipe. Next, the cryostat was soaked into liquid nitrogen (nitrogen dewar is shown in Figure 6.6) and helium gas was introduced into the cryostat. The pipe was cooled down mainly by convection of the helium gas between the wall of the cryostat and the pipe. After the helium gas was pumped out, the pressure was $\sim 10^{-4}$ Pa.

Calibration

To examine the relationship between ΔT and the incident heat, a calibration was conducted. To prevent radiation from coming into the bolometer, the hole on the room temperature side of the pipe was closed by another aluminum tape. When the pipe and the bottom of the bolometer was cooled down to approximately 80 K, the dependence of the difference in the temperature ΔT on the heat coming from heater H2 was measured.

Measurement

The radiation plate with paper on its surface was set above the aluminum pipe. A heater H1 and a thermometer SI1 were attached to it. After the pipe and the bottom of the bolometer were

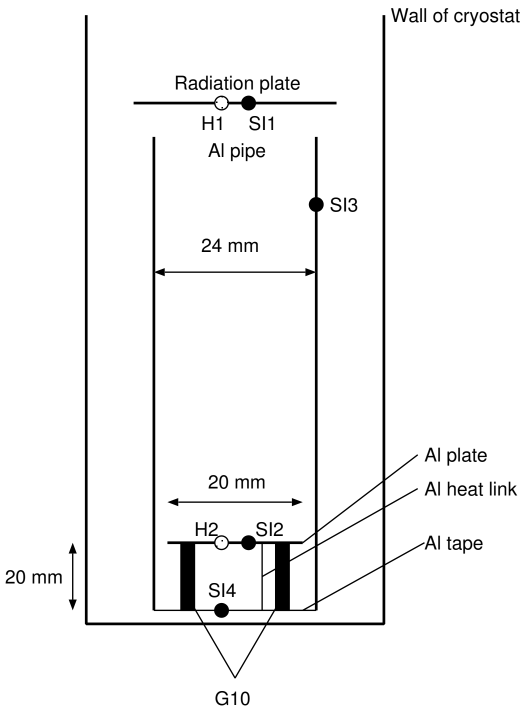

Figure 6.8: Schematic diagram of the experimental setup

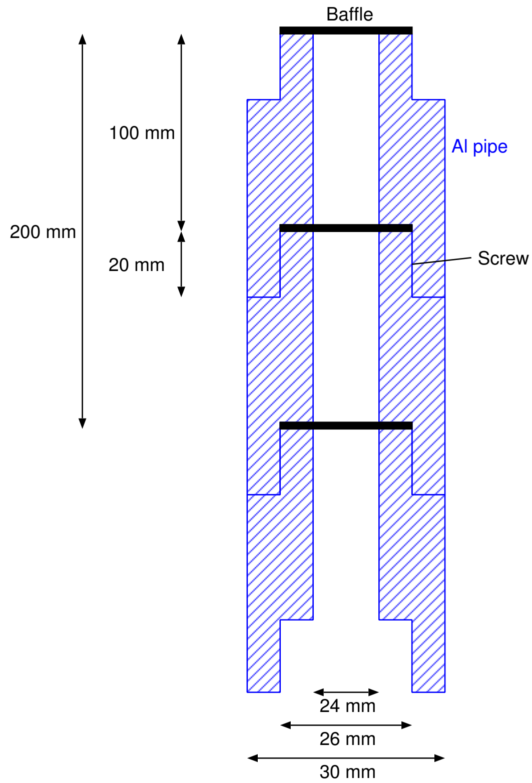

Figure 6.9: Baffles fixed by the pipe

cooled down to approximately 80 K, the radiation plate was kept 300 K by heater H1. Then, ΔT was measured and transferred to the incident heat. In order to confirm that the temperature difference ΔT was caused by radiation from the radiation plate, the same measurement was performed when the radiation plate was kept at a different temperature (e.g. 250 K).

Three baffles, whose apertures were 20, 16, 12 mm in diameter, were introduced at distances of 0, 100, 200 mm from the room temperature side, respectively. The baffles were fixed by the pipe with screws, as shown in Figure 6.9.

6.2.2 Result

Calibration

The temperature change over time of each thermometer is shown in Figures 6.13 and 6.14. The relationship between ΔT and the incident heat H_2 are given in Table 6.2 and Figure 6.12.

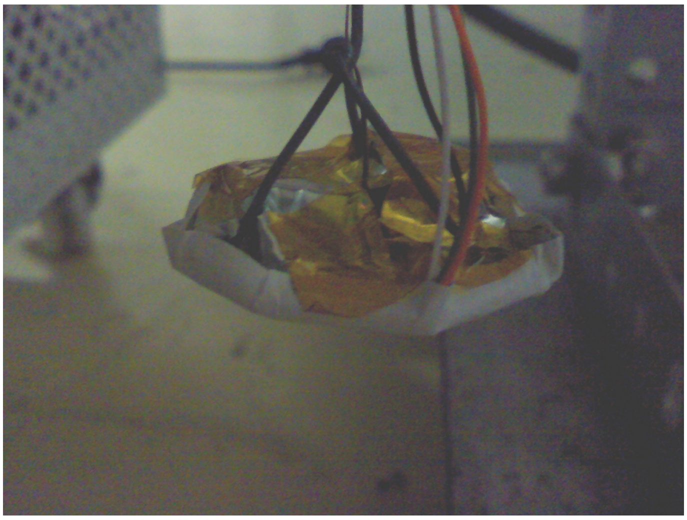

Figure 6.10: Radiation plate

Figure 6.11: Pipe and baffles

The data is fitted by a line:

$$H_2 = a\Delta T + b, \tag{6.11}$$
$$a = 0.00377 \text{ W/K}, \tag{6.12}$$
$$b = -0.00429 \text{ W}. \tag{6.13}$$

The maximum relative difference of H_2 between eq.(6.11) and the data is approximately 30 % (the case ($*$) of Table 6.2), which can be regarded as the uncertainty of this measurement.

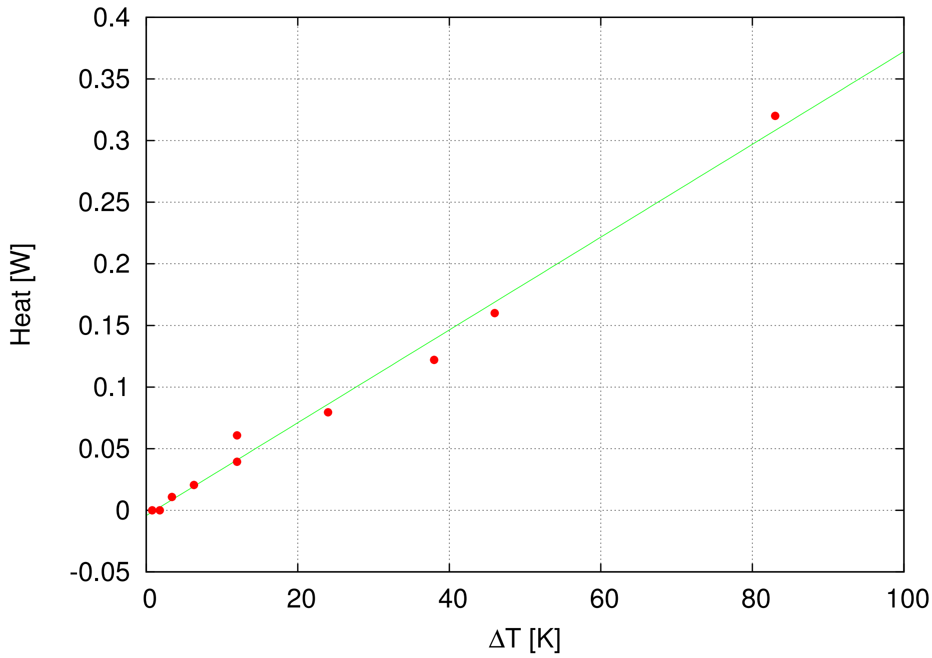

Figure 6.12: Result of the calibration: relationship between $\Delta T = T_{\rm SI2} - T_{\rm SI4}$ and the incident heat

Measurement

The temperature change over time of each thermometer is shown in Figures 6.15 and 6.16. When the radiation plate (SI1) is below 100 K, that is, the incident heat can be neglected,

$$(\Delta T)_0 = -0.47\text{K}. \tag{6.14}$$

When the radiation plate (SI1) is 304$\pm$2 K,

$$\Delta T = 0.30\text{K} \tag{6.15}$$

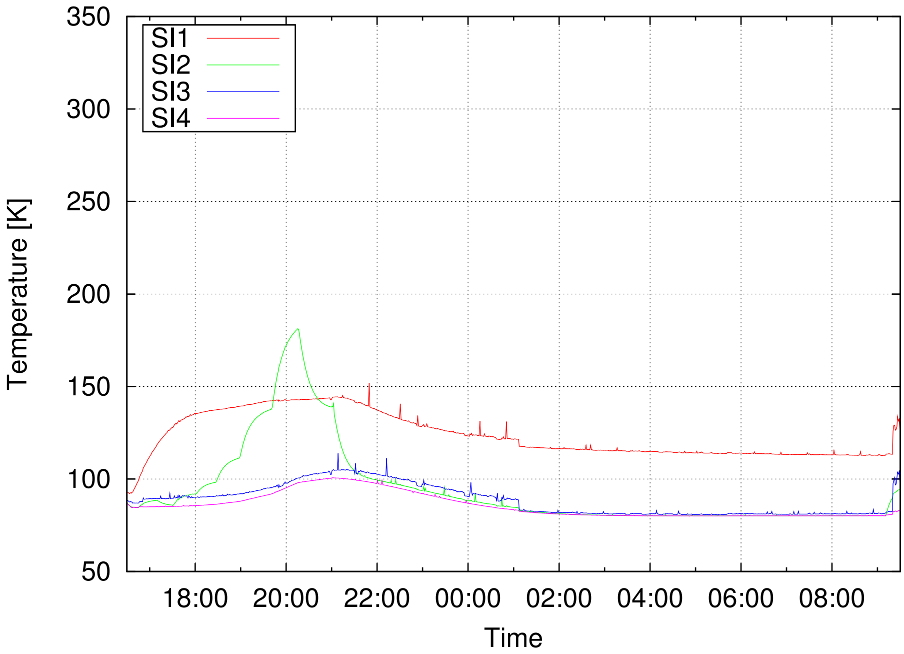

Figure 6.13: Temperature change over time (calibration)

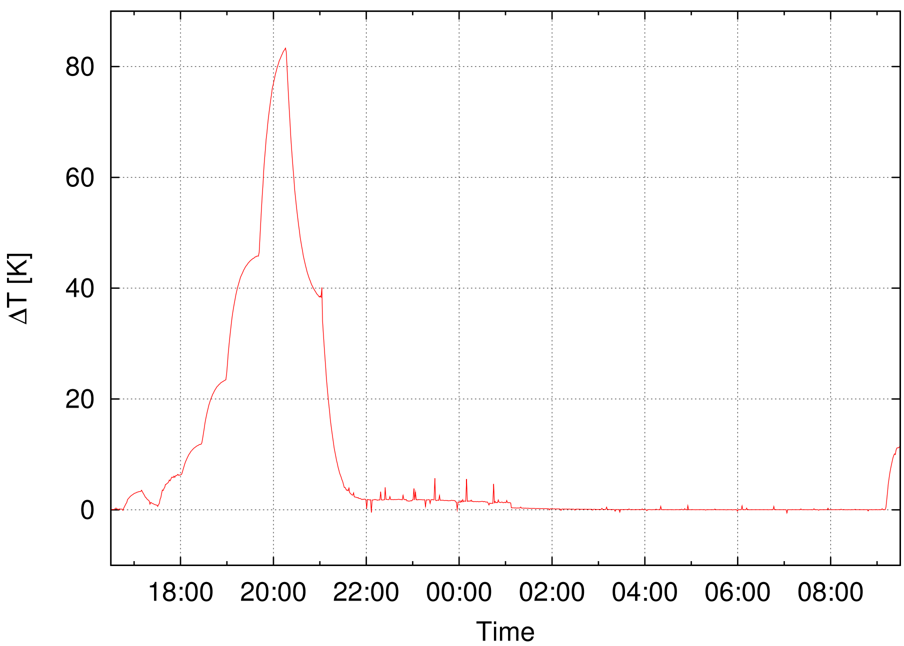

Figure 6.14: Temperature change over time (calibration, $\Delta T = T_{\mathrm{SI2}} - T_{\mathrm{SI4}}$)

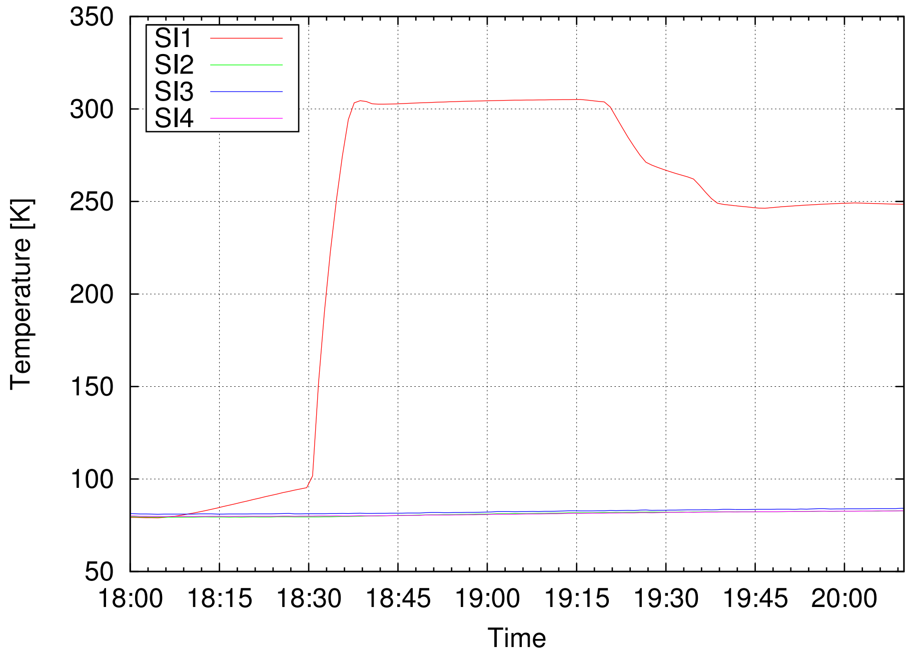

Figure 6.15: Temperature change over time (measurement with baffles)

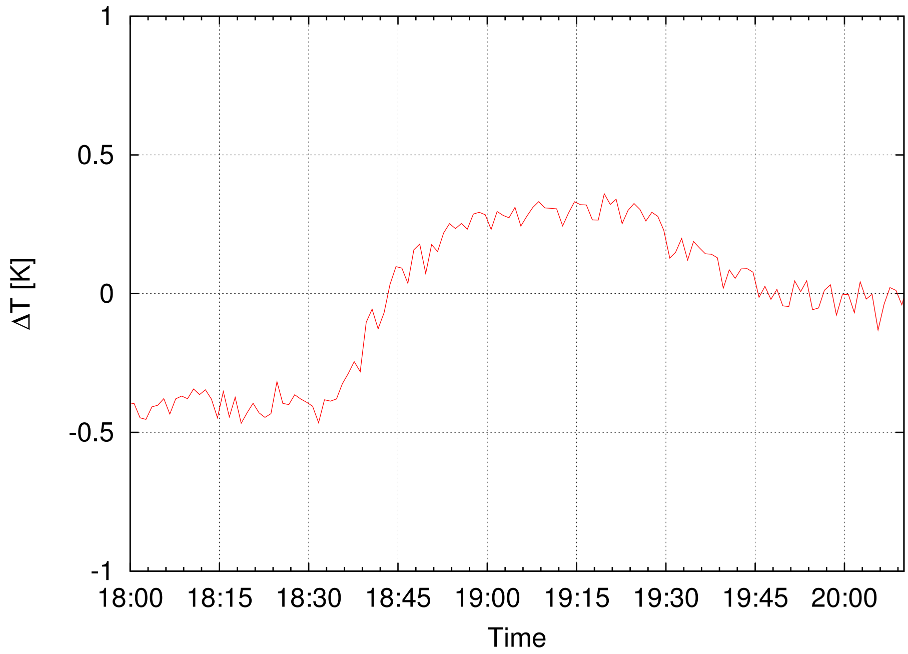

Figure 6.16: Temperature change over time (measurement with baffles, $\Delta T = T_{\mathrm{SI2}} - T_{\mathrm{SI4}}$)

Time	ΔT [K]	Heat (H_2) [W]
16:45 - 17:08	3.4	0.0108
17:08 - 17:30	0.8	0
17:30 - 18:00	6.3	0.0205
18:00 - 18:26	12	0.0394
18:26 - 18:58	24	0.0795
18:58 - 19:40	46	0.160
19:40 - 20:15	83	0.320
20:15 - 21:00	38	0.122
21:00 - 21:30	1.8	0
09:11 - 09:34 ($*$)	12	0.0608

Table 6.2: Result of the calibration

was obtained. According to eq.(6.11) with compensation of eq.(6.14), the absorbed heat by the aluminum plate was

$$H_{304} = a[\Delta T - (\Delta T)_0] = 0.0029 \text{ W}. \tag{6.16}$$

When the radiation plate (SI1) is 248±1 K,

$$\Delta T = -0.01\text{K}, \quad H_{248} = a[\Delta T - (\Delta T)_0] = 0.0017 \text{ W}, \tag{6.17}$$

namely,

$$\frac{H_{248}}{H_{304}} = 0.60. \tag{6.18}$$

This value should be

$$\left(\frac{248}{304}\right)^4 = 0.44, \tag{6.19}$$

which is different from eq.(6.18) by approximately 30 %. This can be regarded as the uncertainty of this measurement.

The effective surface area of the bolometer (the paper of 20 mm in diameter is hidden by three screws of 5 mm in diameter) is

$$S_b = \frac{\pi}{4}(20\text{mm})^2 - \frac{\pi}{4}(5\text{mm})^2 \times 3 = 2.55 \times 10^{-4} \text{ m}^2 \tag{6.20}$$

while the cross-sectional area of the inside of the pipe is

$$S_p = \frac{\pi}{4}(24\text{mm})^2 = 4.52 \times 10^{-4} \text{ m}^2. \tag{6.21}$$

Using these values, the incident radiation P_i is

$$P_i = \frac{S_p}{S_b}\frac{H_{304}}{\epsilon_{\text{paper}}} = 0.0057 \text{ W}, \tag{6.22}$$

where $\epsilon_{\text{paper}} \sim 0.9$ is the emissivity of the paper. Heat radiated by the radiation plate is

$$P_0 = \epsilon_{\text{paper}} \sigma T_{\text{SI1}}^4 S_{20} = 0.137 \text{ W}, \tag{6.23}$$

where $S_{20} = 3.14 \times 10^{-4}$ m^2 is the area of the aperture of the baffle at the top. Thus,

$$\frac{P}{P_0} = 0.042. \tag{6.24}$$

On the other hand, the calculated value using the ray-trace model is (the reflectivity of the surface of the pipe R is 0.94)

$$\frac{P}{P_0} = 0.093. \tag{6.25}$$

This value is several times larger than the measurement eq.(6.24). Conversely, if $0.83 < R < 0.90$, the ray-trace model yields a consistent value with eq.(6.24) within an uncertainty of 30 %.

Heat loads on 4 cryocoolers	[W]
Radiation through duct shields	0.3
11 view ports	0.4
Radiation from outer shield	2.2
Conduction from supports	2.4
Conduction from mirror absorbing laser beam	0.9
Total	6.2

Table 6.3: Summary of the heat loads on the 2nd stages of the cryocoolers in LCGT. The total cooling power of the 2nd stages of the four cryocoolers is approximately 8 W at 6 K (2 W per one cryocooler). "Radiation through duct shields" is from the superscript of the case $(*)$ in Table 6.1, 0.15 W, times 2, and the values of the other heat sources are shown in [31].

6.2.3 Discussion

There is a discrepancy between the calculation and the measurement. It is necessary to find the factor that causes this discrepancy in the future.

However, both values are consistent within several times. Fortunately, since the calculated value is larger than the measured value, the calculated result in the LCGT case can be regarded as the value on the safety side, which helps to design the LCGT cryostat.

In case $(*)$ in Table 6.1, the incident heat through the duct shield can be reduced to 0.15 W at most. Then, the sum of the incident power through the two duct shields is 0.30 W. This is smaller by more than one order of magnitude than the sum of the heat loads on the 2nd stages of the cryocoolers, 6.2 W, as given in Table 6.3. It was found that thermal radiation through the duct shields could be reduced to the extent that it didn't prevent cooling.

Chapter 7

Conclusion

The reflectivity was measured for samples that are candidates for the radiation shields of LCGT using a CO_2 laser with wavelength $\lambda = 10.59$ μm, where black body radiation of 300 K has the largest intensity. As an application of the result of the reflectivity measurements, the incident heat through the duct shields was calculated in the case of the current LCGT plan. It was found that:

- A duct shield with baffles can sufficiently reduce the incident heat in LCGT.
- Baffles coated with a high absorptivity coating are useful to reduce the incident heat.
- The calculation and measurement of thermal radiation through a small pipe are consistent within several times.

In the future, there is a plan to verify the result of this calculation in the LCGT cryostat.

Appendix A

Sample program

A.1 Flowchart to calculate the incident heat through the duct shield

A calculation of the incident heat through the duct shield was conducted using c-code. The flowchart of the program is shown in Figure A.1 and the sample program in the case $(*)$ in Table 6.1 is given in the next section.

On the plane that includes the center axis of the duct shield, the equation of the ray is expressed as $y = Ax + B$. The initial point of the ray is (x_0, y_0), which satisfies $y_0 = Ax_0 + B$. The direction of the ray is $dr = \pm 1$ when the ray is oriented to the $\pm x$ direction, respectively. Then, the program calculates the point (x_1, y_1) which the ray reaches next. If the point is on the surface of the duct or on the baffles, it calculates the equation and the direction of the ray after reflection. Then, the initial point of the ray is set at (x_1, y_1) and the same calculation is repeated. If the point is on the holes, it stops counting the number of reflections N and adds R^N to the integral.

If the number of reflections is too large ($N \sim 10000$) to reach the holes, counting N is finished and R^N is neglected.

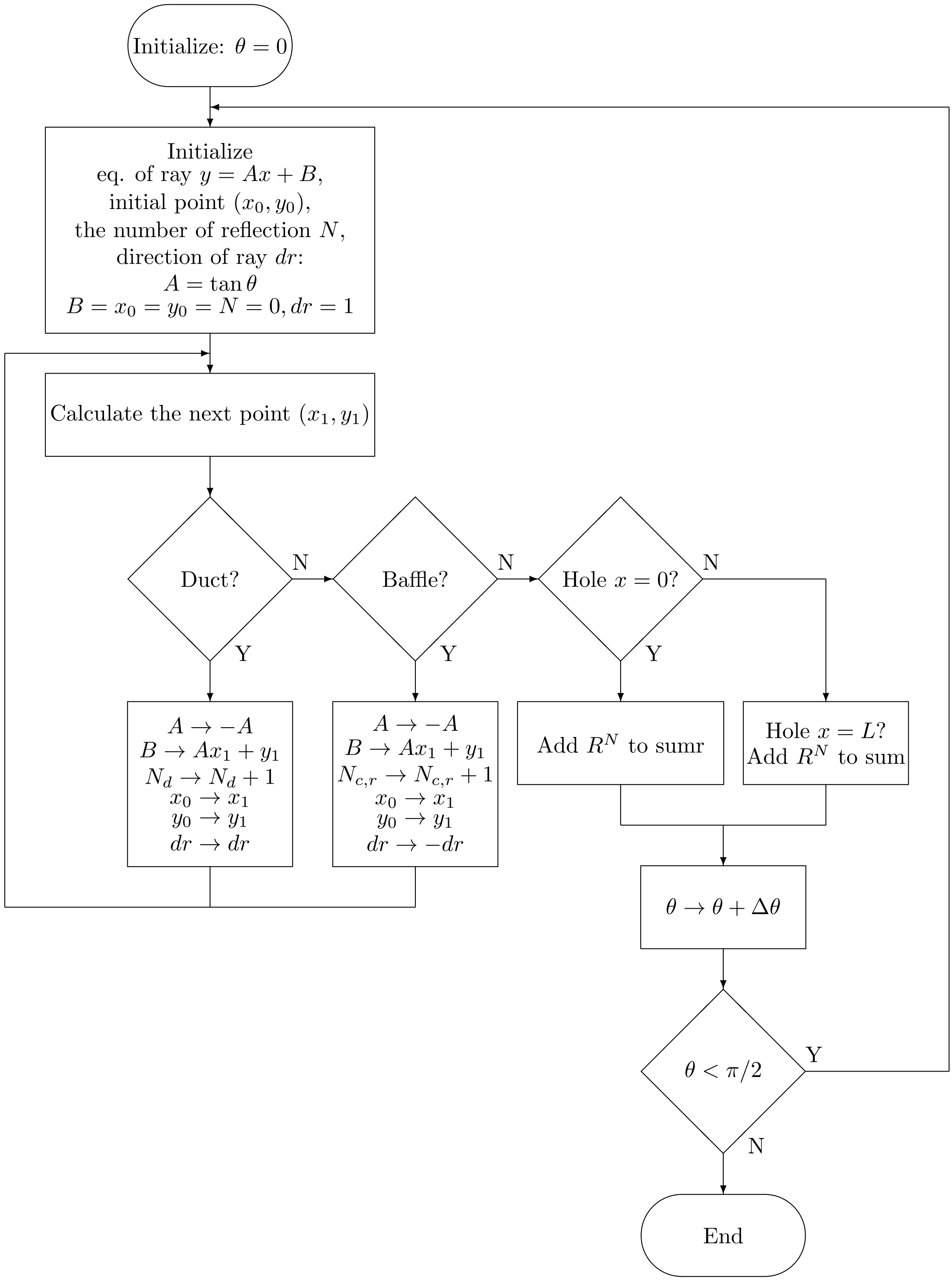

Figure A.1: Flowchart of the program

A.2 A sample program to calculate the incident heat through the duct shield

The program used in the case (∗) in Table 6.1 is as follows:

```
/*
An example of programs (c-code) to calculate the incident heat through the duct shield.
This program shows the results
0.003826 0.065741.
The first one is Pi/P0 and the second one is Pr/P0.
*/

#include<stdio.h>
#include<math.h>

double cx(double x,double L){ //The height of the baffle at the position x
  double cc,cr;
  cc=0.325; //The height of the baffle at the cryogenic temperature side (x = L)
  cr=0.05; //The height of the baffle at the room temperature side (x = 0)

  return cr+(cc-cr)/L*x;
}



int main()
{

  int Nd,Nr,Nc,dr,j,jnear,nb;
  double a,L,A,B,x0,y0,Rd,Rr,Rc,near,dt,t,sum,sumr;
  double x[10];

  a=0.45;
  L=17;

  Rd=0.94; //Reflectivity of the duct
  Rr=0.59; //Reflectivity of the room temperature sides of the baffles
  Rc=Rd; //Reflectivity of the cryogenic temperature sides of the baffles
```

```
dt=M_PI/2.0/10000; //Δθ

sum=0.0; //P_i/P_0
sumr=0.0; //P_r/P_0

for(t=0;t<M_PI/2;t=t+dt){ //t is substituted for θ
  A=tan(t);
  B=0.0;
  x0=0.0;
  y0=0.0;
  Nd=0; //The number of the reflection at the duct
 Nr=0; //The number of the reflection at the room temperature sides of the baffles
  Nc=0;
  //The number of the reflection at the cryogenic temperature sides of the baffles
  dr=1;
  nb=8;
  while(Nd+Nr+Nc<10000){

    x[0]=(a-B)/A; //The x coordinate of the point on the ray at y=a
    if(x[0]<0 ||L<x[0]){x[0]=L*2.0*dr;}
    //If 0<x<L doesn't hold, y=a is not the reflection point.
    x[1]=(-a-B)/A;
    if(x[1]<0 ||L<x[1]){x[1]=L*2.0*dr;}
    x[2]=0; //The hole at the room temperature side
    if(B<-a+cx(0,L) ||a-cx(0,L)<B){x[2]=L*2.0*dr;}
    x[3]=L; //The hole at the cryogenic temperature side
    if(A*x[3]+B<-a+cx(L,L) ||a-cx(L,L)<A*x[3]+B){x[3]=L*2.0*dr;}

    //The baffles
    x[4]=0.0;
    if(A*x[4]+B<-a ||(-a+cx(x[4],L)<A*x[4]+B && A*x[4]+B<a-cx(x[4],L))
    ||a<A*x[4]+B){x[4]=L*2.0*dr;}
    x[5]=L;
    if(A*x[5]+B<-a ||(-a+cx(x[5],L)<A*x[5]+B && A*x[5]+B<a-cx(x[5],L))
    ||a<A*x[5]+B){x[5]=L*2.0*dr;}
    x[6]=10.0;
    if(A*x[6]+B<-a ||(-a+cx(x[6],L)<A*x[6]+B && A*x[6]+B<a-cx(x[6],L))
    ||a<A*x[6]+B){x[6]=L*2.0*dr;}
    x[7]=14.0;
```

```
if(A*x[7]+B<-a ||(-a+cx(x[7],L)<A*x[7]+B && A*x[7]+B<a-cx(x[7],L))
||a<A*x[7]+B){x[7]=L*2.0*dr;}
x[8]=16.0;
if(A*x[8]+B<-a ||(-a+cx(x[8],L)<A*x[8]+B && A*x[8]+B<a-cx(x[8],L))
||a<A*x[8]+B){x[8]=L*2.0*dr;}


//Calculate the reflection point
near=x[0];jnear=0;
for(j=0;j<=nb;j=j+1){
  if(fabs(x0-x[j])>0.0001 && (x[j]-x0)*dr>0.0001){near=x[j];jnear=j;break;}

}
for(j=0;j<=nb;j=j+1){
  if((near-x[j])*dr>0.0001 && (x[j]-x0)*dr>0.0001){jnear=j;near=x[j];}
}


if(jnear==0 ||jnear==1){ //The surface of the duct
  B=A*x[jnear]+a*2*(0.5-jnear);
  A=-A;
  Nd=Nd+1;
  x0=x[jnear];
  y0=a*2*(0.5-jnear);
}
if(jnear==2){ //The hole at the room temperature side
  x0=x[jnear];
  y0=A*x[jnear]+B;
  break;
}
if(jnear==3){ //The hole at the cryogenic temperature side
  x0=x[jnear];
  y0=A*x[jnear]+B;
  break;
}
if(jnear>=4){ //The baffles
  x0=x[jnear];
  y0=A*x[jnear]+B;
  B=A*x0+y0;
```

```
        A=-A;
        if(dr==1){Nr=Nr+1;}else{Nc=Nc+1;}
        dr=-dr;
      }


    }// end while

    if(jnear==3){
      sum=sum+pow(Rd,Nd)*pow(Rr,Nr)*pow(Rc,Nc)*sin(t)*dt;
    }else{
      sumr=sumr+pow(Rd,Nd)*pow(Rr,Nr)*pow(Rc,Nc)*sin(t)*dt;
    }
  }// end for

  printf("%lf %lf\n",sum,sumr);

  return 0;
}
```

Acknowledgement

First, I would like to thank my supervisor Prof. Kuroda. He kindly welcomed me to his laboratory, taught me about LCGT, (To my shame, I knew LCGT for the first time at that time.) and gave me the theme of reflectivity measurement.

Next, I would like to express my gratitude to Prof. Suzuki. He not only taught how to conduct cryogenic experiments but also introduced me to the research field concerning the cryogenic system of LCGT. This field is very attractive because the cryogenic system is a key feature of LCGT, which is the first GW detector in the world that has sufficient sensitivity to detect GWs more than once per year.

Dr. Takahashi prepared the experimental apparatus, including the power meter, the iris diaphragm and the sample to be measured and taught me how to use this equipment. He finally suggested that I should submit the result, which allowed me to publish my paper in TEION KOGAKU[14].

Dr. Musha of University of Electro-Communications, Prof. Saito, Dr. Miyoki, Prof. Mio, Dr. Moriwaki, and Dr. Ohmae prepared, or let me use, the experimental apparatus and gave useful advice for proceeding with this experiment. Especially, Dr. Ohmae proposed that I should use a cryostat in the Mio laboratory, which takes a few hours to cool down, in place of the one in ICRR, which takes about one week to cool down. Without him, I could not have completed this experiment for as early as 2 years.

Dr. Kimura taught about cryogenic engineering necessary to perform calculations on the duct shield and took me to the international workshop GWADW in Italy, which allowed me to give my presentation about the research on the duct shield[31].

I conducted the measurement of thermal radiation through the pipe in Cryogenics Science Center, KEK, where Dr. Tomaru and many people helped me to set up the experiment and let me use the experimental apparatus.

In the student room, Dr. Shiomi, Dr. Hirose, Dr. Konishi, Dr. Saito and Mr. Sekiguchi gave me not only useful advice about my research but also interesting or amusing information.

Here, I express my thanks to all people who helped me, including the people mentioned above.

References

[1] J M. Weisberg and J H. Taylor: "Relativistic binary pulsar B1913+16: thirty years of observations and analysis," ASP Conference Series **328** (2005) 25-31

[2] K. Kuroda: "Status of LCGT," Class. Quantum Grav. **27** (2010) 084004

[3] D. Sigg: "Status of the LIGO detectors," Class. Quantum Grav. **23** (2006) S51

[4] F. Acernese, et al.: "Status of Virgo," Class. Quantum Grav. **25** (2008) 114045

[5] H. Grote: "The status of GEO 600," Class. Quantum Grav. **25** (2008) 114043

[6] M. Punturo et al.: "The Einstein Telescope: a third-generation gravitational wave observatory," Class. Quantum Grav. **27** (2010) 194002

[7] M.Maggiore: "Gravitational Waves I. theory and experiments," Oxford Univ. Press (2007)

[8] T. Nakamura et al.: "Juryokuha wo Toraeru," Kyoto University Press (1998) [in Japanese]
中村卓史、三尾典克、大橋正健：「重力波をとらえる」、京都大学学術出版会、京都 (1998)

[9] P R. Saulson.: "Fundamentals of interferometric gravitational wave detectors," Singapore ; River Edge, NJ : World Scientific (1994)

[10] "LCGT design document Version 3.0" (2009) [in Japanese]

[11] S. Miyoki, et al.: "The CLIO project," Class. Quantum Grav. **23** (2006) S231

[12] M. Shoji: "Heat transfer textbook," Tokyo Univ. Press (1995) [in Japanese]
庄司正弘：「伝熱工学（東京大学機械工学 6）」、東京大学出版会、東京 (1995)

[13] J. P. Holman: "Heat transfer 10th ed," Boston : McGraw-Hill Higher Education (2010)

[14] Y. Sakakibara et al.: "Reflectivity Measurements of Metals for LCGT Thermal Radiation Shields at Cryogenic Temperature and Wavelength of 10 μm," TEION KOGAKU **46** (2011) 434-440 [in Japanese]
榊原裕介ら：「大型低温重力波望遠鏡（LCGT）熱シールド用金属の低温における波長 10 μ m での反射率測定」、低温工学、**46** (2011) 434-440

[15] R F. Barron: "Cryogenic heat transfer," Philadelphia: Taylor & Francis (1999)

[16] K G. Ramanathan, S H. Yen, E A. Estalote.: "Total hemispherical emissivities of copper, aluminium, and silver," Appl Opt **16** (1977) 2810-77

[17] D. Giulietti, M. Lucchesi.: "Emissivity and absorptivity measurements on some high-purity metals at low temperatures," J Phys D Appl Phys **14** (1981) 877-881

[18] S. Tsujimoto, M. Kanda, T. Kunitomo.: "Thermal radiative properties of some cryogenic materials," Cryogenics **22**(11) (1982) 591-7

[19] V. Musilova et al.: "Low temperature radiative properties of materials used in cryogenics," Cryogenics **45** (2005) 529-536

[20] V. Musilova et al.: "Effect of different treatments of copper surface on its total hemispherical absorptivity bellow 77 K," Cryogenics **47**(4) (2007) 257-261

[21] Electrical resistivity of copper(99.999 %). AIST Network Database System for Thermophysical Property Data

[22] M.Born et al.: "Principles of optics : electromagnetic theory of propagation, interference and diffraction of light, 7th ed," Cambridge University Press (1999)

[23] D R. Lide: "CRC Handbook of Chemistry and Physics, 90th ed," CRC Press, Boca Raton (2008) 12-121, 12-124

[24] National Astronomic Observatory of Japan. Rikanenpyo, Maruzen publishing (2009) [in Japanese]
国立天文台：「理科年表」、丸善 (2009)

[25] Y. Saito, et al.: "Vacuum system of the 300 m gravitational wave laser interferometer in Japan (TAMA300)," Vacuum **53** (1999) 353-356

[26] M. S. Hunter and P. Fowle: "Natural and Thermally Formed Oxide Films on Aluminum," J. Electrochem. Soc. **103** (1956) 482-485

[27] J. A. Allen: "Oxide films on electrolytically polished copper surfaces," Trans. Faraday Soc. **48** (1952) 273-279

[28] T. Tomaru, et al.: "Conduction effect of thermal radiation in a metal shield pipe in a cryostat for a cryogenic interferometric gravitational wave detector," Jpn. J. Appl. Phys. **47** (2008) 1771-1774

[29] Y. Kuraoka, et al.: "Heat analysis and reduction of evaporation rate of liquid helium dewar," Cryogenics **19**(4) (1979) 182-186

[30] T. Tomaru, et al.: "Study of Heat Load Reduction for the LCGT Cryostat," J. Phys. Conf. Ser. **122** (2008) 012009

[31] N. Kimura, Y. Sakakibara et al.: "Present Design of LCGT Cryogenic Payload - Status of Cryogenic Design -," GWADW, Id:15, La Biodola, Isola d 'Elba, Italy (2011)